Automotive Radar Imaging Using Noncoherent Sensors

Florian B. Ramian, geb.Helmbrecht

Fachgebiet Höchstfrequenztechnik, Technische Universität München

Automotive Radar Imaging Using Noncoherent Sensors

Fachgebiet Höchstfrequenztechnik, Technische Universität München

Automotive Radar Imaging Using Noncoherent Sensors

Florian B. Ramian, geb.Helmbrecht

Vollständiger Abdruck der von der Fakultät für Elektrotechnik und Informationstechnik der Technischen Universität München zur Erlangung des Akademischen Grades eines

Doktor - Ingenieurs

genehmigten Dissertation.
Vorsitzender:

Univ.-Prof. Dr. sc. techn. (ETH) Andreas Herkersdorf

Prüfer der Dissertation:

1. Univ.-Prof. Dr.-Ing., Dr.-Ing. habil. Erwin Biebl

2. Univ.-Prof. Dr.-Ing., Dr.-Ing. habil. Stefan Lindenmeier,
Universität der Bundeswehr München

Die Dissertation wurde am 15.09.2005 bei der Technischen Universität München eingereicht und durch die Fakultät für Elektrotechnik und Informationstechnik am 05.05.2006 angenommen.

ABSTRACT

This work treats the development and evaluation of a new concept for an imaging radar algorithm for the automotive environment. The system under investigation, is especially examined for its applicability in a multi-target scenario, i.e. more targets than sensors, a basic requirement of the industry. The assignment problem resulting from trilateration of a multi-target scenario is investigated and solved. Furthermore, sensors without any synchronization of frequency or phase are used to keep the system cost efficient.

Diese Arbeit behandelt die Entwicklung und Evaluierung eines neuen Konzeptes für ein bildgebendes Radarverfahren für den automobilen Einsatz. Das untersuchte Verfahren ist in der Lage, eine Mehrziel-Szenario, gemeint ist hier mehr Ziele als Sensoren, so abzubilden, dass es den grundlegenden Anforderungen der Automobilbranche entspricht. Hierbei wird nicht nur das Zuordnungsproblem, welches bei der Anwendung des Trilaterationsverfahrens auf eine Mehrzielumgebung auftritt, berücksichtigt, sondern auch bewusst auf die Synchronisierung der einzelnen Radarsensoren, bzgl. Frequenz oder Phase, verzichtet, um die Kosteneffizienz des Gesamtsystems zu steigern.

Danksagung

Die vorliegende Arbeit stellt das Ergebnis meiner Tätigkeit am Fachgebiet Höchstfrequenztechnik der Technischen Universität München dar.

Mein besonderer Dank gilt daher Prof. Dr. E. Biebl, der mir durch seine fachliche Kompetenz und seine Motivationskraft diese Arbeit ermöglicht hat. Auch für die Ermöglichung von Konferenzreisen und sein stets offenes Ohr für viele meiner Anliegen möchte ich mich bedanken.

Ich möchte mich ferner bei meinen Kollegen, insbesondere bei den Diplom-Ingenieuren Florian Gerbl und Magnus Olbrich, sowie bei Dr.-Ing. M. Beer, Dr. rer. nat. M. Streifinger und Dipl.-Ing. C. Morhart für deren fachliche Unterstützung und das angenehme Arbeitklima bedanken.

Besonders herzlich möchte ich mich bei allen bedanken, die mir im privaten Umfeld Rückhalt gegeben haben, im Besonderen meiner Frau Tanja.

CONTENTS

1. INTRODUCTION

In the world of today, mobility is a key characteristic in any society. Not only does it offer a greater flexibility to the employee, but it increases dramatically the sales market for almost any product. The downside of this trend toward more mobility is the higher density of traffic in general. Studies demonstrate that at a certain traffic density, the slightest braking of a car may cause fatal congestions. This results from the disability of most drivers to correctly determine the deceleration rate and the distance to the vehicle ahead. To navigate a car safely in heavy traffic, it is not enough to just measure the exact distance to the vehicle in front, but the entire scenario has to be taken into account. As this is not possible with current cruise control systems, the so called autonomous drive of today is limited in a number of ways. On the one hand, the systems allow only inefficient large distances in between cars and are on the other hand limited to moderate acceleration and deceleration values. Furthermore, current systems cannot operate a car in "Stop and Go" mode, due to a lack of precision, especially of angular precision. Though automated "Stop and Go" is very comfortable for the driver, the main goal is still the avoidance of dangerous situations, setting a person's life at risk. Such a situation might arise for example if a child suddenly appears on the road from behind a parked car. Clearly, an emergency break is required here. The same maneuver cannot be tolerated if a tin can appears on the road. Therefore a system that is allowed to initiate heavy deceleration needs to exhibit high reliability. Definitely, high precision images as well as object identification are necessary to obtain this..

To establish a new product on the automotive supplier market, observing standards on reliability, cost, and size is crucial. As with any new product, a certain degree of innovation and usefulness is required. Within the automotive market, new features need to be eyecatchers. Eyecatcher does not necessarily mean something visible, as an extraordinary design, but relates more to the appearance in the press and commercials. For example, a functionality that protects pedestrians, even if it only flattens an edge that the predecessor model did not even exhibit, will result in numerous positive press appearances of the corresponding car and mark the respective brand as innovative.

Customers on the automotive market can be separated into two groups. Functionality and design oriented buyers. Speaking very figurative, the first group is not willing to pay a cent for anything that goes beyond the basic functionality of driving. The second group on the other hand, is able and willing to pay more money for a car, but the money goes straight into the brands and the design. Therefore, a low price per unit is essential. This can only be reached, if large quantities are sold.

At the same moment, where low cost per unit is required, a high reliability is required.

This results on the one hand from the high quantities argument above, meaning that an error requires the replacement of many devices. On the other hand, most parts in a car can cause enormous damage if they malfunction. A good example is an erroneous brake.

Connected to the pricing argument is another main argument, car manufacturers have to deal with. People do not buy cars to travel, but because of their design. This exaggerated statement is not as exaggerated as it might appear, but it is crucial for additional features, such as a radar system. It must not influence the appearance of the vehicle, i.e. it has to vanish somewhere inside the chassis.

It is furthermore important for almost all systems in cars to work as real time applications. Depending on the specific application, the maximum processing time that has to be guaranteed varies. For a pre-crash sensor for example, the processing time available is shorter than for imaging systems, as the covered targets are closer.

These demands of the automotive industry that are also cited in a number of publications [1–3] apply for radar imaging systems as they do for any other system. The aim of this work is now to consider, whether an imaging radar system can be developed that obeys all these demands and at the same time provides a reasonable radar image. Designing an imaging system itself is far from trivial, but as it comes to the above mentioned restrictions, entirely new concepts need to be investigated.

1.1 State of the Art

Imaging radars are not only investigated with a focus on the automotive industry, but do play a major role in research on nondestructive-testing [4] and meteorology [5]. Therefore, all of the above mentioned paragraphs solutions exist. Unfortunately none of them satisfies more than two prerequisites. The most common solutions will be described shortly with their advantages and disadvantages.

Precise radar images can be obtained using scanning radars, as e.g. in nautical navigation. Almost any naval vessel is equipped with the characteristically rotating antenna. Many stationary radars use this method, which provides good angular precision in combination with any radar method chosen to perform the range measurement. The disadvantages of this system are clearly the moving parts, as well as the influence on the shape, i.e. design of the car. Another realization of a scanning radar is the phased array radar. It works basically the same way as the mechanically scanned radar, but has no moving parts. This results from electronically panning the antenna radiation pattern. It is reached by building a single antenna from a large number of antenna elements. Each element has to be fed and the phase of the feeding line needs to be adjustable. This is equivalent to high production cost, as active elements to control the phase of radar frequencies are extremely expensive.

Recent upper class cars come with adaptive cruise control. This means that the cruise control does not control the velocity but the distance to the car ahead. The distance is measured by radar sensors. These sensors do provide only poor angular precision and are therefore not suited for imaging. The modules commercially available furthermore do have data processing units included, i.e. raw data is not available. This makes them slow. As

pricing is a main argument in the automotive supplier market, sensors that can handle pre-crash detection as well as high precision imaging are desired.

In contrast to the above, there are also publications and pending patents [6, 7] dealing especially with near range radar systems that depend on phase information for angular resolution. This technique is different to the above mentioned phased array method, as not the antenna pattern is steered, but the phase difference is used to determine the target angle using the known location of each sensor and the propagation delay given by the phase difference. The system therefore provides a high relative range resolution, i.e. propagation delay between two sensors. As mentioned, a high angular resolution is reached by accepting higher production cost.

Radar imaging is also performed by combining information from multiple sensors. A very old method to combine information is triangulation or trilateration. To locate an object in a three dimensional space, three distance or three angle measurements are necessary. If each measurement was performed from a different reference point, with known location and infinite precision, the result is an exact location. This method works perfectly for a single unknown location, but gets out of control, if multiple indistinguishable objects are to be located.

So called superresolution algorithms usually deal with the same problem. Publications [8, 9] on those algorithm often state the condition of more sensors than objects. This is unrealistic for a roadside scenario. Furthermore, a number of publications deals with the combination of different sensors, i.e. using different frequencies, different ranging methods, such as pulse and spread spectrum, or even combining radar with infrared sensors [10–15]. These publications use radar sensors that were selected because of their precision, but not because of their cheap assembling cost.

In addition, there are also methods that try to assign targets to classes, which can be characterized by specific values such as speed [16]. Many of the above mentioned methods can also be transferred into the optical domain, as described in [17].

1.2 Goal of this Work

A recent project at the Fachgebiet Höchstfrequenztechnik [18] brought up a cheap and powerful radar front end. It was developed for usage in the automotive environment and fulfills therefore the above mentioned boundary conditions concerning cost and size. As raw data is available at reasonable speed, the front end is basically suitable for both, pre-crash detection as well as radar imaging.

This work is supposed to determine, whether it is possible to combine two or more of these radar front ends into a cost effective imaging system. Due to the required cost effectiveness, it is not possible to evaluate the phase of received signals, which allows more precise range measurement. As the imaging system is not intended to be connected to one specific radar front end, the general question arose, whether radar imaging using noncoherent sensors reaches reasonable precision in a roadside environment. Other sensors that could be used, include not only pseudo noise or spread spectrum sensors as in [19], but

also pulse or other radars or even optical sensors. As already mentioned, common concepts for radar imaging do not qualify for the automotive market, due to the limitations explained above. Therefore, a new concept needs to be developed and evaluated for its applicability. The basis of the new concept was the suggestion to use noncoherent sensors, as well as the offer to utilize a recently developed pseudo noise radar sensor. Using noncoherent sensors is also a main difference compared to systems, such as in [7].

2. PROPOSED RADAR-SYSTEM CONCEPT

The following chapters will first give an overview on radar systems in general, before describing the elements of the front-end of one sensor of the proposed radar system.

2.1 Radar Considerations

Radar, or RAdio Detection And Ranging, at first detects only the range of a target, as denoted by its long form. In opposite to its original meaning, radar is equivalent to radar imaging for many people. In this chapter, the focus is set on a single radar sensor that outputs distance and amplitude information. For the design of a radar system, one of the first decisions to be made deals with the type of radar to be used. The choice is basically to be made among pulse radars and continuous wave radars. The decision for or against a certain type will be based on factors like cost efficiency, complexity of the system, and target detection capabilities, i.e. can moving and stationary targets be detected. Furthermore the achievable dynamic range, minimum and maximum detection distance, and the compliance to bandwidth and power limitations, given by regulating authorities, dominate the decision. Additionally, radar systems are distinguished as mono- and bi- or multistatic systems, depending on whether transmitter and receiver are collocated or not. All the following systems can be designed as either mono- or bistatic systems.

2.1.1 Pulse Radar

Classical Pulse Radar

The oldest and most commonly known system is the pulse radar. A short pulse is sent and the reflection from the target is received. The range is determined by examining the round-trip delay of the pulse. A block diagram for a pulse radar is shown in Fig. 2.1. A critical element in Fig. 2.1 is the transmit/receive switch or whatever element is used to create the pulse. The pulse length limits on the one hand the resolution of the radar and sets the bandwidth requirements on the other hand. The shorter the transmit pulse duration, the higher the range precision, as the delay time measurement is more precise. This means for a multi target environment, i.e. a sum of reflected pulses, each with a different delay, the minimum distance between two targets necessary to detect both of them decreases with decreasing pulse width. Sec. 2.2.2 goes more into detail on the resolution aspect. Furthermore, the detection of a target depends on the energy of the received pulse due to low pass characteristics of all elements. This means the shorter the pulse, the higher the

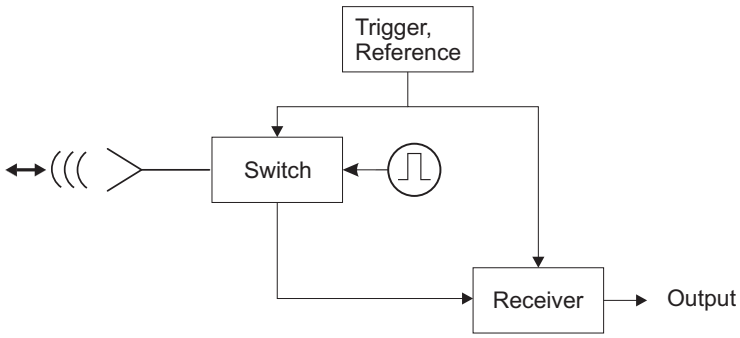

Fig. 2.1: Block diagram of a pulse radar

required peak power to detect a given minimum target. Peak power levels are critical in pulse radar systems. Usually, maximum peak- as well as average power levels are specified for frequency bands. Pulse radar peak powers therefore will be limited by either peak power specification of the band or technical limitations of the peak power. In general, the maximum allowed transmitted energy is higher, when continuous transmission is used, obeying the maximum average power, instead of pulses limited by the maximum peak power. Besides the power limitations, bandwidth limitations apply to all radar applications. This means the pulse duration is roughly inversely proportional to the occupied bandwidth. As far as bandwidth is concerned, the general goal is to keep it narrow. The reason is cost. The more bandwidth a system requires, the higher the licensing cost for the respective band. Furthermore, system elements become more expensive, when designed for broader bandwidth. A monostatic pulse radar using a switch as in Fig. 2.1 has also a minimum detection range. It results from the so called "blind time", i.e. the time during which the switch connects the antenna to the transmitter to send out a pulse, instead of the receiver. As indicated by its name, the receiver is "blind" during this time. The other degree of freedom goes into the pulse repetition frequency (PRF). It is the reciprocal time between two pulses. The maximum detectable range as well as the probability for ambiguities are determined by the PRF. The maximum detectable range is given by $\frac{c_0}{2\mathrm{PRF}}$, i.e. the reflected pulse must be received before the following pulse is sent. Ambiguities in range detection arise for high PRFs, i.e. short time between two pulses. A distant but strong target might be detected as a close target, because the returning pulse is not detected before the next pulse is sent. This is illustrated in Fig. 2.2.

Pulse Compression Radar

The bandwidth problem of the classical pulse radar led to the development of the so called pulse compression radar. The idea behind pulse compression is to spread a sharp, narrow, and high power pulse before transmitting it. This is done by means of a filter $H(\omega)$. The filter changes the phase of the different spectral components of the pulse in a determined way, which results in broadening of the pulse itself. On the receiver-side this effect is reverted by applying a matched filter $H^*(\omega)$ to the RX signal. The result is a

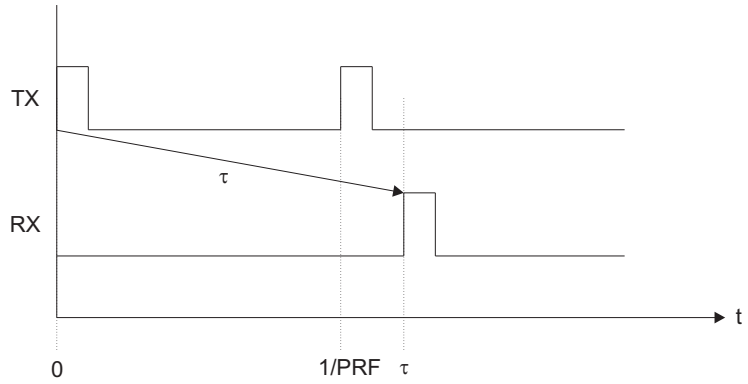

Fig. 2.2: Ambiguities in pulse radar systems, due to high PRF

pulse comparable in width to the original pulse. The actual pulse width and shape can be determined by evaluating $\mathcal{F}^{-1}\{H(\omega) \cdot H^*(\omega)\}$. The principle is sketched in Fig. 2.3. The matched filter principle in the schematic is equivalent to either a correlator or a combination of time inversion and a filter $H(\omega)$. The correlator principle, i.e. correlating the received signal delayed by a fixed time τ resulting from the target distance, with the original transmit signal is used for the PN-radar as well. This is shown in Sec. 2.2. The advantages delivered by pulse compression are various. Due to the spread pulse, the average power can be increased without simultaneously increasing the peak power or decreasing the unambiguous range by using a higher PRF. The matched filter principle can be seen as a coding algorithm. Coding brings along the advantage of reduced sensibility to interfering signals. Pulse compression is therefore closely related to the PN-radar principle.

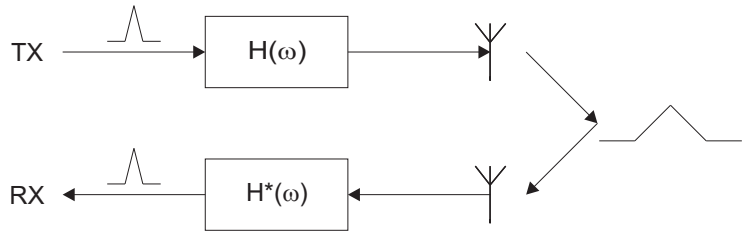

Fig. 2.3: Block diagram of a pulse compression radar sensor

2.1.2 Continuous Wave Radar

In opposite to pulse radars, CW radars transmit continuously, which avoids extreme peak power values, but still provides high energy for a detection interval Δt. Basically the CW radar systems can be distinguished on whether the carrier is modulated or not.

Unmodulated CW Radar

Unmodulated CW radars are also referred to as moving target indication (MTI) radars. The functionality is based on the Doppler effect. A continuous wave RF signal is transmitted. An approaching or departing target, i.e. an object that has a radial velocity component with respect to the radar, reflects the wave back and thereby changes the frequency of the carrier depending on its radial velocity. The receiver detects the frequency difference between the transmitted and received signal and calculates the velocity of the object from the Doppler formula Eq. 2.65. The disadvantage of this method is that stationary targets, or targets that move on a constant radius circle around the radar, cannot be detected.

Modulated CW Radar

Modulated CW radars on the other hand transmit continuously as well but use a modulated carrier. There is a variety of modulations that are used. A linear frequency modulation over time is described here as it is very figurative. These radar systems, unlike the unmodulated ones, are able to detect moving targets as well as stationary ones. In the easiest case, the frequency of the transmitted signal varies linearly with time between $f_{\min}$ and $f_{\max}$ during a time interval Δt. After reaching $f_{\max}$, the frequency goes back to $f_{\min}$ either spontaneously or linearly, which results in sawtooth- and triangular-shaped frequency-over-time graphs as in Figs. 2.4 and 2.5, respectively. As shown in Figs. 2.4 and 2.5, the frequency difference

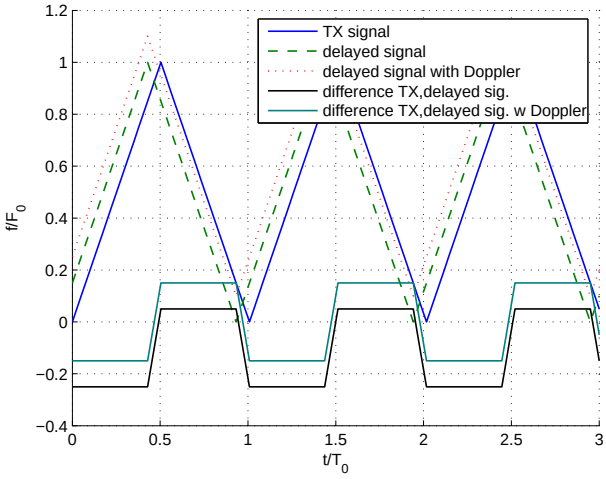

Fig. 2.4: Triangular modulating signal and possible receive signals

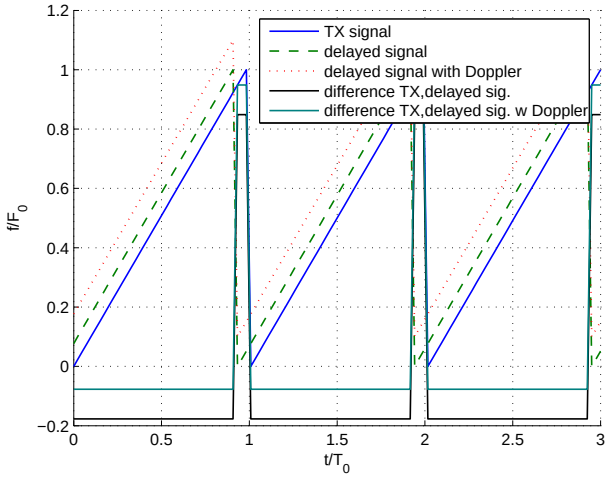

Fig. 2.5: Sawtooth shaped modulating signal and possible receive signals

between transmitted and received signal, obtained by a mixer, results from two effects. The first effect causing the frequency difference, is the modulation. The target reflected, received signal is delayed, compared to the transmitted signal. The frequency difference results from

$$f_{\mathrm{IF}} = \frac{(f_{\mathrm{cmax}} - f_{\mathrm{cmin}})}{\Delta t} \cdot \tau \tag{2.1}$$

with $\tau = \frac{2r}{c_0}$ the delay time resulting from the distance of the reflector to the target r, and f_{IF} the frequency difference obtained by mixing the TX and RX signal. The other effect causing frequency variation of the received signal is again the Doppler effect as already mentioned. To separate the Doppler and the delay effects and therefore to detect distance as well as radial velocity, triangular shapes of the frequency-over-time graph are preferred over sawtooth-shaped ones. For triangular shapes f_{IF} is a sum signal for the rising slope and a difference signal for the falling slope. Obviously, the two terms can be separated easily by combining sum and difference signal. For sawtooth shaped signals it is not possible to clearly separate both components. In general $\Delta f = f_{\max} - f_{\min}$ is chosen so that $\tau \frac{\Delta f}{\Delta t} > f_{\mathrm{D}}$ to avoid the need for case distinction. Under this constraint the distance can be written as

$$r = \frac{\Delta t\, c_0}{4\,\Delta f}\, \tau \cdot (f_{\mathrm{IF,rise}} - f_{\mathrm{IF,fall}}) \tag{2.2}$$

and the Doppler shift is obtained as

$$f_{\mathrm{D}} = \frac{1}{2} \cdot (f_{\mathrm{IF,rise}} + f_{\mathrm{IF,fall}})\,. \tag{2.3}$$

The advantages are therefore lower peak power levels and combined detection of velocity and range by a single circuit. The cost of this method is a more complex circuitry, especially for the TX side, where a modulator must be integrated.

2.1.3 Passive and Semi-Active Target Location

Research on passive and semi-active target location is especially enforced by the defense industry. A primary problem with radar for defense applications is the radiated power. Any transmit antenna, especially high power ones, can be detected and therefore destroyed easily. Different countermeasures were applied to reduce vulnerability of defense radars. Positioning the redundant transmit antennas at different locations than the receive antenna can avoid destruction of the entire system, but difficulties arise, as the receiver needs information from the transmitter, i.e. RF- or at least IF-connections between TX- and RX- device are required. Hiding the transmit signal beneath the noise is possible by spreading the signal as in PN-radars, but brings along the disadvantage of low maximum ranges, as the TX power is low. So the need for passive and therefore undetectable radars brought along the passive and semi-active radar. A semi-active radar, is a system that does not have its own transmitter. It can be realized by using signals originating from e.g. radio and television transmitters. The idea is basically to listen for echoes of these signals that might result from a reflection from e.g. a hostile aircraft and calculate the target location. This triangulation step uses the information provided by the difference in time of flight between the directly received signal and the signal reflected from the target. By using multiple receive antennas and detecting the Doppler shift, additional information for a radar image can be obtained. Information on realized passive radar systems are scarce, but the idea for a passive radar was mentioned first in the 1950s. A main field of passive radar is radiometry, e.g. in [20]. Radiometry treats the detection of signals,

in relation to radar especially microwave signals, of thermal origin. This means that the radar does not rely on any echoes from the target but on emissions from the target itself. Radiometry deals with thermal emissions, i.e. mainly from the engine, but other emissions, such as communication signals or other RF transmitters on board the hostile target can be valuable for the passive radar system. The predominant problem for these systems is the power level that is several orders of magnitude smaller than that active radars deal with. The advantages that drive research is on the one hand the "invisibility" of the radar and on the other hand system immanent factors, such as r^{-2} dependence instead of r^{-4} and reduced power consumption and therefore weight.

2.1.4 Radar Frequencies

For military applications several frequency bands are reserved. As some devices are kept secret, it is hard to get information on frequency bands used. In general, military applications do not have to fulfill such stringent power and bandwidth limitations as commercial applications. Besides frequency bands assigned to military radar applications, there are some more bands that are exclusively reserved for radars. One would be the civil aviation control radar. For automotive radars, such as described in this document, only the so called ISM bands are of interest. ISM stands for Industrial Scientific and Medical. Devices are free to operate within the boundaries of this bands, provided that they fulfill all regulations applying to the respective band, above all power limitations. For the automotive industry, especially the ISM band at 24.00-24.25 GHz is of interest. This frequency already provides good propagation conditions under all weather situations, e.g. low attenuation for foggy or wet environments. On the other hand, the bandwidth available here is larger than for lower ISM bands. As 250 MHz is still far from the requirements of Ultra-Wide-Band (UWB) radars, some current automotive radars are designed to use the recently assigned automotive radar band at 76-77 GHz by the European Radiocommunications Committee (ERC). With a bandwidth of 1 GHz it allows a resolution about four times better than within the ISM band. The correlation of available bandwidth with maximum resolution of the system is valid for all radar system, no matter whether FMCW, pulse or PN techniques are used. In the USA, the Federal Communications Commission (FCC) approved the allocation of an unlicensed spectrum from 3.1-10.6 GHz for communication and imaging systems. [21] further mentions the approval of another 7 GHz band at 22-29 GHz by the FCC. Although the need for UWB radar bands is acknowledged by the ERC, frequency allocations in excess of the 76 GHz band have not been assigned yet.

2.1.5 Mono-, Bi-, and Multistatic Radars

This section will in short mention the differences between these concepts. They are in general the co- or dislocation of transmit and receive antenna.

Monostatic Radars Monostatic radars are radars that have only a single antenna. It is connected to the transmit and receive circuit through a switch, i.e. the radar either receives

or transmits, but never both at same time. Therefore this concept is not ideal for every type of radar. An FMCW radar cannot be realized reasonably as a monostatic one. A pulse radar on the other hand is ideal for a monostatic concept. Although a so called blind time exists, during the transmit time, see Figs. 2.1 and 2.2, it is usually negligible, due to very short pulses. In addition a separate transmit antenna would be idle most of the time, again due to short pulses, compared to 1/PRF. For systems requiring compact dimensions, a monostatic system might be the layout of choice.

Bi- and Multistatic Radars A bistatic system consists of one transmitter spatially separated from the receiver. As mentioned above, some systems require the possibility to transmit and receive at the same time. If there is more than one transmitter or receiver, many documents speak of multistatic systems, though the term bistatic is used for these configurations too. Besides higher cost for multiple antennas, bistatic systems offer advantages. In military use, separating transmitter and receiver protects the receiver. The transmitter can be located easily by the host, as it is transmitting a significant amount of microwave power. The receiver on the other hand is hardly identified. So it makes sense to collocate expensive parts of the system with the receiver and to implement the transmitter structures redundant.

2.2 PN-Radar Principles

The radar system under investigation for this work uses pseudo-noise (PN) sensors. The characteristic feature of this type of radar is the spreading code used to modulate the carrier. Spreading technology is a specific realization of the pulse compression technique, as already mentioned. Cheap microprocessors allow the generation of long spreading sequences that let appear the signal random and therefore noise-like.

2.2.1 PN sequences

As already mentioned in Sec. 2.1.1, spreading technology can be described as a matched filter receiver or equivalent as a correlation receiver. For PN radars, the time domain function of the transmit filter is a random looking series of “0” and “1” generated by a linear tapped delay line, also referred to as linear feedback shift register (LFSR), as shown in Fig. 2.6. Using a LFSR means the code can be generated by using l unit-delay elements and l or less exclusive-or (EXOR) gates. This is visualized in Fig. 2.6 by using parameters $a_0 \dots a_l \in \{0,1\}$, with “1” indicating the existence of a tap. From l the number of unit-delay elements, i.e. a delay of a bit-length T_c, the length of the code in bits L can be written as

$$L = 2^l - 1. \tag{2.4}$$

Maximum length sequences or m-sequences can be easily generated by using a single linear feedback shift register. Combining two or more m-sequences from different shift registers by means of EXOR gates results in code families such as Gold- and Kasami-sequences.

More information and mathematical deduction of their properties is available in [22, 23]. The name pseudo-noise relates to the spectrum of this sequences. The spectrum looks like white noise for the ideal case. The ideal case is marked by zero-length bits, i.e. $T_c \rightarrow 0$, and an infinitely long sequence, which equals white noise. The real world case has a relatively constant amplitude in the spectrum roughly between f_{min} and f_{max}, with $f_{min} = \frac{1}{L \cdot T_c}$, $f_{max} = \frac{1}{T_c}$, L the code length, and T_c the bit duration. Depending on whether a uni- or bipolar sequence, i.e. a 0/1 or a -1/1, was chosen, the spectrum contains either a dominant or a negligible DC component. The exact spectrum depends of course on the pulse form of a single bit. A single bit of the sequence is also referred to as a chip. The spectra of a real PN sequence with Gaussian shaped pulses and white noise are compared in Fig. 2.7. It is clearly visible that a bipolar sequence was plotted, as the DC component is negligible. Furthermore, the spectrum can be separated into a Gaussian shape and the periodic continuation of the auto-correlation function (ACF) of a maximum length sequence (m-sequence). This fact is deduced in Sec. 2.2.2. A large variety of PN sequence families

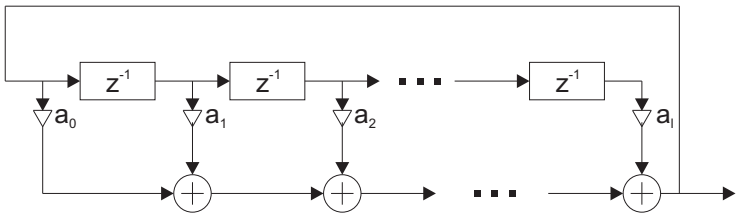

Fig. 2.6: Block diagram of tapped delay line PN sequence generator

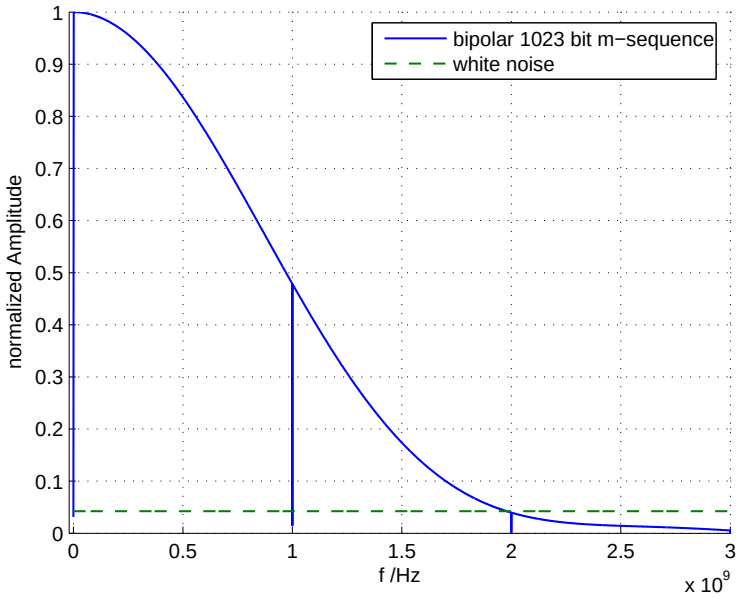

Fig. 2.7: Spectra of a 1023 bit m-sequence and white noise

exist. A short summary of periodic correlation sequences will be given here according to

[22]. To be able to compare the sequences with respect to their applicability for automotive radar systems, relevant correlation functions are defined first.

Auto-Correlation-Function

In general, for a function

$$f(t) \begin{cases} \neq 0 & \text{for} \quad |t| \leq \frac{T}{2} \\ = 0 & \text{for} \quad |t| > \frac{T}{2} \end{cases}$$

the auto-correlation is defined as

$$\varphi_{ff}(\tau) = \int_{-T/2}^{T/2} f(t) \cdot f(t+\tau)\,\mathrm{d}t. \tag{2.5}$$

A circuit schematic to obtain a correlation function (CF) of a received and a reference signal is depicted in Fig. 2.8. In the following, ACF will refer to periodic ACFs, i.e. the function f

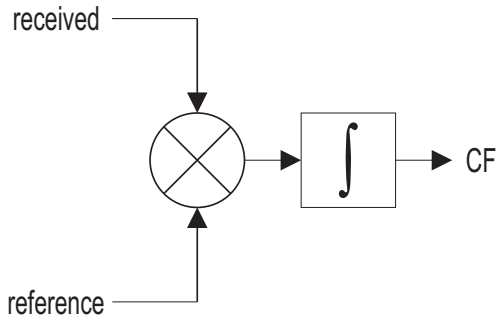

Fig. 2.8: Block circuit of a correlator

is periodically continued and therefore φ_{ff} is periodical, too. The ACF is characterized by a peak at location $\tau = 0$. As for radar systems, the dynamic range is the limiting factor for detection, it is important to obtain a high main-to-side-lobe ratio, i.e. ideally the following condition is fulfilled

$$\mathrm{ACF} \begin{cases} = 0 & \text{for} \quad \tau \neq 0 \\ \to \infty & \text{for} \quad \tau = 0 \end{cases}. \tag{2.6}$$

Though for an infinite main-to-side-lobe ratio, only one of the conditions in Eq. 2.6 needs to be fulfilled, it is desirable, to look for ACFs that come close to both conditions, as zero as well as infinite values do not exist in real world systems. Although most mathematical publications would not use the term auto-correlation function for the correlation within a PN-radar receiver, due to the delayed received signal, the term will be used in this document.

$$\varphi_{s_{\mathrm{rec}}s_{\mathrm{ref}}}(\tau) = \int_{0}^{LT_{\mathrm{c}}} s_{\mathrm{rec}}(t - z_n T_{\mathrm{c}}) \cdot s_{\mathrm{ref}}(t+\tau)\,\mathrm{d}t \tag{2.7}$$

with $z_n \in \mathbb{R}$, the delay-time that corresponds to the distance transmitter – target n – receiver,

$$z_n = \frac{2 \cdot r_n}{c_0 T_\mathrm{c}} \tag{2.8}$$

normalized to T_c. For now $n = 1$, i.e. there is only one target. The signals

$$s_\mathrm{ref} = m_\mathrm{u}(t) = \sum_{k=1}^{L} c_k \delta(t - kT_\mathrm{c}) \tag{2.9}$$

and

$$s_\mathrm{rec} = m_\mathrm{b}(t - z_1 T_\mathrm{c}) = \sum_{k=1}^{L} d_k \delta(t - kT_\mathrm{c} - z_1 T_\mathrm{c}) \tag{2.10}$$

are assumed to be periodic with LT_c, i.e. continuous operation, with $c_k \in \{0,1\}$ and $d_k \in \{-1,1\}$. With known spectra $S_\mathrm{rec} = \mathcal{F}\{s_\mathrm{rec}\}$ and $S_\mathrm{ref} = \mathcal{F}\{s_\mathrm{ref}\}$ the ACF can alternatively be written as

$$\varphi_{s_\mathrm{rec} s_\mathrm{ref}}(\tau) = \mathcal{F}^{-1}\big\{S_\mathrm{rec}(-f) \cdot S_\mathrm{ref}(f)\big\}. \tag{2.11}$$

Eq. 2.11 can be derived from Eq. 2.18. It is necessary to mention that the above equations refer to the mathematical definition of a correlation function. In real world systems, it is not possible to implement a negative delay so the expression

$$\varphi_{s_\mathrm{rec} s_\mathrm{ref}}(-\tau) = s_\mathrm{rec}(t) * s_\mathrm{ref}(-t) = \mathcal{F}^{-1}\big\{S_\mathrm{rec}(f) \cdot S_\mathrm{ref}(-f)\big\} \tag{2.12}$$

is usually referred to as correlation function.

The decision to transmit the bipolar sequence is arbitrary for now. Mathematically correct, Eq. 2.7 does not describe an ACF, as the functions f and g are correlated, with $g(t) = f(t - t_1)$, i.e. a delayed copy of f. This means $\varphi_{s_\mathrm{rec} s_\mathrm{ref}}$ is a shifted ACF with the peak at $\tau = -z_n T_\mathrm{c}$. In real world systems, the received signal s_rec is furthermore superimposed by noise and DC offset. The peak of the ACF is characterized by its width and its height. In real world correlations, the width of the ACF peak depends on the chosen pulse form and limits the resolution as calculated in Sec. 2.2.2. The peak is limited to a height of LT_c, which results from Eq. 2.5 and the fact that m-sequences contain N_H high-bits and N_L low-bits with

$$N_\mathrm{H} = 2^{l-1} \tag{2.13}$$

and

$$N_\mathrm{L} = 2^{l-1} - 1, \tag{2.14}$$

i.e. $L = N_\mathrm{H} + N_\mathrm{L}$. For a properly selected code family, it is possible to obtain zeros for all side lobes, which results in an infinite main-to-side-lobe ratio. A promising combination is the concurrent use of a bipolar and a unipolar m-sequence, i.e. the reference contains a unipolar m-sequence and the transmit signal uses the same sequence but coded bipolarly or vice versa. In Fig. 2.9 the ACF of a $L = 15$ bit m-sequence is shown for the three relevant cases, unipolar with unipolar, bipolar with bipolar, and the combination of a unipolar and a bipolar one.

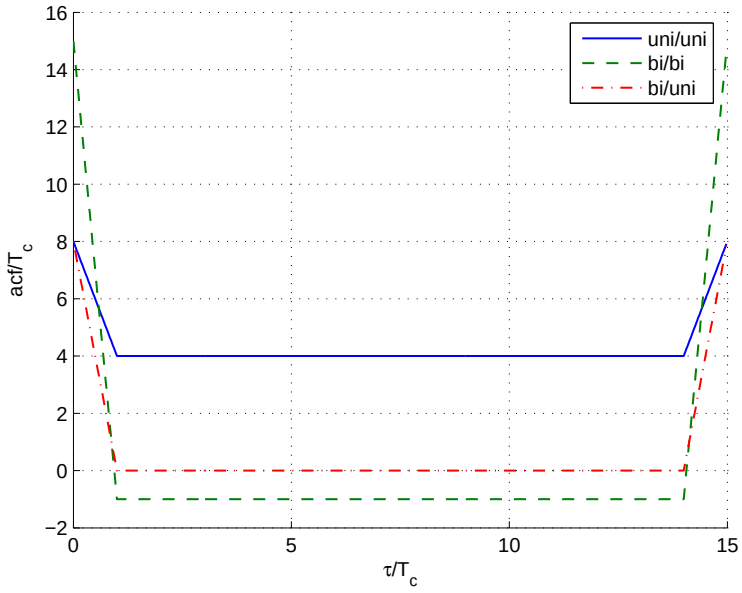

Fig. 2.9: Comparison of ACFs of a $L = 15$ bit m-sequence, uni- and bipolarly coded

Cross-Correlation

A cross-correlation function (CCF) in general is the correlation of two different functions

$$\varphi_{fg}(\tau) = \int_{-T/2}^{T/2} f(t) \cdot g(t+\tau)\,\mathrm{d}t \tag{2.15}$$

with g defined as f above. In this document, the term will be used to describe the interference of codes of the same family, i.e. f and g are different PN codes, both of the same family and of length L. In a multi-user environment, it is suggested that every user uses a different code to not directly disturb other users. Practically speaking, it is not possible to assign a different code to each user, as the number of available code for each family is roughly one order of magnitude less than the code length L. This means on the one hand that all sequences of a suitable family will be used, but on the other hand there will still be numerous users transmitting the same code. Ideally, CCF $= 0$ for all τ, i.e. users with different codes do not interfere each other. It can be shown that the ideal code family, i.e. a family that has ideal ACF and CCFs does not exist [24]. For this imaging application, the CCF is not as critical as for e.g. communication applications, because interfering users can be identified by other means as described in Sec. 3.6. In Fig. 2.10, it is clearly visible that CCFs for either form of m-sequence are far from ideal.

2.2.2 Resolution, Dynamic Range and Unambiguous Range

Resolution, dynamic range, and unambiguous range are important characteristic properties of radar systems. As all three properties are quoted in the following chapters, they will

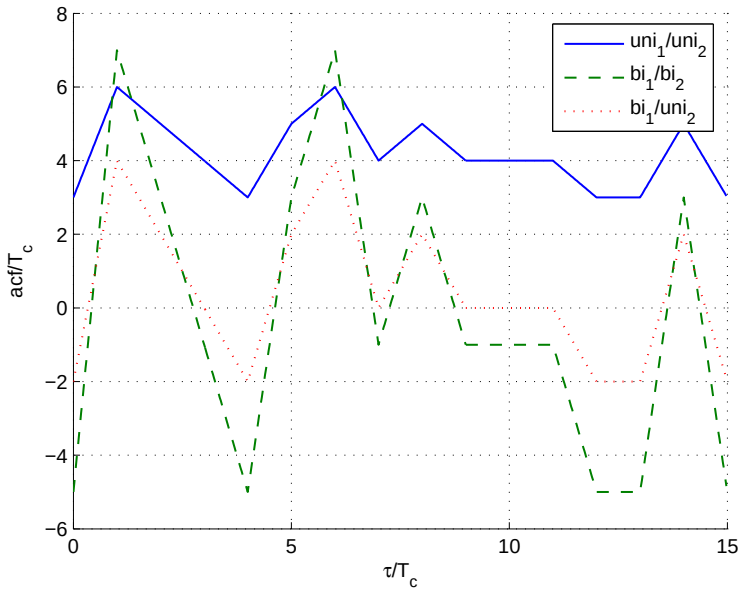

Fig. 2.10: Comparison of CCFs of a $L = 15$ bit m-sequence, uni- and bipolarly coded

be defined here. As resolution depends on the chosen pulse form, its influence will be discussed first.

Influence of the Pulse Form

With m_u and m_b from Eqs. 2.9 and 2.10 the baseband reference signal is defined as

$$x_\mathrm{u}(t) = m_\mathrm{u}(t) * p(t) \tag{2.16}$$

and the received signal as

$$x_\mathrm{b}(t) = m_\mathrm{b}(t) * p(t) \tag{2.17}$$

with $p(t)$ denoting the chosen normalized pulse form, i.e. $|p(t)| \leq 1$. With Eq. 2.11, the correlation of a received baseband signal $x_\mathrm{b}(t - z_1 T_\mathrm{c})$, i.e. there was only one target, with the reference x_u can be written as

$$\begin{aligned}
\varphi_{x_\mathrm{b}x_\mathrm{u}}(-\tau) &= \int_0^{LT_\mathrm{c}} x_\mathrm{b}(t - z_1 T_\mathrm{c}) \cdot x_\mathrm{u}(t - \tau)\,\mathrm{d}t = \\
&= x_\mathrm{b}(t - z_1 T_\mathrm{c}) * x_\mathrm{u}(-t) = \\
&\circ\!\!-\!\!\bullet\ \mathcal{F}\{x_\mathrm{b}(t - z_1 T_\mathrm{c})\} \cdot X_\mathrm{u}(-f) = \\
&= \mathcal{F}\{m_\mathrm{b}(t - z_1 T_\mathrm{c})\} \cdot P(f) \cdot M_\mathrm{u}(-f) \cdot P(-f) = \\
&= \mathcal{F}\{m_\mathrm{b}(t - z_1 T_\mathrm{c})\} \cdot M_\mathrm{u}(-f) \cdot P(f) \cdot P(-f) \\
&\bullet\!\!-\!\!\circ\ \varphi_{m_\mathrm{b}m_\mathrm{u}}(-\tau) * \varphi_{pp}(-\tau) = \varphi_{m_\mathrm{b}m_\mathrm{u}}(-\tau) * \varphi_{pp}(\tau)
\end{aligned} \tag{2.18}$$

From Eq. 2.18 it is clear that the ACF of a m-sequence that ran through pulse shaping is equivalent to the convolution of the ACF of a single pulse and the periodic ACF of a time discrete m-sequence. Fig. 2.11 shows three ACFs, namely for the sum of Dirac-pulses, the transmit pulse form, and the transmitted signal, i.e. the convolution of the sum of Dirac-pulses with the transmit pulse form.

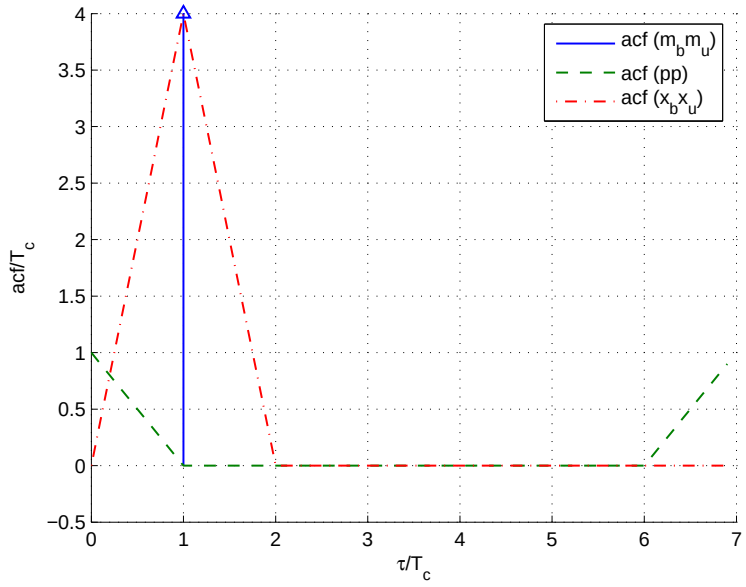

Fig. 2.11: Illustration of the dependency of the ACF on the pulse form, $L = 7\,\text{bit}$, m-sequence, uni- and bipolarly coded

Resolution and Precision

It is important to distinguish the terms resolution and precision. Precision will be used in this document to indicate the accuracy of the range detection for a single target environment. Clearly, for PN radars, precision depends solely on the step width of the correlator, i.e. $\Delta\tau$, and the detector properties. From the radar range equation Eq. 2.8, it is obvious that the precision writes as

$$\delta_\text{P} = \frac{\Delta\tau \cdot c_0}{2} \tag{2.19}$$

with the factor 2 resulting again from the return trip of the wave to the target. Eq. 2.19 is valid for a monostatic radar is a good approximation for a bistatic one, with small distances in between the sensors compared to the range of the target. The precision may be increased using interpolation techniques, but in general, for a multi-target environment this is not possible.

Influences of the detector cannot be described in general equations. It depends mainly on the ability to detect the peak, although it is corrupted by noise. Due to this fact it will be neglected here.

Resolution is defined for this document as the minimum distance between two targets, necessary to separate them. It is obvious that the resolution is deduced from the shape of the ACF. As shown in Sec. 2.2.2, the shape of the ACF depends on the pulse form used for transmission. To define resolution, rectangular shaped pulses will be assumed to keep the deduction figurative. Rectangular shapes result in triangular ACFs that are located at $\tau = -z_n T_\mathrm{c}$ as in Fig. 2.12. The width of each triangle is given by twice the pulse width, resulting from Eq. 2.5, as depicted in Fig. 2.12. Assuming two targets, roughly at the same distance, i.e. the same free space attenuation is assumed, that are characterized by radar cross sections (RCS) σ_1 and σ_2, the absolute of the gradient of the edges of triangle 1 derives as σ_1/T_c and that of triangle 2 as σ_2/T_c. The peak detector as described in Sec. 2.6.3 is configured with a certain peak excursion δ. Two peaks can only be separated, if the function drops by at least δ in between the peaks. The resolution δ_R of two targets, therefore depends strongly on the parameter δ and ranges in between $T_\mathrm{c} < \delta_\mathrm{R}/c_0 \leq 2T_\mathrm{c}$. The factor 2 is caused by the fact that the wave travels forth and back between the targets. Thus the resolution for rectangular shaped pulses is $\delta_\mathrm{R} \leq T_\mathrm{c} \cdot c_0$. The resolution can generally be written as

$$\frac{\mathrm{d}}{\mathrm{d}t}\left(\sigma_1 \varphi_{pp}(t) + \sigma_2 \varphi_{pp}\left(t - \frac{2\delta_\mathrm{R}}{c_0}\right)\right)\bigg|_{t=t_\mathrm{min}} \stackrel{!}{=} 0 \tag{2.20}$$

and

$$\sigma_1 \varphi_{pp}(t_\mathrm{min}) + \sigma_2 \varphi_{pp}\left(t_\mathrm{min} - \frac{2\delta_\mathrm{R}}{c_0}\right) \leq \min(\sigma_1,\sigma_2) - \delta \tag{2.21}$$

with φ_{pp} the ACF of the pulse. Eq. 2.20 describes the minimum in between the peaks $\tau = z_1 T_\mathrm{c}$ and $\tau = z_2 T_\mathrm{c}$ by postulating the derivative to be zero. With $t_\mathrm{min}(\delta_\mathrm{R})$ calculated from Eq. 2.20, Eq. 2.21 can be solved for δ_R.

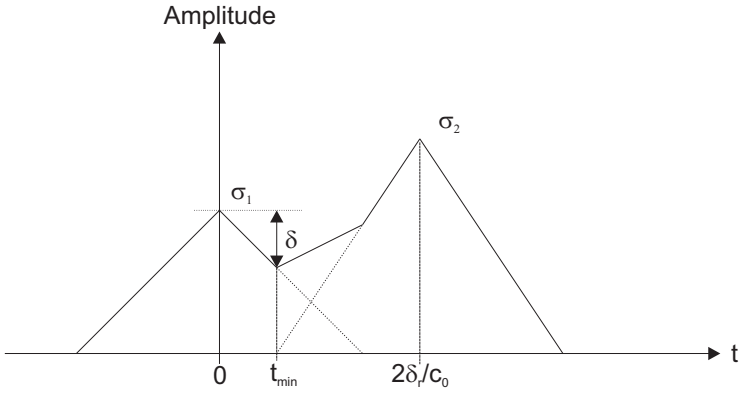

Fig. 2.12: Resolution for rectangular pulses, i.e. triangular φ_{pp}

Dynamic Range

The dynamic range of a radar system is an important characteristic. It is clear from Eq. 3.8 that the amplitude of the received signal can vary by several orders of magnitude. On the one hand, the amplitude of the received signal is proportional to r^{-4}, with r the distance between target and radar module. On the other hand, the radar cross section (RCS) of common objects varies enormously with the aspect angle as shown in Sec. 4.2.1. This section does not only treat the dependence on the aspect angle but also the influence of object geometry and properties such as conductivity.

Unambiguous Range

For every radar system the unambiguous range is defined. For pulse radars, it is derived from the pulse repetition frequency (PRF) as already mentioned and depicted in Fig. 2.2. In PN-radars, the corresponding time to 1/PRF is LT_c, i.e. the duration of a whole spreading sequence. The unambiguous range d_unamb is the distance that a wave can travel twice within LT_c, i.e.

$$d_\mathrm{unamb} = \frac{1}{2} c_0 \cdot LT_\mathrm{c}. \tag{2.22}$$

The range of targets within this area can be measured unambiguously. Targets further away may be detected, if the received signal is strong enough, but their range will be determined as

$$d_\mathrm{d} = d - k \cdot d_\mathrm{unamb} \tag{2.23}$$

with d the true range, d_d the detected range, and $k \in \mathbb{N}$. The unambiguous range results from the maximum time the system waits for an answer of the target. For a pulse radar, this time is derived from the PRF, whereas for PN radars it depends on the code length.

As the freedom to choose T_c already went into fixing the precision of the system, the remaining possibility to adjust the unambiguous range is the code length L. Increasing L not only yields a greater unambiguous range, but also increases the peak of the ACF, according to Eq. 2.7. On the other hand, for analog correlations, the needed time increases with L^2. This results from the principle that for each discrete point of the ACF, the sequence needs to be transmitted completely. Sec. 4.1.1 treats the realization of an analog correlator in detail. In case extremely fast and high precision analog to digital converters (ADCs) were available, e.g. 10 GS/s at 18 bit, the received signal could be digitized and then correlated in a microprocessor using the frequency domain correspondence from Eq. 2.18. This method would provide significantly faster correlation results and only a linear dependency on the code length.

2.3 Antennas

Antenna properties play a vital role for the radar system. Several standard requirements for antennas, such as high efficiency and high gain, apply as well as numerous additional

ones, especially when the radar system is set into relation with the automotive industry. As the imaging algorithm in Sec. 3 is based on the response of several single sensors, it is necessary to have a certain degree of diversity between the sensors. As the algorithm is based on the assumption of quasi-constant RCS for all sensors, diversity can be realized by different locations and/or different characteristics for the sensor antennas. Several publications propose suggestions for antennas usable in automotive radar systems [25–27], but again a main aspect, besides the basic functionality, will be the production cost of the device.

2.3.1 Location

Location diversity will be investigated first. For the following section, a single target is assumed, i.e. there are no problems assigning sensor outputs to targets. The problem arises, if two targets are separated by less than the distance between two sensors. This topic is treated in Sec. 3.2. Location diversity can be used for imaging by using trilateration techniques as described in Sec. 3.2.4. Figuratively, every sensor detects a different distance to the target. Assuming the distance information from the sensor has zero tolerance, the target is exactly located on the intersection of circles around each sensor. The respective circle has a radius equal to the detected target distance. Fig. 2.13 shows the described trilateration principle with zero tolerance distance information and a single target. In

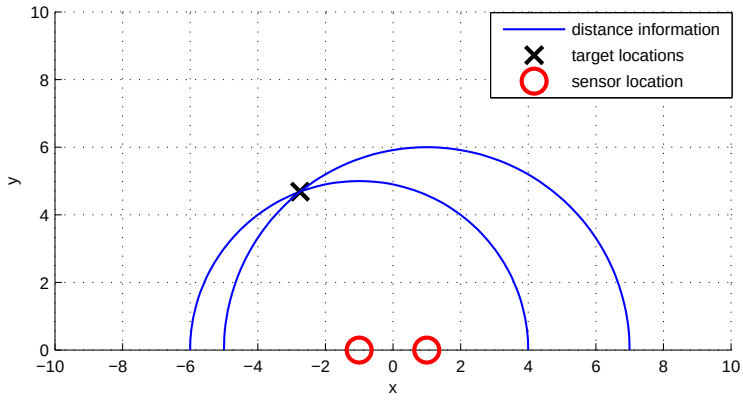

Fig. 2.13: Simplified schematic of the trilateration principle

opposition to the above mentioned, real world scenarios show two main problems:

- Distance information is not exact, e.g. corrupted by noise or discretization.
- With multiple distance information from each sensor, due to multiple targets, combining the corresponding distances is far from trivial.

The problem of noise is common to every system engineer. It can be treated using standard techniques such as averaging and calculating location probabilities instead of precise coordinates. The other problem is severe. Using superresolution techniques as in [8], it

is assumed that the number of antennas N_A is greater than the number of targets N_T. Clearly, $N_A > N_T$ cannot be assumed here, as in a roadside scenario multiple scattering centers, such as cars, pedestrians, trees, and buildings, exist. The approach to solve this problem is described in Sec. 3.2.

Distance between receiver antennas must be on the order of several times the resolution, to obtain a good location diversity. With reference to Sec. 4.2.1, large distances between the sensor antennas deliver not only the advantage of high diversity. As objects in a real roadside scenario do not resemble isotropic objects such as spheres, it cannot be assumed that their RCS is constant for all angles of incidence. Even worse, cars or guard rails often exhibit metal edges, which are responsible for dramatic changes of RCS over the angle of incidence. Furthermore, different location and different characteristics of the antennas, see Sec. 2.3.2, can influence the amplitude of the received signal. With knowledge of the antenna characteristics, this effect can be compensated. Studies were conducted on whether it is possible to calculate this change in RCS for common roadside objects, see Sec. 4.2.1, but the task appeared too complex, for treatment under the topic of this work. To conclude the discussion about the ideal distance between the sensors, it is important to mention the trade off: large distance means high diversity and therefore high imaging precision, low distance means low diversity but a roughly constant aspect angle for the target and therefore constant RCS. When talking about automotive radar, the sensor location is limited by the given mounting space. For a car this will presumably be the bumper, so its width limits the location too. Finally, to mention some numbers, rough estimations show that exploiting the standard width of a car of approximately 2 m for 3 or more sensors, is a good trade off, between location diversity and keeping the RCS constant for typical target distances. A 1 m distance between two sensors means a difference in aspect angle for an object that is located 5 m straight ahead, of roughly 10° for the worst case.

2.3.2 Characteristics

As mentioned above, diversity can also be implemented by using different antenna characteristics for different sensors. Unfortunately it is not as powerful as location diversity for radar imaging. This is a result of the reduced precision of the measured amplitude compared to the distance measurement. Though precise amplitude measurement is in general a feasible task, it is difficult in this case, as it is not the amplitude itself to be measured, but the change in amplitude due to the antenna characteristic. Furthermore, changes in aspect angle, and therefore changes of the RCS influence the amplitude significantly. According to Eq. 3.8, besides the antenna characteristics, the distance and the RCS influence the amplitude of the received signal. Even though the influence of the different distances can be calculated using the sensor distance information, there remains the problem of the RCS. As mentioned above, there is no alternative to assuming the RCS constant for all sensors. With these problems solved, the knowledge of the antenna characteristics can be used to calculate the angle of the target. Clearly, with real world characteristics, i.e. a non-isotropic radiator, each angle of incidence has its specific gain value, as $G(\varphi,\vartheta)$ is a function

of elevation and azimuth angle. Fig. 2.14 shows the characteristic of a so called Rampart antenna. It was studied and presented during a student master thesis in [28]. It was designed with regard to using it in automotive environment for a 24 GHz radar. Rampart

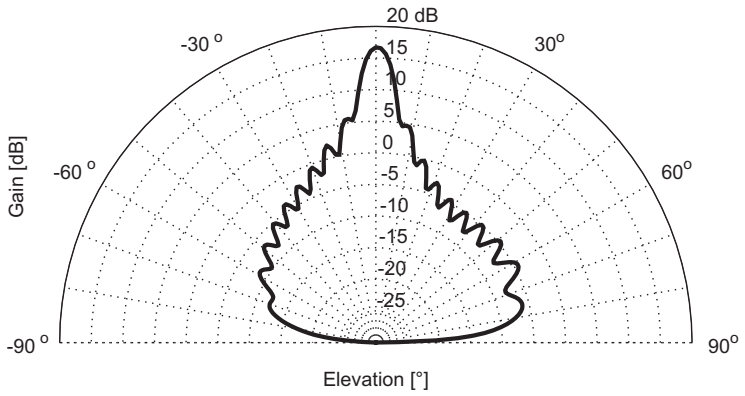

Fig. 2.14: Gain of a left hand side circularly polarized Rampart antenna at 24.1 GHz

antennas meet all essential requirements for the proposed application in automotive radar systems.

Clearly, for any imaging algorithm, it is important that the number of independent pieces of information on the object location is greater or equal to the number of degrees of freedom for the object location, i.e. at least two independent sensors for a 2D scenario. So with three sensors and a 2D scenario, the system is four times overdetermined, i.e. three range values and three amplitude values to determine x- and y-position. The situation allows the usage of the additional information to increase the precision. So additional information helps to reduce the influence of different noise effects. The most important factor of disturbance is the matching of detected targets from the different sensors as mentioned in Sec. 3.5. So exploiting the gain diversity as in the example of Fig. 2.15, allows target location via different methods. In case the different methods lead to the same position, it is likely that current combination of sensor information refers to a real target. As the system is four times overdetermined, a double target location is even possible, if one sensor is blind for a certain target. To use gain diversity for target location, a highly different gain for different aspect angles is required, i.e. the change in gain shall dominate in Eq. 3.8 over the change in RCS. This yields automatically narrower beams and therefore less coverage of the scenario. The sample antenna configuration contains a 60° beamwidth antenna for the central sensor and two 30° beamwidth antennas at the outer sensors that have a few degrees of inclination. The effect of this configuration is that targets straight ahead cause a strong response for all three sensors, whereas non-central objects still result in strong radar responses for two sensors, which is sufficient for the system. The algorithm in Sec. 3.4 is based on the assumption that the changes in antenna characteristic over aspect angle is for at least two sensors greater than the change in RCS. Designing the antennas in an appropriate way helps satisfying this condition for as many objects as possible.

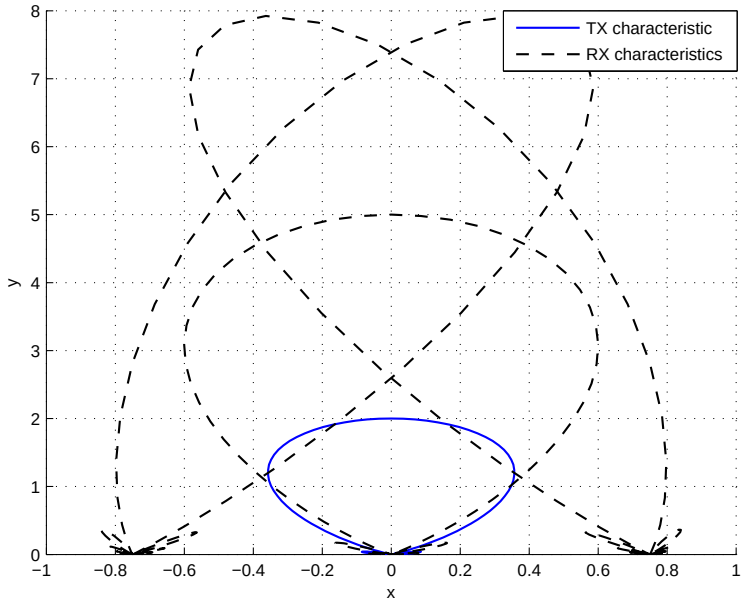

Fig. 2.15: Proposed antenna characteristics for a three RX-antenna system

Polarization

Regarding the polarization, neither direction of polarization can be prioritized. Therefore, it would be a strategic choice, if circularly polarized antennas were chosen. In case vertical polarization is not reflected by a target or converted into horizontal by a polarizer, only a 3 dB loss occurs instead of the entire signal. The same is of course valid vice versa. Unfortunately, there are situations that cannot be handled by this configuration. Given the fact of vertical polarization being reflected without a change in phase and horizontal polarization being reflected with a phase difference of 180° leads to a change from left hand circular polarization to a right hand one or vice versa. This situation requires complex target shapes and materials and is only valid for certain incident angles so that it can be neglected. Finally, it can be concluded that circularly polarized antennas are eligible for use in automotive radar imaging systems.

2.3.3 Structural Shape

With respect to its designated use in automotive environments, certain constraints regarding the structural shape apply. To fulfill the above mentioned requirements concerning placement, the car bumpers are suggested for mounting the antennas. Not only are they generally made of a material that has a high transmission coefficient for the ISM frequencies under examination, but they allow mounting over the complete width of the vehicle. Furthermore their height above the road is considered ideal with respect to reflection from the road. As already mentioned, the characteristics of the antennas are kept narrow in vertical direction to avoid detection of ghost targets resulting from surface reflections. Al-

though a narrow vertical characteristic is required, the mounting prerequisites, especially the available depth, strongly suggest using microstrip planar antennas. Microstrip planar antennas for use in automotive radar systems were investigated in [28].

2.4 Correlator

As already shown in Sec. 2.2, the correlation of a unipolarly coded m-sequence with the same bipolarly coded sequence exhibits a theoretically infinite main-to-side-lobe ratio. For practical reasons, unipolarly coded sequences are extremely difficult to handle, as they are easily corrupted by DC offsets. As will be shown in Sec. 2.4.2, DC offsets cancel out weaker targets.

2.4.1 Correlating at the Intermediate Frequency

Usually the received signal is mixed to an intermediate frequency (IF) and then detected. The resulting baseband signal is correlated with a baseband reference from the code generator. For baseband correlators, bipolarly coded sequences are preferred. For long sequences, the mean approaches zero according to Eqs. 2.13 and 2.14 with $L_c \to \infty$. Therefore, the DC offset can be isolated by evaluating the mean. Subtracting the mean from the signal yields the uncorrupted signal. The method is also applicable for superimposed signals such as the received signal, but is exact only for infinite sequences. To eliminate this shortcomings, different approaches were studied. [23] proposes the use of a serial combination of different codes. The codes are chosen so that the sum over the correlations of the different codes is zero mean. The disadvantage of this method is the cycle time. The method requires the scenario to be quasi-constant over the complete series of codes. The amount of codes added to a series is on the order of the length of the single sequence, i.e. for a $L = 1023$ bit sequence, the scenario needs to be constant over roughly 1023^2 bits. For a chip duration of 1 ns, i.e. roughly a bandwidth of 1 GHz, this results in 1 ms, that is required to only transmit the complete series. Although there are ways to reduce the amount of time, an analog correlation needs, in general, it will be on the order of L^2 chip durations. This makes clear that an image update rate, i.e. the rate at which the image of the complete scenario can be updated, of 100 Hz, a number given by the automotive industry for pre-crash detection, is hardly accomplishable. To avoid this prerequisite and the large amount of correlations, which reduces the image update rate, a different approach, as proposed in [29], is investigated here.

The following calculations are kept simple by taking only one target into account. Unless otherwise stated, the equations write as sums for multiple targets and are therefore valid for a multi-target environment. Instead of correlating two baseband signals, the IF signals are correlated. At first this has the advantage that a detector for the received signal is not necessary. On the other hand, the reference signal needs to be modulated onto an

IF carrier. The received signal can be written as

$$s'_{\mathrm{rec}}(t) = \Re\Big\{\cos\big((\omega_{\mathrm{c}} \pm \omega_0)\, t\big) \cdot \ \big[A_1 \cdot g(t - z_1 T_{\mathrm{c}}) + A_2 \cdot g(t - z_2 T_{\mathrm{c}}) + \ldots\big]\Big\} \tag{2.24}$$

where $A_n = |A_n| \cdot \exp(j\zeta_n)$. ζ_n accounts for complex RCS and $\cos((\omega_{\mathrm{c}} \pm \omega_0)\, t)$ is the local oscillator (LO) frequency that is applied to the mixer. $n = 0$ denotes the reference and $n = 1, \ldots, N$ the radar targets. The transmitted signal is written as

$$g(t) = x_{\mathrm{b}}(t) \cdot \cos(\omega_{\mathrm{c}} t) \tag{2.25}$$

with x_{b} from Eq. 2.17 giving the received signal for a zero distance, unit reflectance target. With ω_0 the intermediate frequency,

$$h_{\mathrm{I}}(t) = x_{\mathrm{u}}(t) \cdot \cos(\omega_0 t) \tag{2.26}$$

denotes the reference IF signal function and

$$s_{\mathrm{ref,I}}(t) = \Re\big\{A_0 \cdot h_{\mathrm{I}}(t)\big\} = |A_0| \cdot x_{\mathrm{u}}(t) \cdot \cos(\omega_0 t + \vartheta_0) \tag{2.27}$$

the reference signal. The mixer output signal $s'_{\mathrm{rec}}(t)$ is low-pass filtered so that

$$s_{\mathrm{rec}}(t) = |A_1| \cdot x_{\mathrm{b}}(t - z_1 T_c) \cdot \cos(\omega_0 t + \vartheta_1) + |A_2| \cdot x_{\mathrm{b}}(t - z_2 T_c) \cdot \cos(\omega_0 t + \vartheta_2) + \ldots \tag{2.28}$$

is obtained, with

$$\vartheta_n = \omega_{\mathrm{c}} z_n T_{\mathrm{c}} - \zeta_n. \tag{2.29}$$

The signals $s_{\mathrm{rec}}(t)$ and $s_{\mathrm{ref,I}}(t)$ are now being correlated. A block diagram showing the concept of a correlator at intermediate frequency corresponding to these calculations is shown in Fig. 2.16. The correlation for the IF signals with one target according to Eq. 2.7

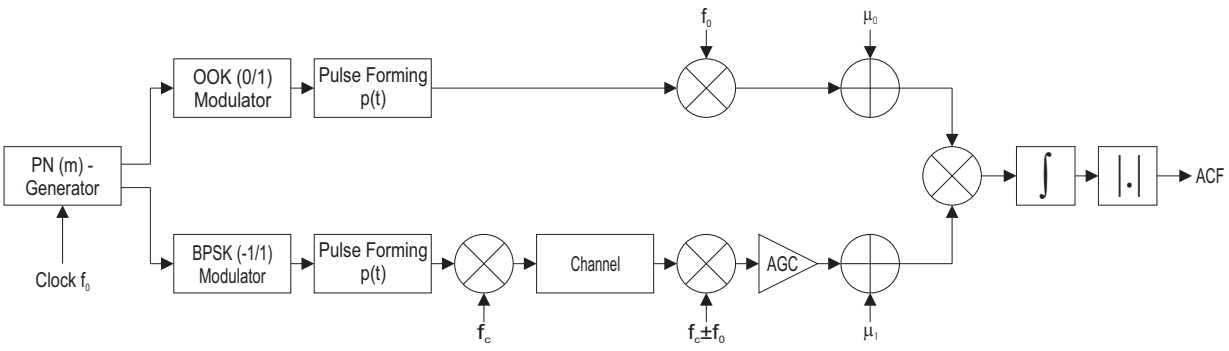

Fig. 2.16: Block diagram of a correlator at intermediate frequency

writes as

$$\begin{aligned}\varphi_{s_{\mathrm{rec}}s_{\mathrm{ref,I}}}(\tau) &= \int_0^{LT_\mathrm{c}} s_{\mathrm{rec}}(t)\cdot A_0\cdot x_u\left(t+\tau\right)\cdot\cos\left(\omega_0 t+\vartheta_0\right)\mathrm{d}t = \\ &= |A_0||A_1|\int_0^{LT_\mathrm{c}} x_\mathrm{b}\left(t-z_1T_\mathrm{c}\right)\cdot x_\mathrm{u}\left(t+\tau\right)\cdot\underbrace{\cos\left(\omega_0 t+\vartheta_1\right)\cdot\cos\left(\omega_0 t+\vartheta_0\right)}_{\frac{1}{2}\left[\cos(\vartheta_0-\vartheta_1)+\cos(\omega_0 2t+\vartheta_0+\vartheta_1)\right]}\mathrm{d}t = \\ &= \underbrace{\frac{|A_0||A_1|}{2}\cdot\cos\left(\vartheta_0-\vartheta_1\right)\cdot\varphi_{x_\mathrm{b}x_\mathrm{u}}\left(\tau\right)}_{\varphi_\mathrm{cos}}+ \\ &+ \underbrace{\frac{|A_0||A_1|}{2}\int_0^{LT_\mathrm{c}} x_\mathrm{b}\left(t-z_1T_\mathrm{c}\right)\cdot x_\mathrm{u}\left(t+\tau\right)\cdot\cos\left(2\omega_0 t+\vartheta_0+\vartheta_1\right)\mathrm{d}t}_{\gamma_\mathrm{cos}}.\end{aligned} \tag{2.30}$$

Clearly Eq. 2.30 comes to a result that has a couple of disadvantages.

IQ-Correlation First, the desired term $A_0A_1\varphi_{x_\mathrm{b}x_\mathrm{u}}$ is multiplied with a cos function. The argument of the cos depends on the sum of a system immanent phase constant ϑ_0 and a variable phase ϑ_n that depends on the respective target distance and RCS. Obviously, it cannot be guaranteed that $\vartheta_0+\vartheta_1\neq(2k-1)\pi$, $k\in\mathbb{N}$, i.e. the cos term has a non-zero value. Furthermore, a term that depends on the carrier frequency and the current target distance cannot be accepted for the imaging algorithm. To avoid this cos term, a second correlation path is introduced. In contrast to the in-phase correlation Eq. 2.30, the received signal will be correlated with

$$s_{\mathrm{ref,Q}}(t)=\Re\big\{A_0\cdot h_\mathrm{Q}(t)\big\}=|A_0|\cdot x_\mathrm{u}\left(t\right)\cdot\sin\left(\omega_0 t+\vartheta_0\right) \tag{2.31}$$

instead of $s_{\mathrm{ref,I}}$. A block diagram for the IQ correlator at the intermediate frequency is shown in Fig. 2.17. The result of the quadrature-phase correlation writes as

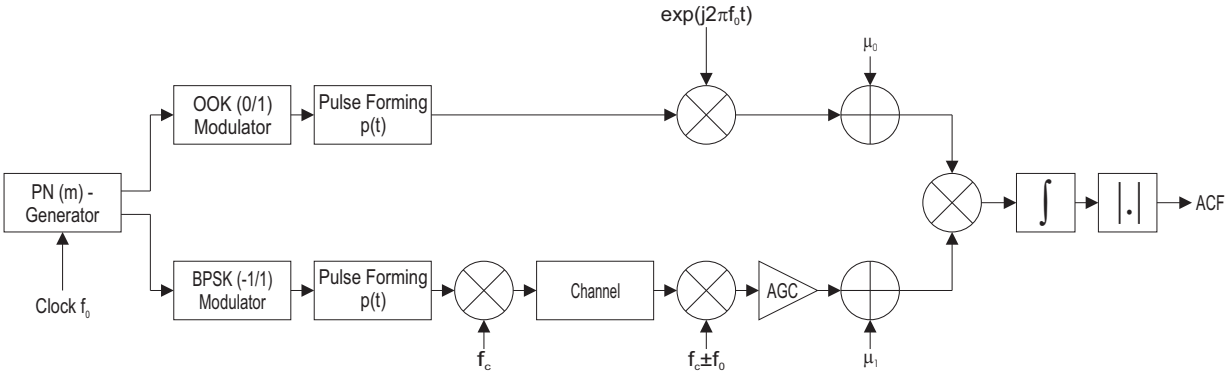

Fig. 2.17: Block diagram of an IQ correlator at intermediate frequency

$$\varphi_{s_{\mathrm{rec}}s_{\mathrm{ref,Q}}}(\tau) = \int_0^{LT_\mathrm{c}} s_{\mathrm{rec}}(t) \cdot A_0 \cdot x_u\left(t+\tau\right) \cdot \sin\left(\omega_0 t + \vartheta_0\right) \mathrm{d}t = \tag{2.32}$$

$$= |A_0||A_1| \int_0^{LT_\mathrm{c}} x_\mathrm{b}\left(t - z_1 T_\mathrm{c}\right) \cdot x_\mathrm{u}\left(t+\tau\right) \cdot \underbrace{\cos\left(\omega_0 t + \vartheta_1\right) \cdot \sin\left(\omega_0 t + \vartheta_0\right)}_{\frac{1}{2}\left[\sin(\vartheta_0-\vartheta_1)+\sin(\omega_0 2t+\vartheta_0+\vartheta_1)\right]} \mathrm{d}t =$$

$$= \underbrace{\frac{|A_0||A_1|}{2} \cdot \sin\left(\vartheta_0 - \vartheta_1\right) \cdot \varphi_{x_\mathrm{b}x_\mathrm{u}}\left(\tau\right)}_{\varphi_{\sin}} +$$

$$\underbrace{+ \frac{|A_0||A_1|}{2} \int_0^{LT_\mathrm{c}} x_\mathrm{b}\left(t - z_1 T_\mathrm{c}\right) \cdot x_\mathrm{u}\left(t+\tau\right) \cdot \sin\left(2\omega_0 t + \vartheta_0 + \vartheta_1\right) \mathrm{d}t}_{\gamma_{\sin}}.$$

It becomes clear now that if $\gamma_{\cos}$ and $\gamma_{\sin}$ were zero, the desired $\varphi_{x_\mathrm{b}x_\mathrm{u}}$ could be extracted by calculating the absolute of the IQ correlation result, i.e.

$$\sqrt{\varphi^2_{s_{\mathrm{rec}}s_{\mathrm{ref,I}}} + \varphi^2_{s_{\mathrm{rec}}s_{\mathrm{ref,Q}}}} = \frac{|A_0||A_1|}{2}\varphi_{x_\mathrm{b}x_\mathrm{u}} \quad \text{for} \quad \gamma_{\cos} = \gamma_{\sin} = 0. \tag{2.33}$$

It will be shown later that the above mentioned assumption can be made if pulse form and intermediate frequency adhere to certain constraints. For the real world case of multiple targets, Eq. 2.33 can be used, although problems may arise. Eqs. 2.30 and 2.32 can be written as sums over N terms, N the number of targets, where each term resembles $\varphi_{\cos}$ and $\varphi_{\sin}$ respectively. As the ACF $\varphi_{s_{\mathrm{rec}}s_{\mathrm{ref,I}}}$ has no side lobes, the square of the superimposed term equals the sum of the square of the ACF of each target. This is valid, if the minimum distance between two targets is $2T_\mathrm{c}$, and the pulse width is limited to T_c. This is deduced from the fact that $\varphi_{x_\mathrm{b}x_\mathrm{u}}$ has a $2T_\mathrm{c}$ wide peak around $\tau = z_n T_\mathrm{c}$, but is zero for all other τ. For the case that the ACF of two targets overlap, i.e. $z_n - z_{n+1} < 2$ or infinite impulse

response (IIR) pulses, Eq. 2.33 with two targets must be written as

$$\varphi^2_{s_{\mathrm{rec}}s_{\mathrm{ref,I}}} + \varphi^2_{s_{\mathrm{rec}}s_{\mathrm{ref,Q}}} = \left(\frac{|A_0||A_1|}{2}\varphi_{x_\mathrm{b}x_\mathrm{u}}\left(\tau - l_1T_\mathrm{c}\right)\right)^2 + \left(\frac{|A_0||A_2|}{2}\varphi_{x_\mathrm{b}x_\mathrm{u}}\left(\tau - l_2T_\mathrm{c}\right)\right)^2 + \frac{|A_0||A_1|}{2}\frac{|A_0||A_2|}{2}\varphi_{x_\mathrm{b}x_\mathrm{u}}\left(\tau - l_1T_\mathrm{c}\right)\varphi_{x_\mathrm{b}x_\mathrm{u}}\left(\tau - l_2T_\mathrm{c}\right)\cdot \underbrace{\left(\cos\left(\vartheta_0-\vartheta_1\right)\cos\left(\vartheta_0-\vartheta_2\right)+\sin\left(\vartheta_0-\vartheta_1\right)\sin\left(\vartheta_0-\vartheta_2\right)\right)}_{\cos(\vartheta_1-\vartheta_2)}. \tag{2.34}$$

It becomes clear that the additional term is not constant as $\cos(\vartheta_1 - \vartheta_2)$ oscillates with changes in distance between the targets on the scale of the carrier wavelength. Assuming $f_\mathrm{c} = 24\,\mathrm{GHz}$, 3 mm correspond to $\pi/2$, so even the phase difference of static targets will change significantly unless they are aligned straight ahead, i.e. the aspect angle does not change during the approach. This mixed term might appear in the imaging system as a ghost target, but with its heavy fluctuation in amplitude, it can easily be identified by the algorithm.

Intermediate frequency Second, the terms $\gamma_{\cos}$ and $\gamma_{\sin}$ respectively need to be avoided. The sinusoidal part in both terms depends on the argument $2\omega_0 t + \vartheta_0 + \vartheta_1$. Furthermore, an integration over the complete term is performed. These facts brought up the question, whether the equation

$$\int_0^{1/f_0} \cos(2\pi f_0 t)\mathrm{d}t = 0 \tag{2.35}$$

can be exploited. Sec. 2.4.3 will show in detail under which prerequisite the γ-terms can be neglected. This prerequisite is by name the choice of the proper intermediate frequency, depending on the pulse form.

2.4.2 Influence of Noise and DC Offset

In the following, an estimation of the signal-to-noise ratio (SNR) at the correlator output will be derived. It will depend on a given level of additive white Gaussian noise (AWGN) or DC offset at the correlator input ports. Again, the equations describe only an environment with a single target.

Noise

First, the noise problem will be treated. As already mentioned, we assume AWGN, $n(t)$, in the received signal path. With

$$s_{\mathrm{rec,n}}(t) = |A_1| \cdot x_\mathrm{b}\left(t - z_1T_\mathrm{c}\right) \cdot \cos\left(\omega_0 t + \vartheta_1\right) + n\left(t\right) \tag{2.36}$$

the in-phase correlator output writes as

$$\varphi_{s_{\mathrm{rec,n}}s_{\mathrm{ref,I}}}(\tau) = \int_0^{LT_\mathrm{c}} \left[s_\mathrm{rec}(t) + n(t)\right] \cdot s_\mathrm{ref,I}(t+\tau)\,\mathrm{d}t = \varphi_{s_\mathrm{rec}s_\mathrm{ref,I}} + \varphi_{ns_\mathrm{ref,I}}. \tag{2.37}$$

This section will treat only $\varphi_{ns_\mathrm{ref,I}}$, as $\varphi_{s_\mathrm{rec}s_\mathrm{ref,I}}$ has already been investigated. As already mentioned, the described PN principle corresponds to a matched filter receiver. Therefore, the SNR considerations will be focused on the sampling instance. Matched filter systems are optimized, so that the SNR is maximal at the sampling instance. The point in time under investigation for the correlator output is therefore the maximum in $\varphi_{s_\mathrm{rec}s_\mathrm{ref}}$, i.e. $\tau = z_1 T_\mathrm{c}$. Assuming $n(t)$ a stochastic process, the average noise power P_N resulting from Eq. 2.36 can be written as

$$P_\mathrm{N} \leq 2 \cdot \mathcal{E}\left\{\varphi^2_{ns_\mathrm{ref,I}}\right\} = 2 \cdot \mathcal{E}\left\{\left[\int_0^{LT_\mathrm{c}} n(t) \cdot s_\mathrm{ref,I}(t+\tau)\,\mathrm{d}t\right]^2\right\} \tag{2.38}$$

with the factor 2 resulting from the addition of the sin- and cos-terms. The argument of the expected value operator can be estimated as follows

$$\left[|A_0| \int_0^{LT_\mathrm{c}} n(t) \cdot x_\mathrm{u}(t+\tau) \cdot \cos(\omega_0 t + \vartheta_0)\,\mathrm{d}t\right]^2 \leq \tag{2.39}$$
$$|A_0|^2 \cdot \left[\int_0^{LT_\mathrm{c}} |n(t) \cdot x_\mathrm{u}(t+\tau) \cdot \cos(\omega_0 t + \vartheta_0)|\,\mathrm{d}t\right]^2$$

as all functions are real. Substituting a real positive function within an integral by its maximum value gives an upper limit as in

$$|A_0|^2 \cdot \left[\int_0^{LT_\mathrm{c}} |n(t) \cdot x_\mathrm{u}(t+\tau) \cdot \cos(\omega_0 t + \vartheta_0)|\,\mathrm{d}t\right]^2 = \tag{2.40}$$
$$|A_0|^2 \cdot \left[\int_0^{LT_\mathrm{c}} |n(t)| \cdot |x_\mathrm{u}(t+\tau) \cdot \cos(\omega_0 t + \vartheta_0)|\,\mathrm{d}t\right]^2 \leq |A_0|^2 \left[\int_0^{LT_\mathrm{c}} |n(t)|\,\mathrm{d}t\right]^2$$

with $\max(x_\mathrm{u}\cos(\omega_0 t + \vartheta_0)) = 1$. Using the triangle inequality, the following step is possible for $n(t)$ a real function

$$|A_0|^2 \left[\int_0^{LT_\mathrm{c}} |n(t)|\,\mathrm{d}t\right]^2 \leq |A_0|^2 \int_0^{LT_\mathrm{c}} n^2(t)\,\mathrm{d}t. \tag{2.41}$$

With the definition of the expected value operator from [30], the average noise power can be estimated as

$$P_{\mathrm{N}} \leq 2 \cdot |A_0|^2 \, \mathcal{E} \left\{ \int_0^{LT_{\mathrm{c}}} n^2(t) \, \mathrm{d}t \right\} \leq 2 \cdot |A_0|^2 \int_0^{LT_{\mathrm{c}}} \mathcal{E} \left\{ n^2(t) \right\} \mathrm{d}t = 2 \cdot |A_0|^2 \cdot LT_{\mathrm{c}} \cdot \sigma^2 \tag{2.42}$$

with $\mathcal{E}\left\{ n(t)^2 \right\} = \sigma^2$, the average noise power. From Eq. 2.42, the SNR at the sampling instance is derived as

$$\mathrm{SNR}_{\mathrm{out}} \geq \frac{P\left(\varphi_{s_{\mathrm{rec}} s_{\mathrm{ref}}}\right)}{P\left(\varphi_{n s_{\mathrm{ref}}}\right)} = \frac{\frac{|A_0|^2 |A_1|^2}{4} \varphi^2_{x_{\mathrm{b}} x_{\mathrm{u}}}(\tau = z_1 T_{\mathrm{c}})}{2 \cdot |A_0|^2 \cdot LT_{\mathrm{c}} \cdot \sigma^2} = \frac{|A_1|^2 \, \varphi^2_{x_{\mathrm{b}} x_{\mathrm{u}}}(\tau = z_1 T_{\mathrm{c}})}{8 LT_{\mathrm{c}} \cdot \sigma^2} \tag{2.43}$$

For rectangular pulses $p(t) = \mathrm{rect}(t/T_{\mathrm{c}})$,

$$\varphi_{x_{\mathrm{b}} x_{\mathrm{u}}}(\tau = z_1 T_{\mathrm{c}}) = N_{\mathrm{H}} T_{\mathrm{c}} \tag{2.44}$$

can easily be derived. In addition, it is clear that $\mathrm{SNR}_{\mathrm{in}}$, i.e. the SNR at the correlator input, depends only on the mean power of s, i.e. the mean power of a pulse, and σ^2. Eq. 2.44 leads to

$$\mathrm{SNR}_{\mathrm{out}} \geq \frac{|A_1|^2 \, T_{\mathrm{c}}^2 N_{\mathrm{H}}^2}{8 LT_{\mathrm{c}} \cdot \sigma^2} \propto L. \tag{2.45}$$

This makes clear that $\mathrm{SNR}_{\mathrm{out}}$ increases linearly with L, whereas $\mathrm{SNR}_{\mathrm{in}} = \frac{|A_1|^2}{\sigma^2}$ does not depend on the code length. For Gaussian shaped pulses, i.e. $p(t) = \exp\left(\frac{-t^2 \cdot \pi}{T_{\mathrm{c}}^2 \alpha_G^2}\right)$, $\mathrm{SNR}_{\mathrm{out}}$ can be calculated using

$$\varphi_{x_{\mathrm{b}} x_{\mathrm{u}}}(\tau = z_1 T_{\mathrm{c}}) = N_{\mathrm{H}} \int_{T_{\mathrm{c}}/2}^{T_{\mathrm{c}}/2} |p(t)|^2 \, \mathrm{d}t = N_{\mathrm{H}} \frac{\alpha_G T_{\mathrm{c}}}{\sqrt{2\pi}} \int_{-\sqrt{2\pi}}^{\sqrt{2\pi}} \exp\left(-u^2\right) \mathrm{d}u = N_{\mathrm{H}} \frac{\alpha_G T_{\mathrm{c}}}{\sqrt{2}} \, \mathrm{erf}\left(\frac{\sqrt{2\pi}}{\alpha_G} \right). \tag{2.46}$$

For correct treatment of the noise problem, the A/D converter at the correlator output, which is described in Sec. 2.5, needs to be taken into account. Quantization noise through the ADC adds to the WGN, but is neglected here. Depending on the chosen quantization method, the additional noise can be calculated. The exact derivation is only possible with a known amplitude distribution. The standard assumption of uniform amplitude distribution over the quantization vector cannot be assumed, due to the properties of the ACF.

DC Offset

DC offsets at the correlator output have a large influence on the dynamic range, because detectors are less sensible for weak signals if an offset is superimposed as illustrated in Fig. 2.18 and explained in Sec. 2.5. As already mentioned, for radar applications, dynamic ranges of over 60 dB, i.e. a comparable main-to-side-lobe ratio for the strongest signals, are

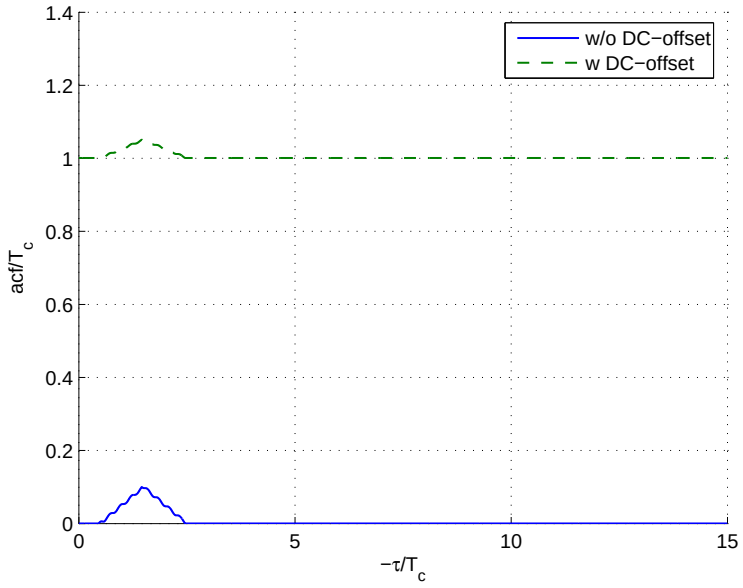

Fig. 2.18: Comparison of DC offset corrupted ACF with a noiseless ACF

required. So it is of vital importance to avoid any offsets. DC Offsets can be suppressed for long bipolar codes using DC blocks as already mentioned in Sec. 2.2.1. For the proposed correlator, both conditions are not fulfilled. On the other hand, the correlator inputs are IF ports, so DC blocks at the input ports can be used. Offsets caused by electronic devices and superimposed on the IF signals can be filtered this way. Furthermore, as DC blocks are far from perfect and high dynamic ranges are necessary, additional reduction is welcomed. The influence of DC offsets can be further minimized by choosing the IF in an intelligent way.

Additionally, DC offsets can be superimposed on the code before modulating the IF carrier. An expression for the influence of both possible DC offset effects will be derived here. Again, all equations do account for only one target. The received signal is written as

$$s_{\mathrm{rec,DC}} = \left(|A_1|\, x_{\mathrm{b}}\left(t - z_1 T_{\mathrm{c}}\right) + \mu_{\mathrm{b1}}\right) \cdot \cos\left(\omega_0 t + \vartheta_1\right) + \mu_{\mathrm{i1}} \tag{2.47}$$

with μ_{b1} the DC offset that was superimposed in baseband on the code and μ_{i1} the DC offset superimposed on IF. Analogously the in-phase reference signal is denoted as

$$s_{\mathrm{ref,I,DC}} = \left(|A_0|\, x_{\mathrm{u}}\left(t\right) + \mu_{\mathrm{b0}}\right) \cdot \cos\left(\omega_0 t + \vartheta_0\right) + \mu_{\mathrm{i0}}. \tag{2.48}$$

The following steps are performed for the in-phase only, but are of course analogical for the quadrature component. The correlation of $s_{\mathrm{rec,DC}}$ with $s_{\mathrm{ref,I,DC}}$ yields

$$\begin{aligned}\varphi_{s_{\mathrm{rec,DC}} s_{\mathrm{ref,I,DC}}} = \int_0^{LT_{\mathrm{c}}} &\left(\left(|A_1|\, x_{\mathrm{b}}\left(t - z_1 T_{\mathrm{c}}\right) + \mu_{\mathrm{b1}}\right) \cdot \cos\left(\omega_0 t + \vartheta_1\right) + \mu_{\mathrm{i1}}\right) \cdot \\ &\left(\left(|A_0|\, x_{\mathrm{u}}\left(t + \tau\right) + \mu_{\mathrm{b0}}\right) \cdot \cos\left(\omega_0 t + \vartheta_0\right) + \mu_{\mathrm{i0}}\right) \mathrm{d}t = \\ &= \varphi_{s_{\mathrm{rec}} s_{\mathrm{ref,I}}} + \gamma_{\mathrm{DC1}} + \gamma_{\mathrm{DC2}} + \ldots + \gamma_{\mathrm{DC8}}.\end{aligned} \tag{2.49}$$

Assuming Eq. 2.58 valid, the following terms are zero, due to the integration over a cos-term

$$\gamma_{\mathrm{DC4}} = \mu_{\mathrm{b1}}\mu_{\mathrm{b0}} \int_0^{LT_\mathrm{c}} \cos\left(\omega_0 t + \vartheta_1\right) \cos\left(\omega_0 t + \vartheta_0\right) \mathrm{d}t = 0, \tag{2.50}$$

$$\gamma_{\mathrm{DC5}} = \mu_{\mathrm{b1}}\mu_{\mathrm{i0}} \int_0^{LT_\mathrm{c}} \cos\left(\omega_0 t + \vartheta_1\right) \mathrm{d}t = 0, \tag{2.51}$$

and

$$\gamma_{\mathrm{DC7}} = \mu_{\mathrm{i1}}\mu_{\mathrm{b0}} \int_0^{LT_\mathrm{c}} \cos\left(\omega_0 t + \vartheta_0\right) \mathrm{d}t = 0. \tag{2.52}$$

For a real world system, $|A_1| \ll |A_0|$ and therefore $|A_1| \ll \varphi_{s_\mathrm{rec}s_\mathrm{ref}}$, due to free space attenuation. Therefore, terms with a pre-factor $|A_1|$ can be neglected, i.e.

$$\gamma_{\mathrm{DC1}} = |A_1|\,\mu_{\mathrm{b0}} \int_0^{LT_\mathrm{c}} x_\mathrm{b}\left(t - z_1 T_\mathrm{c}\right) \cos\left(\omega_0 t + \vartheta_1\right) \cos\left(\omega_0 t + \vartheta_0\right) \mathrm{d}t \approx 0 \tag{2.53}$$

and

$$\gamma_{\mathrm{DC2}} = |A_1|\,\mu_{\mathrm{i0}} \int_0^{LT_\mathrm{c}} x_\mathrm{b}\left(t - z_1 T_\mathrm{c}\right) \cos\left(\omega_0 t + \vartheta_1\right) \mathrm{d}t \approx 0. \tag{2.54}$$

The term

$$\gamma_{\mathrm{DC8}} = \mu_{\mathrm{i0}}\mu_{\mathrm{i1}} LT_\mathrm{c} \tag{2.55}$$

can only be minimized by reducing the offset or the code length, i.e. cannot be influenced by any of the remaining degrees of freedom, whereas

$$\gamma_{\mathrm{DC3}} = \mu_{\mathrm{b1}}\,|A_0| \int_0^{LT_\mathrm{c}} x_\mathrm{u}\left(t + \tau\right) \cos\left(\omega_0 t + \vartheta_1\right) \cos\left(\omega_0 t + \vartheta_0\right) \mathrm{d}t \tag{2.56}$$

and

$$\gamma_{\mathrm{DC6}} = \mu_{\mathrm{i1}}\,|A_0| \int_0^{LT_\mathrm{c}} x_\mathrm{u}\left(t + \tau\right) \cos\left(\omega_0 t + \vartheta_0\right) \mathrm{d}t \tag{2.57}$$

can be minimized by choosing x_b instead of x_u.

2.4.3 Influence of the Intermediate Frequency

As already mentioned, this chapter deals with the task of minimizing $\gamma_{\cos}$ and $\gamma_{\sin}$. A first approach towards this aim is trying to exploit the fact that the correlator integrates over a harmonic oscillation. With Eq. 2.35 in mind, the effect of a certain frequency choice is investigated. The following derivation will be made for the in-phase component, but is valid for both the in- and quadrature-phase components. The first prerequisite is made concerning the intermediate frequency. Assuming $x_{\mathrm{b}}\left(t - z_1 T_{\mathrm{c}}\right) \cdot x_{\mathrm{u}}\left(t + \tau\right)$ in $\gamma_{\cos}$ in Eq. 2.30 constant, ω_0 has to fulfill

$$\omega_0 = k \cdot 2\pi \frac{1}{T_{\mathrm{c}}} \ , \ k \in \mathbb{N} \tag{2.58}$$

in order to eliminate $\gamma_{\cos}$ for $z_1 T_{\mathrm{c}} = \tau$. The above made assumption is valid for e.g. rectangular $p(t)$. For this case,

$$\begin{aligned}
\gamma_{\cos}\left(\tau\right) = \frac{\left|A_0\right|\left|A_1\right|}{2} \sum^{N_{\mathrm{HL}}} \Big[\int_a^b \cos\left(2\omega_0 t + \vartheta_0 + \vartheta_1\right) \mathrm{d}t + \\
+ (-1) \cdot \int_b^{a + k \cdot 1/f_0} \cos\left(2\omega_0 t + \vartheta_0 + \vartheta_1\right) \mathrm{d}t \Big] \\
= \frac{\left|A_0\right|\left|A_1\right| N_{\mathrm{HL}}}{4\omega_0} 2 \Big[\sin\left(2\omega_0 b + \vartheta_0 + \vartheta_1\right) - \sin\left(2\omega_0 a + \vartheta_0 + \vartheta_1\right) \Big] = \\
= \frac{\left|A_0\right|\left|A_1\right| N_{\mathrm{HL}}}{\omega_0} \sin\big(\omega_0\left(b - a\right)\big) \cos\big(\omega_0\left(b + a\right) + \vartheta_0 + \vartheta_1\big)
\end{aligned} \tag{2.59}$$

and analogical

$$\gamma_{\sin}\left(\tau\right) = -\frac{\left|A_0\right|\left|A_1\right| N_{\mathrm{HL}}}{\omega_0} \sin\big(\omega_0\left(b - a\right)\big) \sin\big(\omega_0\left(b + a\right) + \vartheta_0 + \vartheta_1\big). \tag{2.60}$$

The limit a results from the delay of the reference signal τ, whereas b is related to the distance of the target $z_1 T_{\mathrm{c}}$, due to the delay of x_{u} and x_{b}, respectively. The integration limits a and b are shown in Fig. 2.19. The number of high-low transitions $N_{\mathrm{HL}} = 2^{l-2}$ is deduced empirically. Figuratively spoken, the integral equals zero, because there is the same number of regions with the coefficient 1 and -1. Continuing Eqs. 2.59 and 2.60 to calculate the absolute of the IQ correlation

$$\gamma_{\cos}^2 + \gamma_{\sin}^2 = \frac{\left|A_0\right|^2 \left|A_1\right|^2 N_{\mathrm{HL}}^2}{\omega_0^2} \sin^2\big(\omega_0\left(z_1 T_{\mathrm{c}} + \tau\right)\big) \tag{2.61}$$

and

$$\begin{aligned}
2 \cdot \varphi_{\cos}\gamma_{\cos} + 2 \cdot \varphi_{\sin}\gamma_{\sin} = -\frac{\left|A_0\right|^2 \left|A_1\right|^2 N_{\mathrm{HL}}}{\omega_0} \varphi_{pp}\left(\tau\right) * \varphi_{m_{\mathrm{b}} m_{\mathrm{u}}}\left(\tau\right) \cdot \\
\sin\big(\omega_0\left(z_1 T_{\mathrm{c}} + \tau\right)\big) \cdot \cos\big(\omega_0\left(z_1 T_{\mathrm{c}} - \tau\right) + 2\vartheta_1\big)
\end{aligned} \tag{2.62}$$

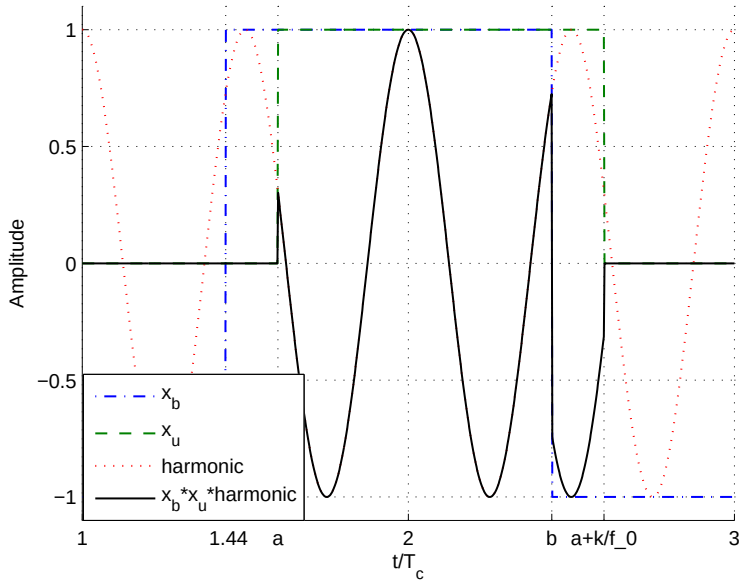

Fig. 2.19: Illustration for integration limits in Eq. 2.59

are obtained in addition to Eq. 2.33. Clearly, $\gamma_{\cos}$ and $\gamma_{\sin}$ decrease with $\frac{N_{\mathrm{HL}}}{\omega_0}$. According to Eq. 2.59, this is valid for rectangular pulses. Eq. 2.62 is zero as soon as the ACF is zero, so the term in Eq. 2.61 needs to be minimized. This can be reached by either setting $\omega_0(z_1 T_\mathrm{c}+\tau) = k\cdot\pi$, with $k \in \mathbb{N}_0$, or by minimizing $\frac{N_{\mathrm{HL}}}{\omega_0}$. The first solution is not feasible, as it would limit $\Delta\tau \geq T_\mathrm{c}$ and is furthermore not applicable for multi-target scenarios. This leaves the minimization of $\frac{N_{\mathrm{HL}}}{\omega_0}$ which can be obtained by either a shorter code, i.e. lower N_{HL}, or a higher IF, i.e. greater ω_0.

As already mentioned, the IF is required to be a multiple of $1/T_\mathrm{c}$. This can either be reached by coupling the IF back to the pulse generator, or by tuning the local oscillator of the received signal down converter. The tuning of the LO could be controlled by a phase locked loop (PLL).

Fig. 2.21 shows the correlation of a received signal with only one target. The parameters are rectangular pulses, $L_\mathrm{c} = 15\,\mathrm{bit}$ m-sequence, and $f_{\mathrm{IF}} = 2\frac{1}{T_\mathrm{c}}$. The influence of the terms $\gamma_{\cos}$ and $\gamma_{\sin}$ is clearly identifiable in the section shown in Fig. 2.21.

2.4.4 Influence of the Pulse Form

In Sec. 2.2.2 and Eq. 2.18 the influence of the pulse form on the shape of a baseband correlation was briefly discussed. The following paragraph will derive an equation for the influence on IF correlations and the relevance of intersymbol interference. The shape of the IF correlation with arbitrary pulse forms can easily be derived by combining Eqs. 2.18, 2.30, and 2.32.

Also the above paragraph promotes the use of sharp, needle-shaped pulses, which is not a generally valid solution. As for all other RF applications, the bandwidth will be

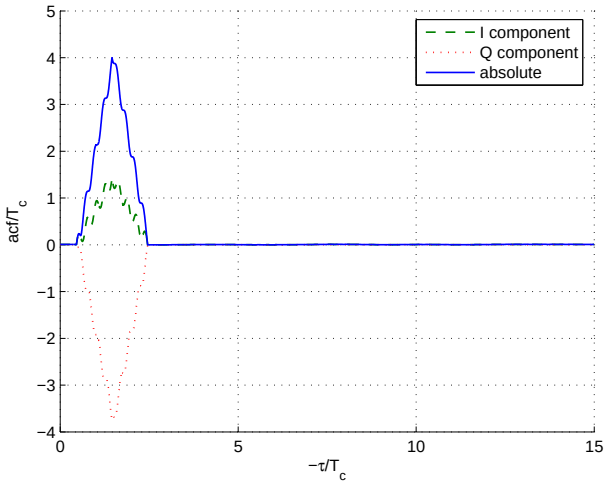

Fig. 2.20: 15 bit m-sequence IQ IF correlation

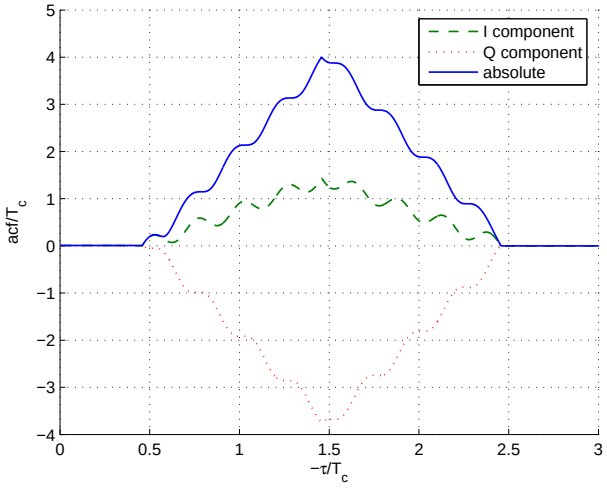

Fig. 2.21: Part of a 15 bit m-sequence IQ IF correlation, clearly visible the γ term

the limiting factor, when choosing a pulse form. In general, when the choice of the pulse form is a degree of freedom in the system under investigation, a pulse that has an optimal pulse-bandwidth factor will be chosen. In real world systems, the technical feasibility and the cost will furthermore play important roles. Not obeying the last two arguments, a Gaussian shaped pulse is decided for. It can be shown [31, 32] that it provides the best pulse-bandwidth product. For practical reasons, further considerations need to be made. Gaussian pulses are neither time-, nor band-limited. The later can be handled, as the bandwidth limitations usually prescribe a power level for out of band emissions that is greater than zero. Pulses with no time limitation cannot be handled in real-world systems, i.e. they will be truncated at some point.

Intersymbol interference in general appears for non time-limited pulses. In information theory, infinite impulse response (IIR) pulses are used without obtaining intersymbol interference. By choosing the proper point in time for sampling the received signal, this can be realized. Assuming $p(t) = \mathrm{si}(t/T)$, si the sinus cardinalis function, the bit duration or time in between the transmission of two subsequent pulses will be $n \cdot T$, with $n \in N$. This ensures that for a sampling rate of $1/(nT)$, all prior pulses are zero, whereas the actual pulse has its peak value. Two problems arise, if this example is transferred to the PN-radar example. First, not the received signal but the ACF of the received signal with a reference is under investigation. This means, the ACF would have to fulfill the above mentioned conditions. Second, in a multi target environment, the distance between two ACF peaks is arbitrary and therefore the time in between two peaks is not constant as in communication systems. So to ensure minimum influence of one target on other target responses, the ACF should fulfill Eq. 2.6 or come as close as possible to this case. The direct influence of the pulse form onto the IF correlation result via its ACF can be seen in Eqs. 2.30 and 2.32.

2.4.5 Influence of the Doppler Shift

Unlike for FMCW radars, where the Doppler effect is used to derive the relative velocity of an object, this is not possible for PN radars without huge efforts in signal processing. Furthermore, since the received signal is not detected, but mixed to an intermediate frequency, the influence of the Doppler shift within the presented system is of great importance. The current IF plays a vital role for the correlation result, as mentioned earlier. The Doppler effect influences the spectrum of a transmitted signal, if the receiver approaches or departs from the transmitter. Furthermore, not only the relative speed of the transmitter against the receiver, but also the original frequency influences the frequency shift. The relativistic expression for the Doppler shift reads as

$$f_{\mathrm{RX,Source}} = f_{\mathrm{TX}} \cdot \sqrt{\frac{1+\frac{v}{c_0}}{1-\frac{v}{c_0}}} \tag{2.63}$$

according to [33], with v the closing speed of between radar source and target, and $f_{\mathrm{RX,Source}}$ the frequency observed by the target. For the received frequency at the receiver

$$f_{\mathrm{RX}} = f_{\mathrm{RX,Source}} \cdot \sqrt{\frac{1+\frac{v}{c_0}}{1-\frac{v}{c_0}}} = f_{\mathrm{TX}} \cdot \frac{1+\frac{v}{c_0}}{1-\frac{v}{c_0}}, \tag{2.64}$$

which results in a Doppler shift of

$$f_{\mathrm{D}} = f_{\mathrm{RX}} - f_{\mathrm{TX}} = f_{\mathrm{TX}} \cdot \frac{\frac{2v}{c_0}}{1-\frac{v}{c_0}}. \tag{2.65}$$

For $v < 0.1 \cdot c_0$ this result can be simplified to

$$f_{\mathrm{D}} = f_{\mathrm{TX}} \cdot \frac{2v}{c_0}. \tag{2.66}$$

Eq. 2.66 is derived very figuratively in [34], by differentiating the phase between transmitter and receiver.

For a scenario where two cars are approaching each other, each one with a velocity of around 100 km/h, the target car has a relative speed of 200 km/h to the radar equipped car. With the resulting $v = 60\,\mathrm{m/s}$, the Doppler shift for a $f_{\mathrm{TX}} = 24\,\mathrm{GHz}$ radar is $f_{\mathrm{D}} \approx 9.6\,\mathrm{kHz}$. Fig. 2.22 shows the spectrum of an m-sequence and the spectrum of the same sequence that was shifted by f_{D} by the Doppler effect. To be precise, the shift is different for any point of the spectrum according to Eq. 2.65, but for narrow bandwidths at high carrier frequencies, the shift is approximately constant for the entire signal. The shift that appears at the RF is directly converted down to IF, i.e. f_{D} is the same at IF. As the entire spectrum of the m-sequence is shifted, the chip duration of the modulated sequence changes slightly, i.e. given a transmitted $T_{\mathrm{c}} = 1\,\mathrm{ns}$, the change in chip duration for the above mentioned example is on the order of 10 fs or 0.01 %. Therefore only minor noise effects will result from the change in chip duration.

If the change in chip duration was a little greater, the Doppler effect and therefore the velocity of the respective object could be determined. Two dimensional correlation would be the direction to investigate into.

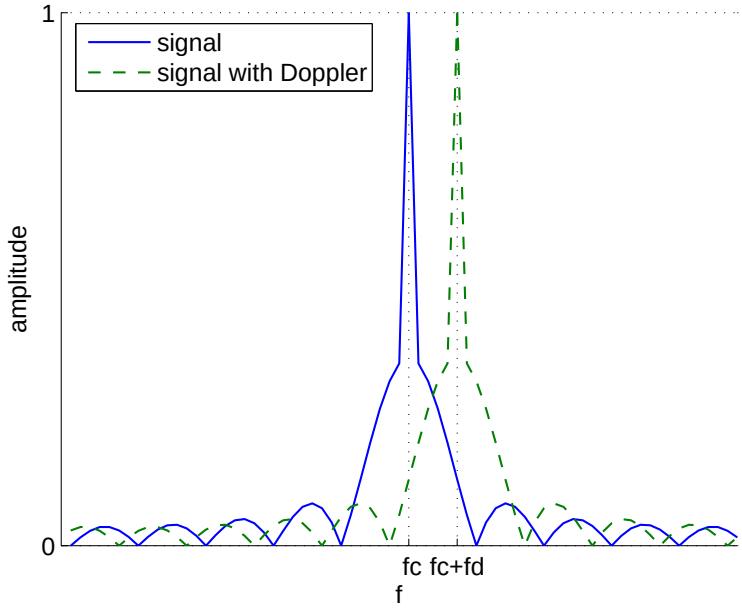

Fig. 2.22: The spectrum of an m-sequence and the same spectrum shifted by the Doppler effect by f_D

2.4.6 Limitations of the IF correlation principle

The above mentioned principle is very powerful and provides substantial advantages over baseband correlators. To gain those, certain boundary conditions need to be satisfied.

One argument to be mentioned here is the IQ correlation. As the received signal is usually extremely weak, it is not a good idea to split it up into two branches for the I- and Q-correlation. As the correlator output is sampled and A/D converted, the correlations can be performed in series, switching the reference input between the I- and Q-reference. The correlator output is stored digitally and the absolute of the IQ-correlation is calculated after each single correlation. As a disadvantage, this method requires the scenario to be constant over two code lengths. According to the received power level, the proper method has to be determined, i.e. whether high speed targets require parallel I/Q-correlation at the cost of further reduced RX power, or if low power levels occur for slow targets that allow serial I/Q-correlation.

2.5 Analog – Digital Conversion

Using the IF correlation principle, a detector for the received signal is not required, as the IF signal is correlated directly. The correlator output on the other hand, contains after a low pass filtering only the DC component. This allows for direct A/D conversion.

2.5.1 ADC Considerations

Sec. 2.2.2 gave already a short overview over the dynamic range. Later on, the dependency of the RCS on the target properties will be treated in detail. Unfortunately, not only the desired dynamic range of the required analog - digital converter (ADC) is enormous, but also the required resolution. The idea therefore is to utilize a logarithmic ADC, i.e. high precision for small amplitudes and a high dynamic range. Fortunately, the sampling rate is moderate, as only a single sample is required for every integration period, i.e. each correlation point. Usually for ADCs, higher resolution means lower sampling rate. For a sampling rate of 10 MHz, ADCs with a resolution of more than 16 bits can be found. Taking the non ideal factors of the ACF into account, it becomes clear that strong targets will always hide those that are smaller by several orders of magnitude in RCS. These non ideal factors include everything from the width of the ACF to the noise resulting from various sources.

Introducing intelligent concepts for A/D conversion, the above mentioned problems of huge targets shading smaller ones can be minimized. Standard linear ADCs have two disadvantages. First, to cover the enormous dynamic range, a high quantization depth is required. This makes the ADC expensive. Furthermore, the quantization steps are relatively large for weak signals and small for strong signals. This led to the idea of utilizing a logarithmic ADC or several linear ADCs with a step-width configured for the specific sector.

Fig. 2.23 shows the quantization steps for an interval 1–1000 that is discretized by 3 bits, i.e. eight values. Clearly, the logarithmic stepping exhibits a big advantage. High resolution for weak targets and lower resolution for strong targets. As already mentioned, a fine resolution for strong targets is only of limited use. Clearly, the quantization noise is reduced, but this is not critical for the imaging algorithm. For the automotive scenario it is more important to be able to separate two targets in close proximity. The argument, that coarse quantization for strong targets makes it impossible to detect a smaller close by target does not count. It has already been mentioned, that the non-ideal pulse form and the limited bandwidth do not allow the separation of signals whose amplitude ratio is greater than a certain value. Two weak targets on the other hand, e.g. a tree next to the road and a child moving onto the road close to the tree, can be separated, as many digital values are available for the corresponding analog value range. Fig. 2.25 shows this impressively. The figure contains the absolute quantization error for a 3 bit ADC of a dynamic range of 60 dB, i.e. a ratio max/min in amplitudes of 1000.

Mentioning numbers for the analog value range and the number of bits required the discussion goes back to the dynamic range ΔP. A dynamic range of 100 dB is desired or requested by many developers of imaging systems. True, the more dynamic range, the better the resulting image. In reality though, ranges on the order of 60 dB are accomplishable with some effort. ADCs with a depth of $b = 12$ bit are commonly available at rational prices. Assuming furthermore the sampling of amplitudes instead of power, as the IF correlator mentioned in Sec. 2.4.1 is used, this leads to a distance of 0.244 amplitude

units in between two digital values according to

$$\Delta A_{\mathrm{q}} = \frac{\sqrt{\Delta P}}{2^b}. \tag{2.67}$$

This leads to the same relative error curve as the one depicted in Fig. 2.25. It is clearly visible that the maximum relative error for logarithmic quantization is less than 50%, whereas linear quantization reaches 100% relative error. In Fig. 2.24 the absolute quantization errors are displayed in contrast to the relative errors in Fig. 2.25.

During the realization of a logarithmic ADC, one may encounter several problems. In case a logarithmic ADC cannot be realized, the option of a partly linear ADC is left over. The entire amplitude range is subdivided into several sub-ranges. For the example in Fig. 2.23, three sub-ranges existed, 1–50, 50–500, and 500–1000. Each one is converted by its own linear ADC. By using different depths of the ADCs or different sizes for the sub-ranges, the overall quantization is non-linear.

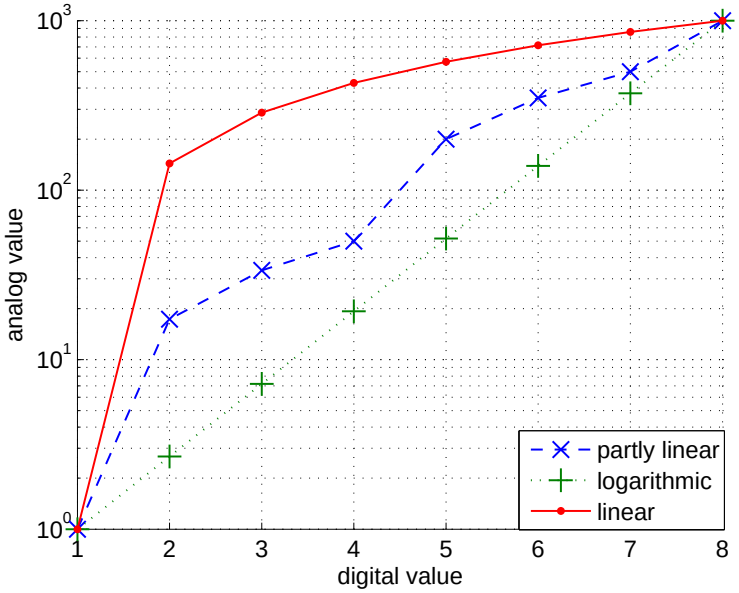

Fig. 2.23: Quantization steps for linear, logarithmic and partly linear 3 bit ADCs

2.5.2 Quantization Noise

Clearly, quantization decreases the SNR. Sec. 2.4.2 referenced this section for details on the quantization noise. The quantization noise can in general be calculated as

$$P_{\mathrm{N,q}} = \int_{-\infty}^{\infty} |x - q(x)|^2 \cdot p(x)\ \mathrm{d}x \tag{2.68}$$

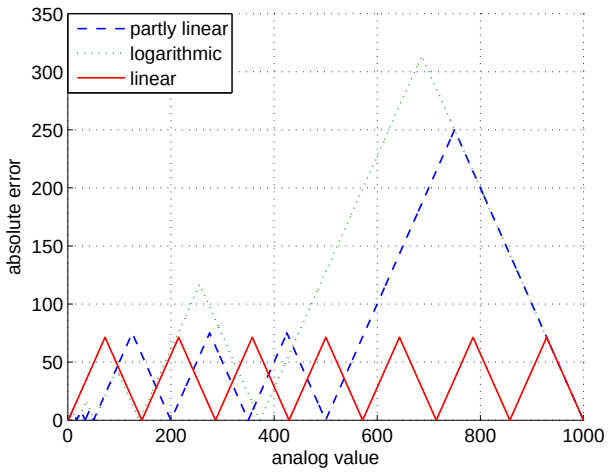

Fig. 2.24: Absolute quantization error for the mentioned 3 bit ADCs

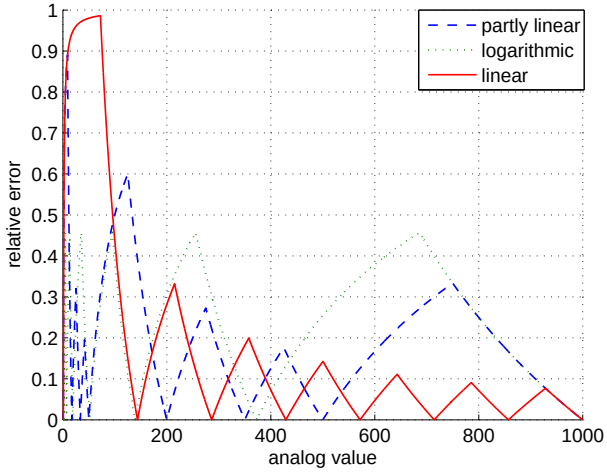

Fig. 2.25: Relative quantization error for the mentioned 3 bit ADCs

with x the signal amplitude, $q(x)$ the quantized signal amplitude, and $p(x)$ the probability of the respective signal amplitude. The signal amplitude x names the quantizer input, i.e. the ACF including noise.

In standard quantization noise calculations, the assumption of equally distributed amplitudes is made, which reduces $p(x)$ to $\frac{1}{A_{\max}}$, with $A_{\max}$ the maximum amplitude. As the reason for choosing a logarithmic quantizer was a signal with scarce but strong peaks, equally distributed amplitudes cannot be assumed here. Eq. 2.45 can be developed into an SNR estimation containing quantization noise by adding Eq. 2.68 to the denominator.

2.6 Processing the A/D-converted signal

The ADC output goes straight into the digital processing unit (PU). Within the PU, any mathematical operation can be applied to the sampled data. Furthermore, the memory of the PU allows random access to all elements of the sampled data. Therefore, it is an easy and cheap choice to implement further mathematical operations on the signal into the PU.

2.6.1 Averaging

As both paths of the correlation, the in- as well as the quadrature-phase component are corrupted by different noise effects, the usage of averaging methods needs to be evaluated. Clearly it is not the mean over the correlation result that is of interest. It is rather the average over multiple samples of entire ACFs that may increase the SNR. Therefore, it becomes clear that the averaging needs to take place in the digital world, i.e. a microprocessor. Furthermore, the process has to be implemented before the absolute of the IQ-correlation is evaluated, as averaging absolutes will increase the noise floor instead of decreasing it. Mathematically, averaging over an infinite number of ACF samples completely cancels out

zero mean noise. The last sentence contains two necessary prerequisites for the success of the method under investigation. It is on the one hand the fact, that only zero mean noise, such as additive white Gaussian noise (AWGN), can be averaged out. Furthermore, ideally an unlimited number of samples are required. Using less samples may reduce noise too. As the number of samples used for the averaging is limited, it has to be evaluated, whether the obtained result is worth the effort.

Most noise types can be assumed zero mean, so averaging promises good results. The other question cannot be answered in general. As noise is random, averaging over only n samples may even increase the noise for one point in time. Assuming that one ACF consists of a large number of sampled values, the overall effect on the ACF is positive even if n is on the order of ten or less. Fig. 2.26 shows an ACF, the same ACF corrupted by noise, and the effect of averaging over ten ACFs.

Averaging multiple samples of the ACF brings up a problem in real time applications such as the automotive radar. The process takes time. Ideally a constant scenario over the averaging time is required, too. As this will not be the case, averaging has to be tested in a real world environment.

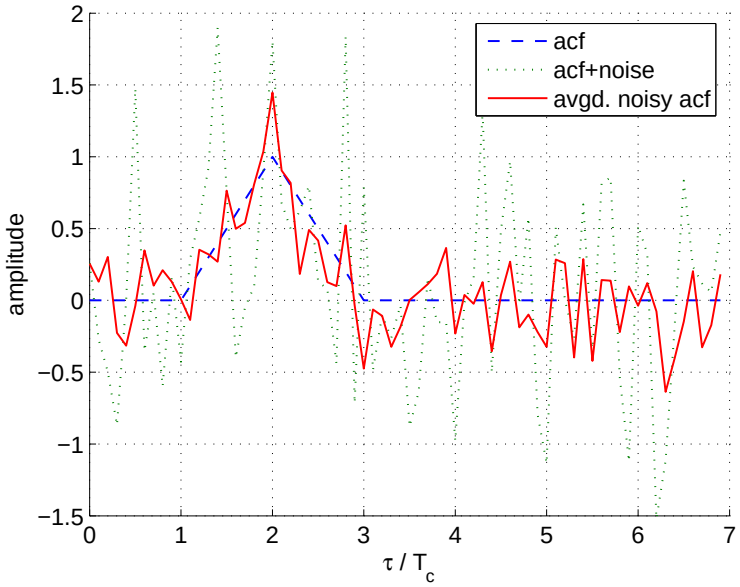

Fig. 2.26: Averaging effect, applied to a digitally stored ACF with superimposed white Gaussian noise

2.6.2 Adding I- and Q-path

In Sec. 2.4.1, Eq. 2.33, the necessity for calculation of the absolute of the IQ-correlation is derived. It is based on the prerequisite that the IF correlation yields the same result as a baseband correlation would do.

2.6.3 Peak Detection

After A/D conversion of the IQ correlator output, lists containing target descriptions, using distance and amplitude need to be generated. A peak detector for this task was at first taken from [35]. The detector in this publication was intended for the use in automated analysis of electrocardiograms. In opposite to standard peak detectors, the detection is not based on the exceedance of a threshold value but on a so called peak excursion δ. In between two peaks, i.e. local maxima, a local minimum is required to exist with a value at least δ less than the lower one of the two maxima. Clearly, for a high peak excursion, this algorithm becomes highly resistant against noise. Unfortunately, at the same moment, small targets are lost. For small peak excursions, strong targets are detected as multiple targets, due to noise affecting the signal slopes of the ACFs. This effect does not only smear the image, but increases the calculation time enormously, as multiple sets of possibly corresponding targets arise, see Sec. 3.4. To improve the dynamic range of the detector system, the phase of the IQ correlation result was also taken into account. This IQ-correlation specific method for peak detection refinement is described in Sec. 4.1.2, as it was part of the realization.

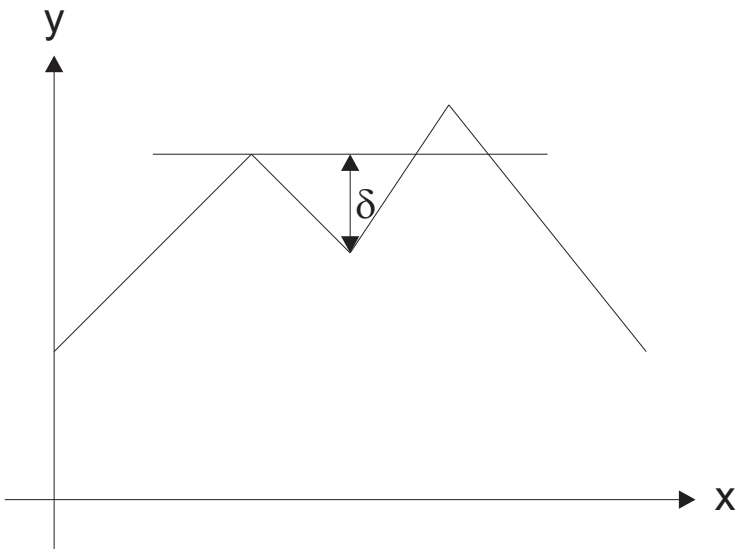

Fig. 2.27: Peak excursion as defined for the peak detection algorithm

3. IMAGING ALGORITHM

Radar stands for radio detection and ranging, where ranging means measuring the radial distance. Often it is not enough to detect a target at a radial distance d. Usually it is of great interest, where the object is located exactly in two or three dimensions. For air traffic controllers, e.g. it is essential to know the altitude of each aircraft to avoid collisions. Acquiring this angle information is generally called imaging. The following sections provide a short overview of common imaging methods, before introducing the algorithm under investigation.

3.1 General Imaging Problems

In general, resolution is the main problem for all imaging applications. Obviously, the higher the resolution, the better the image, as known from optical problems. Lateral resolution, i.e. the range resolution, depends on radar system parameters, whereas transversal resolution, i.e. angular resolution, is always related to the antenna. This relation is either direct for scanning radars or indirect for imaging algorithms. Therefore two different groups of approaches to increase the transversal resolution can be distinguished. On the one hand the real aperture of the antenna can be increased. This yields a sharper beam and therefore a better resolution with basically no signal processing. It is useful for non-static, i.e. scanning antennas. On the other hand, there are methods that require powerful processors. These methods generally make assumptions that are valid only for their specific application. Making intelligent assumptions can help to increase the resolution, as the number of degrees of freedom is reduced. All algorithms require a specific constancy of the scene that will be imaged. Synthetic aperture radars (SAR) for example require a constant scenario over time, as multiple serial measurements are combined into one picture. The algorithm presented here requires constant radar cross section (RCS) of the targets for small changes of the aspect angle. This might sound as an unrealistic assumption, but it will be shown that for small changes in aspect angles, the RCS of many roadside objects does not change significantly (see Sec. 4.2.1).

3.1.1 Cooperative and Non-Cooperative Targets

There are two major classes of targets, cooperative and non-cooperative targets.

Non-Cooperative Targets Non-cooperative targets refer to targets that appear on radar systems solely due to their reflecting properties. These targets are completely de-

scribed by their radar cross section σ. Sec. 4.2.1 treats in detail the possibilities that arise to distinguish and classify these objects. In short, it is extremely difficult and sometimes impossible to distinguish objects, e.g. a small tin can from a child. As they both have a comparable RCS, an imaging algorithm gets a chance to differentiate only if the changes in RCS, due to changing aspect angles, differ during the approach.

Cooperative Targets As cooperative targets are not mentioned further in this document, they will be treated here. A classical example for a cooperative target are aircrafts with a secondary surveillance radar (SSR) transponder. The SSR triggers the transponder to transmit a code that identifies the aircraft. The code consists in the A/C transponder mode of the altitude and call sign of the aircraft. The SSR information is superimposed with the image of the primary radar in order to reduce the identification effort for the airspace surveillance group. This means a primary radar target (reflection) is identified as soon as the secondary radar gets an appropriate answer from the target, i.e. from the same angle and range. The same principle works in roadside environments. To increase road safety, especially for children, passive RFID (radio frequency identification) tags can be introduced. School bags and clothes today are already equipped with optical reflectors to increase the visibility of pedestrians, especially children. The same principle works for radio frequencies. RFID tags or radar reflectors are attached to school bags or other items. The RFID tags are triggered by the imaging radar of an approaching car. They send out an identification code that signals the system that children are close. The method even works if there is no line of sight, e.g. because the children are hidden by parking cars. Ground reflections may help out here. The above mentioned examples of cooperative targets are both active. Passive ones are possible, too. As with the optical reflectors on school bags, radar reflectors can be attached to clothes or school bags of children. Unfortunately, good reflectors for the radar frequencies under investigation are not as small and flexible as the known optical reflectors.

3.1.2 Resolution

Resolution in radar related documents, is generally expressed as a minimum angle or distance, necessary to separate neighboring targets. It depends on radar system parameters, such as chip duration for PN radars. Though it is generally not the limiting factor, the optical resolution limit will be treated in short.

Optical Resolution A target modeled by several scattering centers corresponds to multiple point sources. A point source causes a radiation pattern that is described by the Airy function. The radius of the central disk, also called Airy disk, is on the order of the wavelength of the radiated wave. For the radar context in this document, the radiated wave is of course the reflected wave, i.e. the Airy disk radius depends on the wavelength of the illuminating source.

The Rayleigh criterion is applied to derive the optical resolution, as non coherent sources

are assumed. The decision for the Rayleigh criterion is based on [36], chapter ten. Using the above mentioned criterion means in short that a minimum is required in between the maxima of the radiation patterns of the point sources. Fig. 3.1 depicts the Rayleigh criterion. Clearly, the sum of the intensity of both sources shows a minimum. If the sources were separated only by the 3 dB width of the intensity function, the sum would appear as a single source.

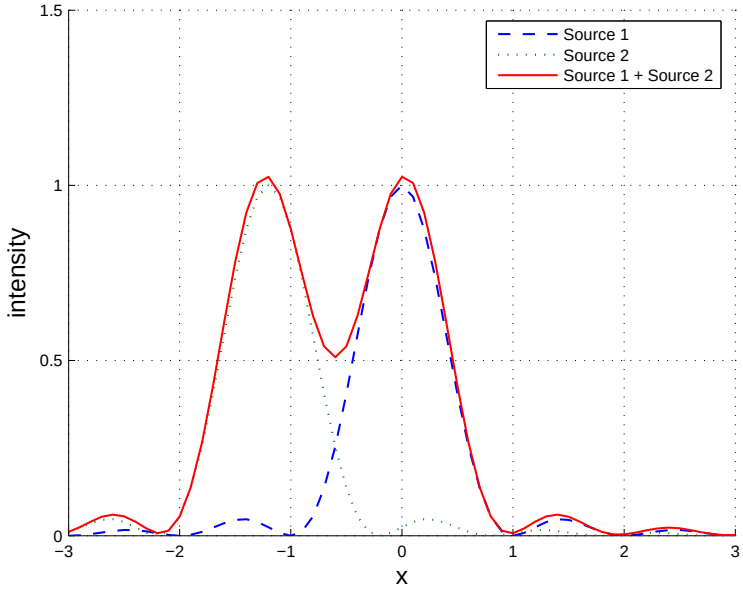

Fig. 3.1: Intensity of two separable point sources, according to Rayleigh criterion

Radar System Resolution Lateral resolution was already mentioned for PN-radars in Sec. 2.2.2. It is a basic characteristic of any radar sensor and describes the ability to separate two targets in radial direction. Range measurement is a basic functionality of any radar system. For precise location of a detected object further information is required, i.e. three measurements are necessary to locate an object in a 3D space. In case of spherical coordinates, the missing values are the azimuth angle φ and the elevation angle ϑ. For applications with the boundary condition that all objects are limited to movements on the ground, i.e. scenarios that do not include flying objects and where heights are not of interest, the problem reduces to two dimensions. As the range is measured in most radar systems by evaluating the time of flight of the wave, most radars provide in general another magnitude that can be evaluated. It is the amplitude of the received signal. Unfortunately it depends on several parameters, notably range d, radar cross section σ, and antenna characteristic G, according to Eq. 3.8. Two of the parameters influencing the amplitude, depend on the remaining azimuth angle, i.e. $\sigma(\varphi)$ and $G(\varphi)$. From this it becomes clear that the angular resolution cannot be calculated analytically, only from the amplitude information. There are ways to exactly derive the position of the detected objects as in Sec. 3.2.4, but they are all limited to scenarios with less targets than sensors available. The algorithm presented

here, tries to make intelligent assumptions, so that only one φ-dependent magnitude is left, which can then be derived.

3.2 Combining Distance Information from Multiple Sensors

This section mentions the most common methods to obtain radar images. Even though the headline might imply multiple physical sensors, this will not be the case for each method. The mechanical scanning radar for example, may consist of a single antenna and only one set of receiver hardware, but as it is revolving, it can be seen as multiple sensors that take pictures in series from different angles.

3.2.1 Mechanical and Electronic Scanning

Both scanning methods are based on the same principle: an antenna with an extremely narrow characteristic sweeps the area of interest. This is equivalent to sampling the scenario with discrete angles.

Mechanical Scanning The classical example for mechanical scanning is the standard naval radar that every vessel utilizes. An antenna with a very sharp beam in its azimuth characteristic rotates around the z-axis at ω_r. Assuming a beam width φ_b of the antenna, a minimum of $2\pi/\varphi_\mathrm{b}$ pictures per revolution need to be taken, to avoid blind spots. Classical display units for this type of radar consist of cathode ray tubes with a persistent display. For the current azimuth angle φ of the antenna, the targets are displayed according to the detected range at the actual angle φ. The persistence time is usually on the order of $2\pi/\omega_\mathrm{r}$, i.e. the time for one revolution. This yields a complete 360° picture, as targets remain on the display until the next sweep. The advantage of a mechanically scanning radar is definitely the cost factor. Besides the mechanics, a single radar sensor with a pencil beam antenna is sufficient. The disadvantages are diverse. First, the scanning frequency is limited, due to mechanical constraints, i.e. the antenna is accelerated all the time. This disadvantage limits the beamwidth in dependency of the transmit carrier frequency, as the antenna size and therefore aperture determines the dimensions of the accelerated part. It is furthermore limited, for the case of monostatic radars. If the same antenna transmits and receives, the antenna position must not change noticeable during the time of flight of the signal. This constraint can be avoided using a bistatic radar, where either the transmit or the receive antenna is isotropic, or covers at least the entire space of interest. In the context of automotive radar, mechanical scanning is not an alternative as it is space consuming and would have to vanish behind the car body, due to design aspects.

Electronic Scanning Electronic scanning is implemented using phased array antennas. Phased array antennas consist of multiple antenna elements that can be fed with a definite

phase. Controlling the phase of each single element allows the steering of the characteristic of the complete structure G, according to

$$G(\vartheta,\varphi) = M(\vartheta,\varphi) \cdot F(\vartheta,\varphi) \tag{3.1}$$

with F the characteristic of a single element and

$$M(\vartheta,\varphi) = \sum_j A_j \cdot \exp\left(-j\left(k\left(r_j - r_0\right) + \varphi_j\right)\right) \tag{3.2}$$

a term that takes care of the feeding phase and the location of the respective element. A_j rates the feed power and φ_j the feed phase for each single element. The term $k\left(r_j - r_0\right)$ accounts for the spatial diversity of the single elements. Controlling the phase of each element describes the phased array transmit antenna. The principle works for receive antennas as well. In this case, the constructive or respectively destructive interference takes place on the feed lines instead of the radiation space. By varying the phase relation between the single elements, the antenna characteristic changes, i.e. the beam can be controlled in its direction. [37] and [20] go further into detail on this topic. This is valid for arrays, consisting of equal single elements. Fig. 3.2 shows a schematic phased array.

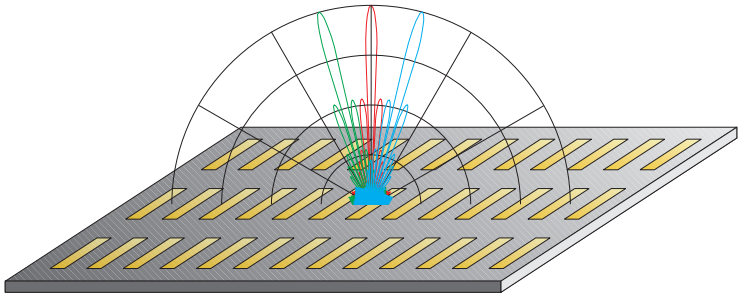

Fig. 3.2: Phased array system, consisting of slot antennas, feed lines are not depicted

It is made up by 13×3 slot antennas. In general, the more single elements are aligned in one direction, the more the overall characteristic is confined in this direction, i.e. the sharper the beam becomes. Phased array antennas are often used in military applications, as they are extremely expensive. This results from expensive microwave devices, necessary to control the feed lines, i.e. provide a definite but variable phase. Furthermore, the control circuits are required for each single element, i.e. a large number of times, which multiplies with the cost of a single element. On the other hand, the maximum angle scan rate is much higher than for mechanical systems, as no mass is accelerated.

3.2.2 Superresolution

Superresolution (SR) is a term that is generally used for techniques that combine multiple low resolution images into a high resolution image. Algorithms are to be differentiated into frequency- and spatial-domain algorithms. Though, the term superresolution is in general

used for algorithms that enhance the resolution of a digital image, it is sometimes used only for algorithms that break the diffraction limit. Here it will be used for any algorithm that increases the resolution, given by the spatial sampling rate. The algorithms require in general the knowledge of the antenna characteristics, so that multiple images can be combined.

For non diffraction limited low resolution images, i.e. images sampled non obeying the Nyquist criterion, the information to be gained by the SR algorithm is hidden by the aliasing effect. Combining several aliased pictures by a powerful superresolution algorithm increases the resolution and may even avoid aliasing effects. Most algorithms require the knowledge of the antenna characteristics and furthermore coherent images. Coherent images for multiple sensors includes the knowledge of the position of the sensors as well as the phase difference resulting from different propagation delays in different sensors. These algorithms are usually spatial domain ones. Images, with a resolution bounded by the diffraction limit, can also be enhanced. The diffraction limit is on the order of the wavelength of the source that illuminates the scenario. It is the well known criterion as familiar in the context of optical images. For analog processing, the resolution of any image is limited by half the wavelength, i.e. $\lambda/2$, of the radiation used for observation. Algorithms that break the diffraction limit, are based on the assumption, that every object can be described by an analytic function in the (spatial) frequency domain. The sampled picture is transformed into the frequency domain, using Fourier transformation. Due to limited resolution, i.e. sampling rate, the spectrum will be limited. Within the limited bandwidth, the algorithm identifies analytical functions and continues them outside the band. After transformation back into the spatial domain, this yields a higher resolution than the original image had. Frequency domain algorithms are generally fast and robust, but limited in dynamic range [38].

Spatial domain algorithms, such as the subspace eigenanalysis algorithms MUSIC [8] and ESPRIT [9] usually require high computational effort and deliver acceptable results only for a few targets. [9] states the condition of less targets than receivers. Under this condition the entire problem of finding corresponding pairs of measurements, as described in Sec. 3.2.4 vanishes.

Superresolution is not only used for radar frequencies but also for optical frequencies as in [17].

3.2.3 Synthetic Aperture Radar (SAR)

Though it may be considered a topic on its own, SAR is not entirely at the wrong place here. It is another form of applying superresolution methods. The difference compared to the above mentioned is that multiple images are taken coherently from different locations. A coherent radar with a small aperture antenna takes multiple pictures while moving along a known path. With the path and velocity known as well as the coherent radar responses from the different locations, the SAR algorithm combines these low resolution pictures into a high resolution image. The low resolution is based on the small real aperture. The high resolution image is equivalent to an image that can be obtained using a radar with an

aperture that corresponds to the path length. This fact is reflected in the nomenclature of the method.

3.2.4 Triangulation and Trilateration

Both, triangulation and trilateration refer to a 3D problem. They both assume 3 references, whose positions are either known exactly for absolute positioning, or are references for relative positioning.

Triangulation

A classical example is nautical navigation, although it is a 2D problem, as the ship is located at sea level. So for the calculation of his position, the ship's captain needs two known reference points, e.g. two lighthouses. By measuring the bearing of each lighthouse, he is able to draw the bearing line into a map, i.e. a line from the respective reference pointing into the direction $bearing + 180°$. The intersection of both lines is the current position of the vessel. Clearly, the ship is required to remain at one position for both measurements to obtain an exact result. This example describes the 2D case of triangulation as illustrated in Fig. 3.3 with a ship and two lighthouses LH_1 and LH_2. In an analogous manner, the 3D case

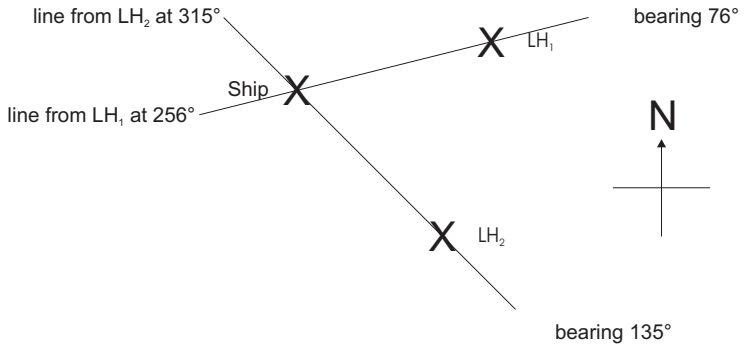

Fig. 3.3: Illustration 2D triangulation principle of a ship using two lighthouses as references

or real triangulation is performed. Three known references help to determine one's position by combining the information of three sequential angle measurements. For the imaging case, the above mentioned example reads as follows. An observer knows the position of the two lighthouses. He takes the bearing from each one towards the ship and combines the information to obtain the position of the target, i.e. ship. This example clearly exposes two main problems attached to the triangulation and trilateration methods. First, it is obvious that the target needs to remain in the same position, during both measurements. Figuratively, a single person is not able to carry out the measurement for this example. Second, if there were N equally looking ships, the observer takes N bearings on every lighthouse, but he would be confused when asked to combine the corresponding pairs, as every target looks the same. This problem will be treated in detail in Sec. 3.3.

Trilateration

Trilateration is based on the same principal, with the difference that distances instead of angles are measured. To approach the system under investigation, a radar system will be referred to here. Again the example is restricted to two dimensions, to keep it figurative. The 3D case is analogous to the case above. Assuming a radar system with two sensors and a single target, the situation depicts as shown in Fig. 3.4. Each sensor measures the distance to the target object separately. For the given 2D case, the result, i.e. the set of possible target locations for one sensor, is a circle around the sensor, with a radius given by the measured distance. As in an automotive scenario the view will be limited to a half-plane, i.e. the sensors will have an azimuth observation angle of 180° or less, so that the circles can be drawn as semicircles. Combining both semicircles yields a single point for the ideal case, i.e. infinite precision. Mathematically, the intersection point described

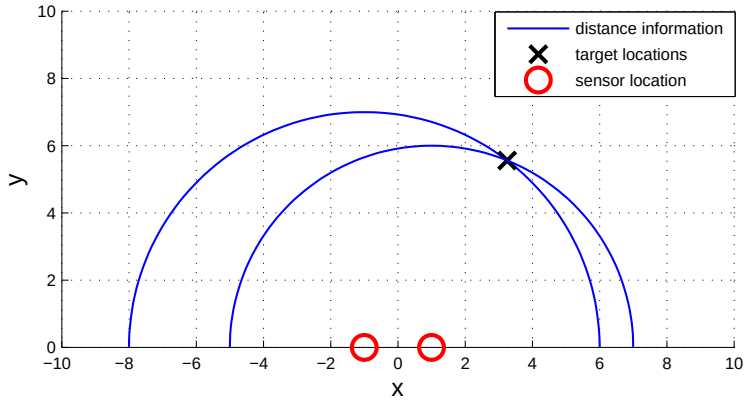

Fig. 3.4: Illustration of the 2D trilateration principle

by vector $\mathbf{x}_\mathrm{I}$ can be expressed as

$$\begin{aligned}\{\mathbf{x}_\mathrm{I}\} = &\left\{\mathbf{x}\,\middle|\, ||\mathbf{x}-\mathbf{s}_1||_2 \geq d_{1,n} - \delta_\mathrm{P} \wedge ||\mathbf{x}-\mathbf{s}_1||_2 \leq d_{1,n} + \delta_\mathrm{P}\right\} \cap \\ &\ldots \quad \cap \\ &\left\{\mathbf{x}\,\middle|\, ||\mathbf{x}-\mathbf{s}_S||_2 \geq d_{S,n} - \delta_\mathrm{P} \wedge ||\mathbf{x}-\mathbf{s}_S||_2 \leq d_{S,n} + \delta_\mathrm{P}\right\}\end{aligned} \tag{3.3}$$

with n indicating the respective target. $\mathbf{s}_m$ is the sensor location vector m, $m = 1 \ldots S$. From this given ideal case, three problems that arise for real world systems will be introduced here.

Precision of the Distance Information First the problem of finite precision of the distance information will be treated. For a PN radar, the precision is given in Eq. 2.19. Clearly, for finite precision, the circles in Fig. 3.4 degenerate to annuli. The result is an intersection area instead of an intersection point. Within this area the target may be located at any point. The size of this area depends on the distance between the sensors

and the precision δ_P. An estimation of the size of the ambiguous area A_amb for the worst case scenario in case the sensor distance $d \geq a$, with a the target distance is derived as

$$A_\mathrm{amb} \leq \Delta\delta_\mathrm{P}^2 + d \cdot \delta_\mathrm{P}. \tag{3.4}$$

It can be derived from the scenario depicted in Fig. 3.5. With the radius $a = \frac{d+\delta_\mathrm{P}}{2}$ for this special case, Eq. 3.4 can be derived as an upper limit by calculating the area of the rectangle R_approx. For the case $d < a$, the worst case is the collocation of both sensors at

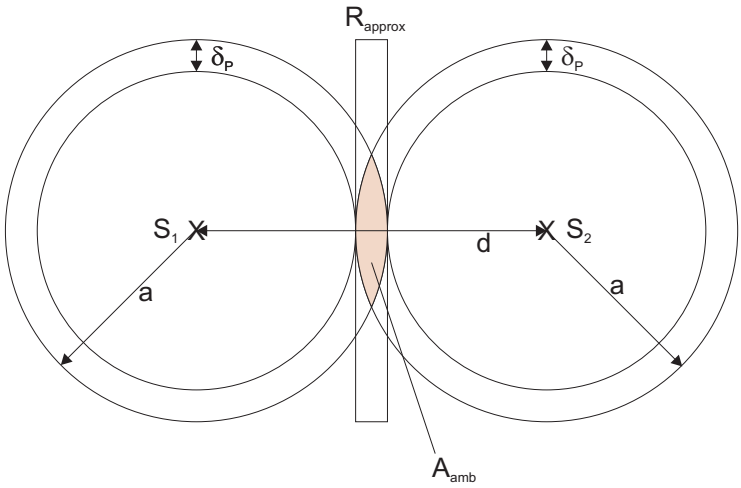

Fig. 3.5: Derivation of the estimation for the ambiguous area for precision δ_P

one place. This yields a maximum ambiguous area of

$$A_\mathrm{amb} \leq \pi \cdot \left(2a\delta_\mathrm{P} - \delta_\mathrm{P}^2\right). \tag{3.5}$$

In general, the ambiguous area A_amb taking the distance precision δ_P into account can be described by

$$A_{\mathrm{amb},i} = \left\{\mathbf{x} \middle| \, ||\mathbf{x} - \mathbf{s}_m||_2 \geq d_{m,i} - \delta_\mathrm{P} \wedge ||\mathbf{x} - \mathbf{s}_m||_2 \leq d_{m,i} + \delta_\mathrm{P}\right\}. \tag{3.6}$$

$\mathbf{x}$ are the position vectors that make up A_amb and $\mathbf{s}_m$ the sensor location vector.

Finding Corresponding Pairs of Measurements As already mentioned in the triangulation paragraph, identifying corresponding sets of target responses is an extremely difficult task. A target appears as one or multiple scattering centers for a radar, depending on its geometry and dimensions. The response of this scattering center with an RCS of σ, causes a peak in the ACF of the PN radar proportional to σ. The aspect angle influences the response in a couple of ways. First, the RCS of an object changes with the aspect angle, but this influence is neglected here, as will be explained in Sec. 4.2.1. Second, the aspect angle influences the response via the angle dependent gain of the TX and RX antennas. This property will later be used to localize targets. It is obvious that two targets

with distances of 5 m and 7 m from sensor 1 and 6 m and 8 m from sensor 2 respectively, lead to the scenario depicted in Fig. 3.6. The figure consists of the two sensors at (−1,0) and (1,0), and the circles with the radii mentioned before. This configuration yields three intersections of the circles, which are marked by black "X"s. Under the assumption that the ACF peaks show roughly the same amplitude, all intersection points are possible target locations. Without further signal processing, i.e. an imaging algorithm, the problem cannot be solved. Obviously, this problem increases exponentially with the number of targets

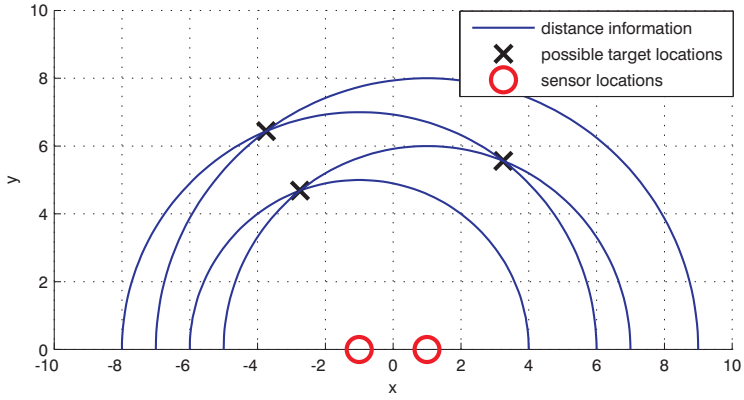

Fig. 3.6: 2D trilateration with two targets and three possible target locations

in the so called unambiguous area. This area is defined by the inter-sensor distance, the aspect angle, and the range precision of the radar. A figurative case will be described to explain the dependencies. The 2D case with two sensors with a distance d in between them is assumed. The field of view (FoV) be 180° , i.e. a half-plane, bordered by the line in between the sensors. Target T_3 in Fig. 3.7 has an aspect angle of -90° , i.e. is on the connecting line of the two sensors. Sensor S_2 detects the target at a distance $d_{23} \pm \delta_P$, whereas sensor S_1 measures a distance of $d_{13} = d_{23} + d_0 \pm \delta_P$. This example shows that with a given d_{23}, any object detected by S_1 within a range

$$d_{23} - d_0 - \delta_P \leq d_{13} \leq d_{23} + d_0 + \delta_P \tag{3.7}$$

needs to be taken into account, as it could be the corresponding target response. For the case that the FoV of the system is limited to less than a half plane, the inter-sensor distance influence decreases, as can be seen in Fig. 3.7 for targets T_1 and T_2. Furthermore, the influence of the range precision is derived. Eq. 3.7 makes clear that the range precision needs to be taken into account multiplied with a factor 2. These considerations indicate that all objects within an area A_{13} have to be checked whether they belong to target T_3, detected by S_2. The area A_{13} denoted with the indices "1" and "3" for correspondence to target "3" in the object list of sensor "1", is described by the range given in Eq. 3.7 and the FoV of sensor S_1. This yields a segment of an annulus that depends on the above mentioned parameters, range precision, sensor distance, and aspect angle, respectively FoV of the sensor. Clearly, this problem arises for all locating algorithms that combine the information of several non-cooperative targets.

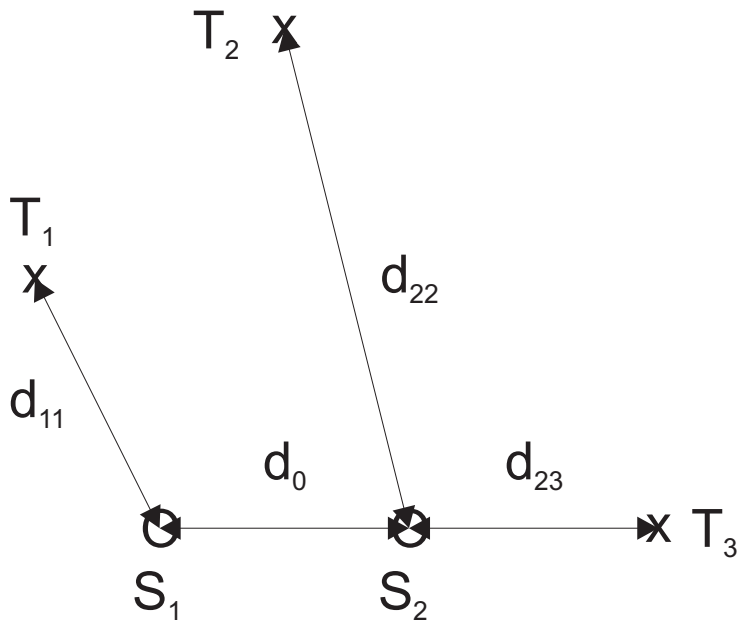

Fig. 3.7: Scenario as used in Eq. 3.7, explaining the assignment problem

Constant scenario As already mentioned in the triangulation scenario, it is important that the scenario is constant during the measurements intended to be combined. For this special case, i.e. a PN-radar with I- and Q-correlation, several boundary conditions apply. Assuming m-sequences of length L, a chip duration of T_c, a serial I-,Q-correlation, and an analog correlation, a constant scenario over a time of $T_\mathrm{cs} = 2L^2T_\mathrm{c}$ is required. The correlation time $T_\mathrm{corr} = L^2T_\mathrm{c}$ results from the analog correlation, under the assumption that the ACF is performed in steps of $\Delta\tau = T_\mathrm{c}$ over the full code length. With $T_\mathrm{c} = 2\,\mathrm{ns}$, $L = 1023\,\mathrm{bit}$ this yields a $T_\mathrm{cs} \approx 4.2\,\mathrm{ms}$. As the code length cannot be reduced without shortening the unambiguous range, see Sec. 2.2.2, another method to minimize the correlation time and therefore the requirements for a constant scenario is proposed in Sec. 4.1.1.

3.3 Amplitude information

Every radar sensor is basically able to evaluate not only the range but also the amplitude of the received signal. The power P_RX of the received signal can be directly derived from the radar equation

$$P_\mathrm{RX} = P_\mathrm{TX} G_\mathrm{TX} \frac{\lambda}{4\pi} \frac{1}{d_\mathrm{TX}^2} \frac{\sigma}{4\pi} \frac{1}{d_\mathrm{RX}^2} G_\mathrm{RX} \frac{\lambda}{4\pi}. \tag{3.8}$$

Eq. 3.8 describes the amount of power received by the antenna. Given the described PN radar system, the amplitude at the correlator output can be given as

$$A_\mathrm{out} = \sqrt{P_\mathrm{RX} \cdot S} \tag{3.9}$$

where S contains all system parameters, such as amplifier gain, attenuation, and resistors. This parameter is assumed constant for all targets. So the dependence of the amplitude on the RCS σ and the transmit and receive antenna gain, G_{TX} and G_{RX}, respectively, is obvious. To go back to the airspace surveillance example, with the mechanically scanned antenna, this information can almost directly be used to indicate the size of the target. Given a quasi-monostatic system, the factor $d_{\mathrm{TX}}^2 d_{\mathrm{RX}}^2$ simplifies to d^4. As R is known from the range measurement, Eq. 3.8 can be solved for the received power and hence amplitude. As the range-corrected amplitude is proportional to the RCS, this value determines the size of the dot on the display. This direct conversion of the received power into RCS information is only valid for pencil beam antennas, i.e. antennas with a very narrow beamwidth. This means, they have a very high gain into one direction and are quasi-blind in every other direction. In case antennas with broader beamwidth are used, as proposed in Sec. 2.3.1, this method cannot be used anymore. Several dB of difference in gain can occur between angle differences of 20° . This means an object with the same RCS can occur more than 10 times bigger, when within the main lobe of an antenna, compared to an out of the main lobe angle.

For the range resolution resulting from a chip duration of $T_{\mathrm{c}} = 1\,\mathrm{ns}$, i.e. $\delta_{\mathrm{d}} = 15\,\mathrm{cm}$, it is sufficient to know the characteristics to a resolution of 1° . This yields a transversal resolution of 15 cm in a distance of $d \approx 10\,\mathrm{m}$ for objects at $\varphi = 89°$. The transversal distance depends on the azimuth angle φ as in

$$d_{\mathrm{T}} = d\cos(\varphi). \tag{3.10}$$

From Eq. 3.10, the transversal resolution derives as

$$\delta d_{\mathrm{T}} = d\cos(\varphi) - d\cos(\varphi + \delta\varphi) = d\frac{\Delta\cos(\varphi)}{\Delta\varphi}\Delta\varphi \rightarrow d\Delta\varphi\frac{\partial\cos(\varphi)}{\partial\varphi} = -d\Delta\varphi\sin(\varphi). \tag{3.11}$$

In contrast to neglecting the antenna gain, the presented approach is based on the knowledge of the characteristics and exploits them.

3.4 Concept

The idea for the imaging algorithm is now to combine trilateration as described in Sec. 3.2.4 and the angular information obtained through the angle dependence of the received amplitude as derived in Sec. 3.3. Parts of this concept are mentioned in [39].

3.4.1 Basic Idea

After constructing all sets of possibly corresponding targets as in Sec. 3.5, the target area A_{amb} is calculated by trilateration techniques. Within this area, the RCS, that would lead to the amplitude response of the current set, is calculated for each point and each sensor. Assuming that most objects in a roadside scenario will show constant RCS over the small

change in aspect angle, resulting from the different sensors, the final decision for one point within the area is made upon the equality of the calculated RCS. To determine the equality of the RCS, the mean over the different sensor results for each point is determined. The criterion for the decision is the sum over the deviation from the sensor RCS of mean RCS.

3.4.2 Discretized Algorithm

The first step remains the trilateration. As mentioned above, this yields an area of a specific size A_{amb} for each set of range-amplitude information. Refer to Fig. 3.5 in Sec. 3.2.4 for A_{amb}. Each set consists of a range value and the corresponding amplitude information from each sensor. Tab. 3.1 is an example for three sensors, and a scenario with one target, visible for all sensors, and another target that is visible for only two sensors. "Visible for a certain sensor" is used to describe the case, wherein the peak detector finds a peak in the correlation that results from the respective target response. Given a sensor spacing of half

Sensor 1		Sensor 2		Sensor 3	
d	A	d	A	d	A
4.2	1.3	4.1	1.7	3.8	1.5
6.4	4.3	6.5	3.3		

Tab. 3.1: Table of sensor responses for a three sensor scenario, with one target visible for all sensors and one target visible to only two sensors

a meter, i.e. they are aligned on the car bumper with 50 cm in between two sensors, the values in Tab. 3.1 result in two sets, i.e. target 1 of sensor 1 cannot correspond to target 2 of sensor 2, because the range difference is greater than the inter-sensor distance. Sec. 3.5 treats this problem in detail. The following section steps through the proposed algorithm using the above mentioned example.

Therefore, the entire two dimensional field of view is discretized into $N_x \times N_y$ boxes, with $N_x, N_y \in \mathbb{N}$. A matrix $\mathbf{M} \in \mathbb{R}^{N_x \times N_y}$ now represents the entire FoV. $\mathbf{M}$ is created for each sensor, so $\mathbf{M}_s$ corresponds to sensor s. All matrix elements are initialized to zero. A_{amb} is then indicated within $\mathbf{M}$ by setting all elements that correspond to A_{amb} to one. The elements corresponding to A_{amb} must satisfy the following mathematical expression:

$$d_s - \delta_{\text{P}} - \sqrt{\frac{D_x^2}{4} + \frac{D_x^2}{4}} \leq \left\| \begin{pmatrix} (n_x - 0.5)\, D_x - S_{x,s} \\ (n_y - 0.5)\, D_y - S_{y,s} \end{pmatrix} \right\|_2 < d_s + \delta_{\text{P}} + \sqrt{\frac{D_x^2}{4} + \frac{D_x^2}{4}} \tag{3.12}$$

with D_x and D_y the discretization step-width in x- and y-direction, respectively, δ_{P} the precision, and d_s the respective sensor distance information. Therefore, the distances in x- and y-direction between the transmitter - receiver and the target, can be written as $d_x = (n_x - 0.5)\, D_x$ and $d_y = (n_y - 0.5)\, D_y$, whereas ($S_{x,s}$,$S_{y,s}$) is the location of sensor s. The terms $(n_x - 0.5)\, D_x$ and $(n_y - 0.5)\, D_y$ reference the center of each element. For sensors at (-0.5,0),(0,0) and (0.5,0) Fig. 3.8 shows the sum of the three sensor matrices

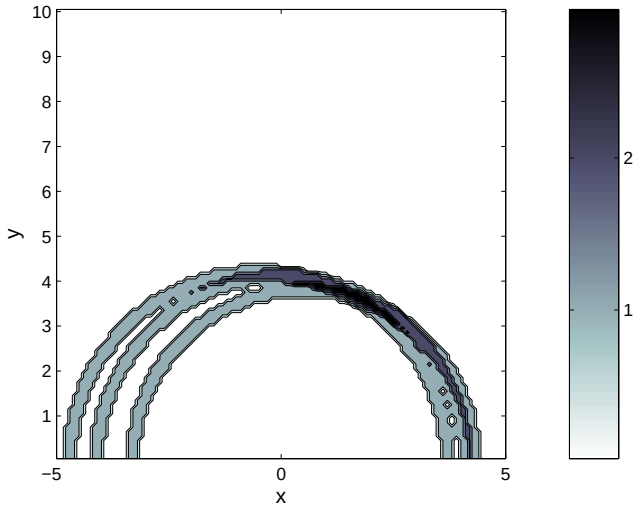

Fig. 3.8: Target area resulting from trilateration

$\mathbf{M}_s$, i.e. the dark area corresponds to the area A_{amb} that can be obtained by trilateration only. The used parameters were target number one from Tab. 3.1, a precision $\delta_{\text{P}} = 0.1$, and the above mentioned sensor locations. The field of view of 10×10 was discretized into 100×100 elements. After elements, whose indices n_x and n_y match the condition in Eq. 3.12, are set to one, Eq. 3.8 is applied bottom-up to these elements. This means, based on the amplitude, given by each sensor, the RCS is calculated by the following equation

$$\sigma_{s,n_x,n_y} = \frac{A_{\text{out},s}^2}{S \cdot P_{\text{TX}} \cdot G_{\text{Rx},s}\left(\varphi_s\right) G_{\text{TX},s}\left(\varphi_s\right)} \cdot \frac{\left(4\pi\right)^3}{\lambda^2} \cdot \left[\left(\left(n_{x,s} - 0.5\right) D_x\right)^2 + \left(\left(n_{y,s} - 0.5\right) D_y\right)^2\right]^2 \tag{3.13}$$

which can be directly derived from Eqs. 3.8 and 3.9. The azimuth angle, necessary to obtain the gain for the current element of the discretized FoV, is obtained using

$$\varphi_s = \arctan\left(\frac{d_{y,s}}{d_{x,s}}\right) + \varphi_{0,s} \tag{3.14}$$

with φ_0 an offset to match the specific alignment of each antenna. With φ_s all necessary variables that appear in Eq. 3.13 are known. To reduce the computational effort the RCS is only calculated for matrix elements that are within the area A_{amb}. Therefore the mask matrix

$$\mathbf{M} = \sum_{s=1}^{S} \mathbf{M}_s' \tag{3.15}$$

is introduced. Given the case that a real target is visible for all sensors, the maximum value in $\mathbf{M}$ equals the number of sensors S. In case a target is not visible for all sensors, the maximum value is reduced by the number of blind sensors for this target. For all matrix

elements that contain max($\mathbf{M}$), the RCS is now calculated for each sensor and stored at the respective position in $\mathbf{M}_s \in \mathbb{R}^{N_x \times N_y}$. At this point, three matrices that contain RCS are existent. Having these matrices, a powerful criterion must now be found to choose the target location within this area A_{amb}.

A criterion to choose the final location

The criterion was set to be the point, where the RCS of three sensors resemble most. The decision is based on the assumption that for the small changes in aspect angle that are treated here, most roadside objects appear with a very similar RCS for all sensors. The assumption is not only based on the small change in aspect angle, but also on the shape of many objects in roadside scenarios. Many of those shapes resemble cylinders, e.g. legs of humans, trees, even human bodies have a curvature at the front and back sides, so can be modeled as parts of a cylinder. For target objects whose RCS changes dramatically, the above mentioned assumption may still apply. A car for example that is right in front of the radar system can be assumed symmetric to its longitudinal axis, which means that two of the equally spaced sensors observe the object under the same absolute of the azimuth angle, i.e. $|\varphi_1| = |\varphi_3|$. If this assumption is adequate for a specific situation, it reduces the difference in aspect angles by a factor of two. In addition, even if for one sensor the RCS deviates heavily from the other ones, it might still be possible to locate the object. Given a three sensor system, one blind or quasi-blind, i.e. the observed RCS differs heavily from that observed by other sensors, can be compensated. Therefore, the respective sensor needs to be identified. In case the sensor did not detect anything, i.e. it is blind, this is trivial. The other case is demanding. The realization of detecting a quasi-blind sensor is explained in Sec. 3.5. Quasi-blind might be a misleading adjective at first, but for the imaging system, a sensor that does not fit into the overall concept is useless for the system and therefore labeled quasi-blind. Listing these arguments, it seems reasonable to assume the RCS observed by the different sensors equal.

The next problem arising is that the correct RCS is not known. In the ideal case, given by non aspect dependent RCS and unlimited precision, this is not a problem, because there will be an element that contains the same value in all matrices $\mathbf{M}_s$. This is the element that corresponds to the true target location. In reality though, this will not be the case. Therefore, a method has to be found, that compares the calculated RCS and return a value that expresses the equality of the calculated RCS. Based on this figure of merit J, the decision for the final target position will be taken. The first step in calculating J is to substitute the missing real RCS by an applicable value. Due to a lack of other possibilities, the mean of the calculated RCS of all sensors is taken and stored in a matrix.

$$\tilde{\mathbf{M}} = \langle \mathbf{M}_s \rangle = \frac{1}{S} \sum_{i=1}^{S} \mathbf{M_s} \tag{3.16}$$

With the result from Eq. 3.16, the value J is calculated for each element of the FoV matrix

so that a $\mathbf{J}$ matrix is obtained as

$$\mathbf{J} = \sum_{i=1}^{S} \left| \mathbf{M}_s - \tilde{\mathbf{M}} \right| \tag{3.17}$$

The minimum of the resulting matrix $\mathbf{\Delta}$ can now be found at a position that corresponds to the true target location. To avoid spikes, i.e. in this case singular points where J is small, the decision taking algorithm requires several comparably small J values in the immediate proximity of the minimum element of $\mathbf{J}$. This requirement was set up as within the area A_{amb} the deviation value J is supposed to be on the same order of magnitude. Sec. 3.5 will use the deviation measure J again to evaluate the significance of the respective target.

3.5 Finding corresponding pairs

It was mentioned earlier that one of the most critical points in radar imaging is combining the corresponding responses of a single target from multiple sensors. Identifying active targets is usually not a big deal, as their response is characterized by a specific signature, e.g. it answers in a specific way, once it is triggered by a radar. In case passive targets have to be imaged, as is the case in automotive radar imaging, usually some boundary conditions apply, but other than that, all possible combinations of all responses have to be checked for validity. The following sections will go through the pair finding and evaluation algorithms using an example. It assumes three sensors at locations $\mathbf{s}_1 = (-0.5\ 0\ 0)^{\text{T}}$, $\mathbf{s}_2 = (0\ 0\ 0)^{\text{T}}$ and $\mathbf{s}_3 = (0.5\ 0\ 0)^{\text{T}}$. The sensors use 255 bit m-sequences with a chip duration of $T_{\text{c}} = 2\,\text{ns}$. The detector limit is set to 10^{-3}. Four targets are given, located at $\mathbf{t}_1 = (-0.4\ 2.9\ 0)^{\text{T}}$, $\mathbf{t}_2 = (2.08\ 6\ 0)^{\text{T}}$, $\mathbf{t}_3 = (1\ 6.5\ 0)^{\text{T}}$ and $\mathbf{t}_4 = (4.5\ 10\ 0)^{\text{T}}$, with amplitudes 1.5, 3, 5 and 2, respectively.

3.5.1 Creating the List of Possibly Corresponding Pairs

For the system under investigation, the above mentioned boundary conditions that apply are that two responses of two sensors cannot correspond, if the difference in the detected distances is greater than the distance between the sensor location. Mathematically, this condition reads as

$$|d_{i,m} - d_{j,n}| \leq \sqrt{(S_{x,i} - S_{x,j})^2 + (S_{y,i} - S_{y,j})^2} + \delta_{\text{P}} \tag{3.18}$$

with $1 \leq i,j \leq S$, $i \neq j$ the index identifying the respective sensor, and m and n the target indices of the respective sensor, i.e. $1 \leq m \leq T_i$, with T_i the number of targets detected by sensor i. Usually a large number of targets is detected, as most scattering centers will be detected as targets. Therefore the number of combinations that fulfill Eq. 3.18 is large. Furthermore another case has to be obeyed. It is the case of an object that is not seen by all sensors or is seen by one sensor with a RCS that differs heavily from that seen by

the other sensors, as described in Sec. 3.4.2. Taking into account the blind and quasi-blind sensors, it is necessary to additionally create sets, that consist of less than S range - amplitude pairs. Given S sensors, it makes sense to demand for at least $\lceil S/2 \rceil$ information pairs, i.e. at least half the sensors do get useful results. This number is arbitrary, but a minimum of two pairs for 2D imaging can be stated. For a three sensor system, it means that two pairs are enough. Two possible scenarios where one sensor is blind or quasi-blind are the following:

- A target with a high azimuth angle, i.e. an object to the very right or left of the ahead looking radar.
- A target straight ahead, that has comparable RCS for the symmetric side sensors but a highly different one for the center sensor.

For these and comparable cases, the missing information will be displayed by adding zero pairs in the respective tables. Taking into account quasi-blind sensors expands the list, where three sensors detect a single target each, to a list of 4 sets. One set is the scenario, every sensor detected roughly the same RCS, three of them assume that one sensor was quasi-blind. The following table contains a small example that makes clear how fast the number of sets of possibly corresponding pairs grows. Though Tab. 3.2 may imply

Sensor 1		Sensor 2		Sensor 3	
d	A	d	A	d	A
5.8800	1.3612	5.8920	1.2003	5.9880	0.6604
13.2840	0.4442	12.7680	0.1461	12.5880	0.0843
22.1640	0.0176	13.1400	0.4171	13.1160	0.1924
		21.9720	0.0163		

Tab. 3.2: Table of sensor responses for a three sensor scenario, with two targets visible for all sensors and two target visible to only two sensors

that ($d_{1,1}$,$d_{2,1}$,$d_{3,1}$), ($d_{2,2}$,$d_{3,2}$), ($d_{1,2}$,$d_{2,3}$,$d_{3,3}$), and ($d_{1,3}$,$d_{2,4}$) form sets with corresponding distance information, this cannot be guaranteed. Therefore, all possible sets have to be created and tested for their minimum J value. As already mentioned, each sensor target list is extended by one zero target, to cover the case of a quasi blind or blind sensor. Thereafter, all possible sets are created, with the boundary condition that the number of blind or quasi-blind sensors is not greater than $S/2$. This process yields Tab. 3.3. The table contains only the combined distance information, as amplitude information is not used as a criterion to form the sets of possibly corresponding pairs. The four outer columns together contain all combinations that will be checked by the algorithm. The numbers in the columns S_s indicate the target number of the respective sensor according to Tab. 3.2, whereas K is the number of the current combination. So the first column combination in Tab. 3.3 has to be read as the combination of the following distance information ($d_{1,1}$,$d_{2,1}$,$d_{3,1}$). The combinations have been split up into four groups as displayed with four columns. With the given

K	S_1	S_2	S_3
1	1	1	1
2	–	1	1
3	1	–	1
4	1	1	–

K	S_1	S_2	S_3
5	2	2	2
6	2	2	3
7	2	3	2
8	2	3	3

K	S_1	S_2	S_3
9	–	2	2
10	–	2	3
11	–	3	2
12	–	3	3
13	2	2	–
14	2	3	–
15	2	–	2
16	2	–	3

K	S_1	S_2	S_3
17	3	4	–

Tab. 3.3: All possible combinations that are checked by the algorithm for their minimum J value

sensor locations $S_1 = (-0.5,0)$, $S_2 = (0,0)$, $S_3 = (0.5,0)$, the maximum distance differences result as $|d_{1,m} - d_{2,n}| \leq 0.5$, $|d_{2,m} - d_{3,o}| \leq 0.5$, and $|d_{1,m} - d_{3,o}| \leq 1$, with $m,n,o \in \mathbb{N}$ the target numbers of the respective sensor. Clearly, the first targets of S_1 can only correspond to the first targets of the other sensors. Column one therefore contains this combination plus the target one cases including one quasi blind sensor. Column two combines the 12 m and 13 m distance targets, disregarding the possibility of blind sensors. Column three takes into account the possibility of blind or quasi-blind targets for these targets. The last column holds the only possible combination for the most distant target and completes the list of all possible combinations. Combination 17 is a case with a blind sensor and no other detected targets that satisfy Eq. 3.18, so the result is a single possible combination. The entire list will be called list of possibly corresponding pairs (of distance-amplitude information). It is clear now, that the number of possible correspondences increases exponentially with the number of targets satisfying Eq. 3.18.

3.5.2 Choosing the Correct Target Location

For each of the above mentioned combinations, the matrix **J** is calculated and the minimum reasonable J value evaluated.

Special Cases of J

J is in general given by the sum of the deviation of the calculated RCS mean, as in Eq. 3.17, but a bonus malus system is introduced to account for special cases.

On the bonus side is the case, where a target of one sensor is listed within only one combination, e.g. target one of sensor two appears only in combination 14. Therefore the J value for combination 14 will be decreased by a certain amount j_b. Combination 17 is an example for this case. It makes sense to prefer these type of combinations, as it is very likely that the respective combination belongs to a true target location. The only possibility for such a combination to refer to a ghost target is the case where a noise spike was detected by the respective sensor. Bonus points can also be introduced for a set of

combination that use up all detected targets and at the same time do not use a detected target twice. Unfortunately, the creation of all possible combinations is brute force attack, which makes it extremely difficult to find out the set of combinations that fulfills that condition. Therefore, this part is not yet implemented into the algorithm.

On the other hand, there are several cases where J is increased, due to several criteria. One is the assumption of a quasi-blind sensor. Exactly, in case a combination is checked that has a missing distance information for one or more sensors, a certain value $j_{\mathrm{m,d}}$ is added to J for each missing distance information. So for two missing distances, which is of course not possible for the three sensor system, $2j_{\mathrm{m,d}}$ is added. The algorithm furthermore requires at least two amplitude values to be above the minimum digital value, i.e. the smallest value that can appear at the ADC output, to ensure the usage of real targets. For not fulfilling this condition, the J value of the respective combination is increased by $j_{\mathrm{m,A}}$. The third case, causing an additional value for J results from an ambiguous area that is zero, i.e. Eq. 3.6 contains not a single point. This may result from a good sensor precision, i.e. small δ_{P} and coarse meshing of the FoV. The value added for this case is referred to as $j_{\mathrm{m,M}}$.

For the implementation, a choice for the values of the bonus malus system needs to be taken. It is recommended to choose the j values, so that they are on the order of the largest calculated RCS values.

3.5.3 Limiting Possible Targets to the Field of View

Combinations that do not correspond to a real target may result in calculated locations outside the FoV. Clearly, these are so called ghost targets. Eliminating them is trivial, as the maximum azimuth angle is known. It results from the beamwidth of the antennas. So within this step, all targets from the list of possibly corresponding pairs are eliminated that are outside the FoV.

The J List

At this point of the algorithm, two lists exist. One contains the calculated positions according to all combinations of the list of possibly corresponding pairs and the other one contains the respective J value. As mentioned in Sec. 3.5.1, the number of possible target locations in this list is much higher than the number of real targets. Though possible locations outside the FoV were already eliminated, there will be much more possible locations left than targets in the scenario. Therefore, the possible locations are listed, sorted by the corresponding J value as in Tab. 3.4. The task is now to further reduce the list, so that each detected peak appears only in one combination and that the sum of the J values is minimal. As this task is highly complex, it was reduced to a simpler decision rule. The list is scanned for equal positions. If two combinations k_1 and k_2 that result in the same position are found, the list is reduced by one entry, namely k_2. The J value of the remaining position i that was not removed is set to the mean of both, i.e. $(J_{k_1} + J_{k_2})/2$. This method can be extended to merge all positions that are equal within the range precision.

K	x	y	J
17	0.1	11	0.0061
1	-0.4	2.9	0.0206
8	0.9	6.5	0.0928
5	3.0	5.7	0.1298
6	0.8	6.4	1.0213
4	0	2.8	10.0055
9	3	5.6	10.0065
10	-2.7	5.8	10.0152
12	1.9	6.3	10.0184
2	-1.0	2.8	10.0190

Tab. 3.4: The J list for the example in Tab. 3.2

3.6 Prerequisites and Limitations

3.6.1 Efficiency

Fig. 3.9 shows the result of the above mentioned example. It shows the calculated positions as well as the real target positions. The figure exhibits several ghost targets as well as a non detected target. These effects depend on a number of reasons that will be discussed in the following.

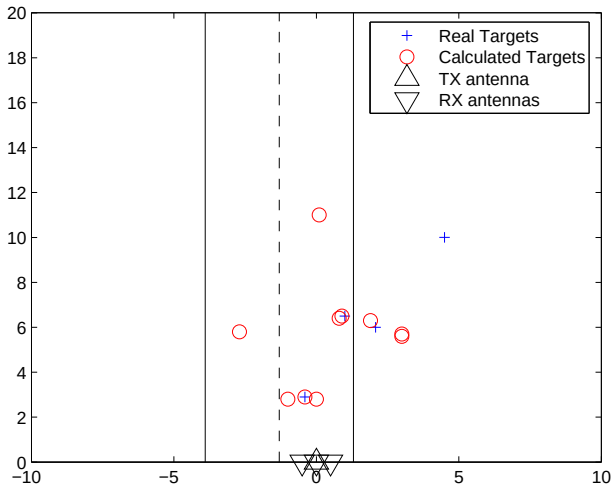

Fig. 3.9: Roadside scenario showing the example from Tab. 3.2

A major limitation is of course the required criterion as mentioned in 3.3 to decide whether the calculated RCS belong to the same object. It is not generally valid that the RCS is constant for different aspect angles. The system is intended for use in automotive

environments, which results in maximum distances between the sensors of roughly 1.5 m (width of a car). This leads to a maximum difference of the aspect angle of 17° for a distance of 5 m. Furthermore the setup shown in Fig. 2.15 is symmetric, i.e. the transmit antenna is located in-between the outer receive antennas. Assuming quasi-symmetric RCS, i.e. $\sigma(\varphi,\vartheta) \approx \sigma(-\varphi,\vartheta)$ further reduces the maximum difference between the RCS seen by the different receive antennas. The assumption of quasi-symmetric RCS is based on the fact that many obstacles in a roadside scenario can be split up into elements resembling cylinders, which do have symmetric RCS [40, 41].

Another vital prerequisite is of course the knowledge of the antenna characteristics needed to calculate the RCS from the detected amplitude. For the simulation, we assume two-dimensional antenna characteristics known with a resolution of one degree. It is desirable that the antennas in the system have sidelobes only outside the field of view of the system. Sidelobes within the field of view with narrow spacing would require higher SNR and a higher resolution of the A/D converter for the same efficiency.

The prerequisite of constant RCS over small changes of the aspect angle can be expressed in a different way as soon as antenna characteristics are taken into account. Instead of postulating constant RCS, the requirement is now that the change in antenna gain dominates the difference in received power, i.e.

$$\frac{|\sigma(\varphi) - \sigma(\varphi + \delta\varphi)|}{\sigma(\varphi)} \ll \frac{|G(\varphi) - G(\varphi + \delta\varphi)|}{G(\varphi)} \tag{3.19}$$

with $|\delta\varphi| > 0$, and G the antenna gain.

Limitations of the system as far as resolution is concerned have to be mentioned as they do not follow neither the standard rules of PN radar nor those of coherent radar sensors. Clearly both relations dealing with resolution, $\Delta\vartheta = \frac{\lambda}{d(\mathrm{RX}_i,\mathrm{RX}_j)}$, and $\delta_\mathrm{R} \propto c_0 \cdot T_\mathrm{c}$ impact the overall resolution for the presented system, but increases over existing limitations are possible. The range resolution limit is dominant for the system performance, especially if two targets cannot be separated by any of the S sensors.

The maximum range of the system under investigation clearly depends on the SNR at each sensor output. Using PN radar techniques, we get a linear dependency between SNR and code length. Code length again is limited by the time available. There will be a minimum update rate of the radar image required by the customer. A major part of this time will be used to perform the necessary correlation, no matter whether analog or digital correlation is performed. A more than optimistic approximation leads to a maximum range of less than 170 m. This value was calculated for a minimum image update rate of 10 Hz, which leads to maximum code length of 10^4 chips, with a bit duration of 1 ns, assuming the processing algorithm consumes no time or is performed during the next correlation cycle. The chip duration of 1 ns sets the range resolution to 30 cm for the distance TX-object-RX. A maximum $P_\mathrm{EIRP} = 20\,\mathrm{dBm}$, a minimum noise level of -70 dBm at the receiver together with a spread gain of 40 dB lead to $\frac{P_\mathrm{RX}}{P_\mathrm{TX}} \geq -130\,\mathrm{dB}$. Assuming $G_\mathrm{TX} \cdot G_\mathrm{RX} \leq 30\,\mathrm{dB}$ and a RCS of $\sigma = 1\,\mathrm{m}^2$, which corresponds to a metal sphere with $r \approx 0.6\,\mathrm{m}$, the above mentioned value can be calculated as an absolute upper limit.

3.7 Logical and Chronological Flow Chart of the Algorithm

The following section will give a short overview of the entire algorithm, in logical as well as in chronological order.

3.7.1 Logical Flow Chart

The flow chart in Fig. 3.10 states the logical order of the elements of the algorithm, including the data flow and the influence of each step onto the entire algorithm. Data input ports are drawn as parallelograms, whereas processes that use information other than the output of the predecessor step are characterized by parallelograms with curved vertical lines.

3.7.2 Time Flow Chart and Time Limitations

Fig. 3.11 makes clear that certain steps, needed to gain a radar image, must be performed in series. With the given boundary condition of a minimum update rate of 10 Hz, duration limits for the steps can be derived. The scenario from which the maximum processing time is derived is two cars approaching each other. Assuming a highway with two cars traveling at 100 km/h each, this makes a relative speed of 60 m/s of one car approaching the other one equipped with the radar system. This yields a 6 m distance of the location of the car between two images. This equals almost two car lengths and is the maximum deviance that can be accepted between two images.

The data acquisition step includes the transmit and receive process of the sensor, but is made up mainly by the analog correlation process. As already mentioned earlier, the time required for this step is on the order of $L^2 T_c$, i.e. 0.13 ms for the case in Sec. 3.5, but already 2.1 ms for a 1023 bit m-sequence. For serial I/Q-correlation, these values double. Although it is possible to limit the ACF to e.g. 50% of its full length, which yields a correlation time that is shorter by 50%, the order of the required time remains, i.e. twice the code length meaning four times the correlation time. Though the correlation takes a certain amount of time, these numbers show that almost the entire 100 ms can be used for the processing algorithm. A full simulation of the entire system in MatLab, described in Sec. 4.3, shows that the required time is on the order of seconds. During a test, it could be shown that coding essential parts of the code in C reduces the time required for the algorithm for a 0.1 m meshed FoV to a level, that is significantly below a second.

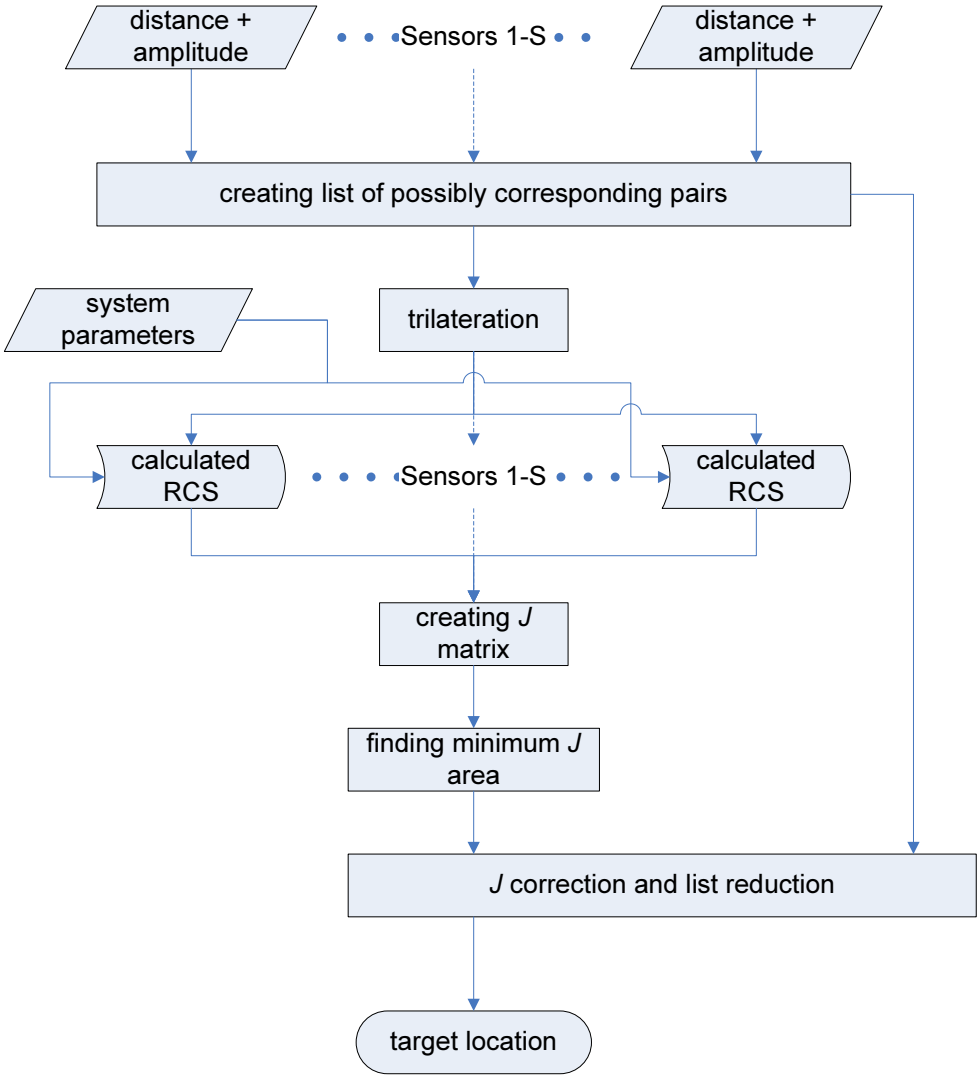

Fig. 3.10: Flow chart of the described algorithm

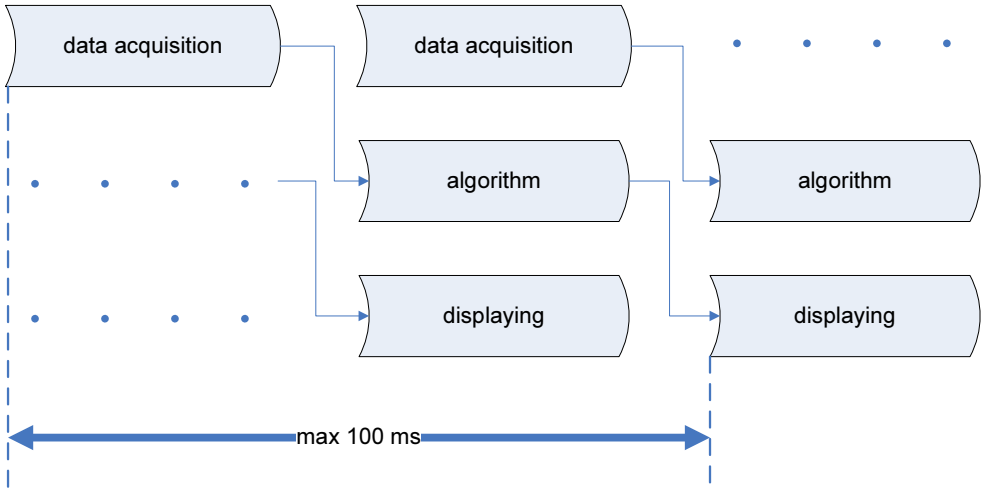

Fig. 3.11: Time flow for the entire imaging system, showing critical path for the update rate

4. SIMULATION AND REALIZATION

This chapter describes the realization of parts of the system, such as the correlator, as well as the implementation of the simulation. The realization of a PN radar front end is treated in detail in [18].

4.1 Front-End

The radar front end was taken from a project currently to be finished at the Fachgebiet Höchstfrequenztechnik [18]. It comprises the development of a cheap 24 GHz PN radar sensor. The intention of the project was to develop a cheap, i.e. 30 US Dollar device, with a high dynamic range and a reasonable range resolution. It was developed with a strong focus on the automotive industry. The functionality of the imaging algorithm can also be reached utilizing other radar sensors providing distance and amplitude information, e.g. [21, 42–44]. The choice for the sensor was made based on fabrication cost and availability. Fig. 4.1 shows the working sensor, made up by single components. In the upper part of the

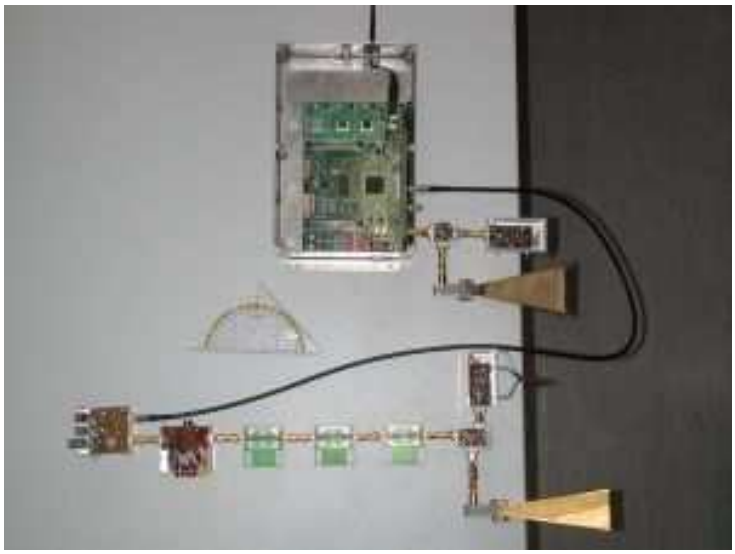

Fig. 4.1: Radar sensor made up by connected components

picture, an FPGA creates the required PN sequence and provides it to the transmitter. The transmitter output goes straight into the transmitter horn antenna. On the lower part of the picture, the receive unit is depicted. It consists of the receive horn antenna,

a mixer that transforms the RF into an IF signal, an amplifier chain with three stages, a detector and the correlator unit. Obviously, the depicted sensor does not utilize the IF correlator principle. Replacing the baseband correlator by an IF correlator is described in Sec. 4.1.1. This distributed sensor layout has the advantage that single stages can be replaced by alternative designs. This was especially useful for the integration of the new correlator concept, as the detector and baseband correlator were easily replaced by the new IF correlator module.

The sensor in Fig. 4.1 was further developed into an integrated layout. Fig. 4.2 shows the final layout, where the entire sensor is integrated onto a printed circuit board. The board consists of multiple layers of FR4 and one layer of RF substrate. Clearly visible, the RF devices in the receiver and transmitter parts are mounted directly to the RF substrate, whereas all other elements are mounted on FR4. This layout can be used for the described

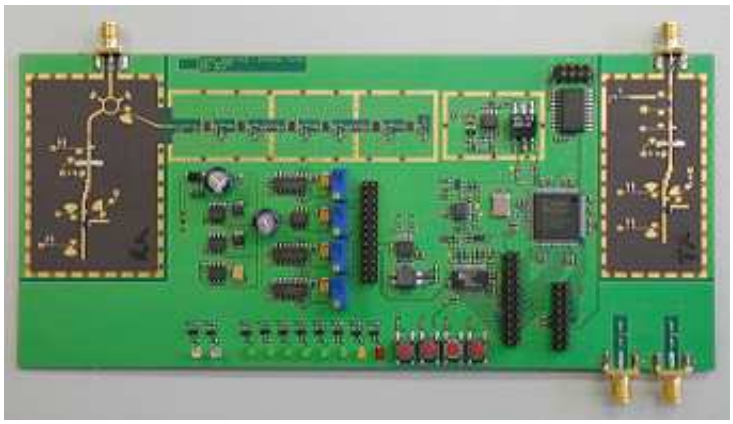

Fig. 4.2: Photo of the radar sensor completely integrated on a PCB

imaging system, though the advantages of the IF correlator method cannot be used, as the baseband correlator is integrated on the board.

The above mentioned layouts were implemented using different PN sequences by reconfiguring the respective FPGA.

4.1.1 Correlator

The following section treats the replacement of the detector and the baseband mixer in the original sensor design by an IF correlator. The theory of this method is described in Sec. 2.4.

Practical Considerations

The following design is based on the analog correlation principle without using any memory elements. Fig. 2.16 shows the schematic of an IF correlator. A PN code of length L is transmitted and provided to the correlator with a variable delay of $k\Delta\tau$, $k = [0 \dots K-1]$,

with

$$K = \frac{LT_\mathrm{c}}{\Delta\tau}. \tag{4.1}$$

$\Delta\tau$ is chosen so that $K \in \mathbb{N}$. After the reference is transmitted completely, k is increased by one, until it reaches $K-1$. Thereafter it is reset to zero. Using this principle, it is clear that a full correlation takes KLT_c. In case the transmitted power of the radar is not sufficient to cover the whole unambiguous range or the information from distant objects is unwanted, the correlation time can be reduced significantly. Under the assumption, that objects further away than d_DL are not of interest, it is not useful to sweep k up to $K-1$.

$$K' = \frac{2d_\mathrm{DL}}{c_0\Delta\tau} \tag{4.2}$$

is introduced and k is limited to $[0 \ldots K'-1]$ now. For $T_\mathrm{c} = 2\,\mathrm{ns}$ and $L = 1023\,\mathrm{bit}$, the unambiguous range would be more than 300 m. No radar operating within the power limits of ISM bands, will be able to cover this distance, due to free space attenuation, see Eq. 3.8. This method results in a time discrete ACF, i.e. corresponds to an ACF that is sampled at a rate of $1/\Delta\tau$. Clearly, the correlator output equals an ACF only for the case that the scenario that reflects the received signal, does not change over $K'LT_\mathrm{c}$, as already required in Sec. 3.2.4.

Correlator Layout

The described IF-correlator was designed and fabricated. For the concept validation it is sufficient to realize the proposed system at an IF and to leave out the RF transmission part, i.e. TX antenna - target - RX antenna. An arbitrary phase for the received signal was realized using a variable delay line. A 1023 bit m-sequence is provided by an FPGA board with a chip duration of 5 ns. The FPGA provides a second output port for the reference, with delay steps of $\Delta\tau = T_\mathrm{c}$, which yields a time discrete ACF. The time discrete ACF

$$\varphi_{s_\mathrm{rec}s_\mathrm{ref}}(k\Delta\tau) = \int_0^{LT_\mathrm{c}} s_\mathrm{rec}(t) \cdot s_\mathrm{ref}(t + k\Delta\tau)\,\mathrm{d}t \tag{4.3}$$

with $k \in \mathbb{N}$, is derived from Eq. 2.5. The code is modulated onto the intermediate frequency f_0=1.4 GHz. The unipolar on off keying (OOK) modulator was implemented by means of a diode switch, whereas the bipolar binary phase shift keying (BPSK) modulation is performed using a mixer. Both modulators were fabricated for this purpose and are depicted in Fig. 4.4. For the correlation, the Analog Devices chip AD8347 with an input frequency of 800–2700 MHz was used. In Fig. 4.3 the correlator using the AD8347 with two IF input ports and the correlation output port is shown.

Measurements

Measurements were taken by setting up the circuit and connecting an oscilloscope to the correlator output. Several characteristic dependencies were measured. All of them show

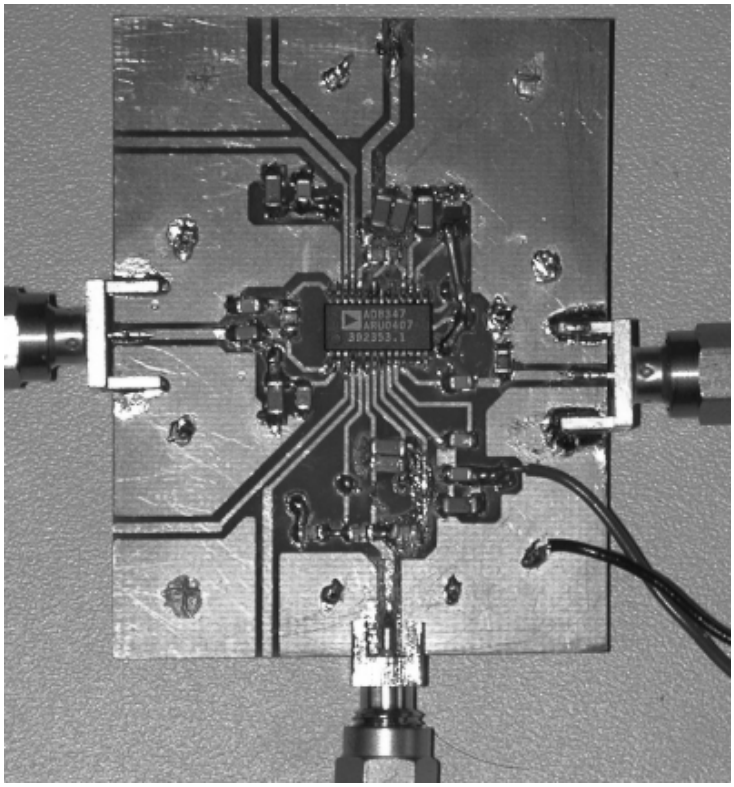

Fig. 4.3: Photograph of the fabricated IF-correlator using the AD8347

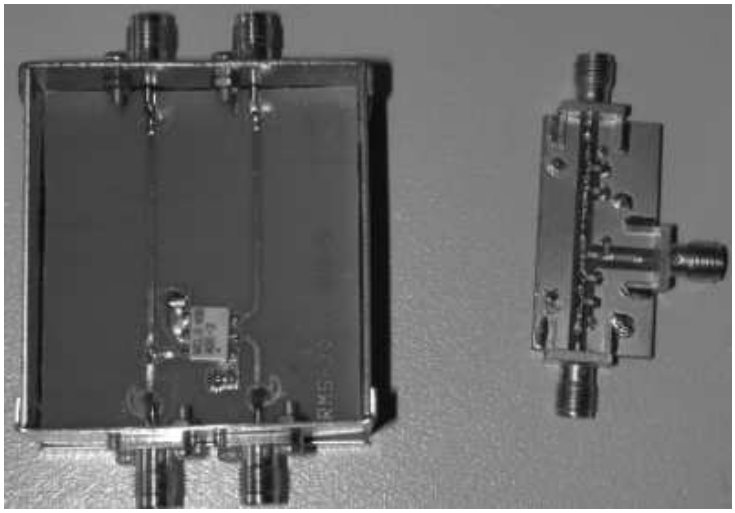

Fig. 4.4: Modulators to modulate the FPGA signal onto the IF carrier, left the boxed BPSK modulator, right an OOK modulator

ACFs, i.e. the amplitude of the correlator output over the delay time of the reference. The delay time is normalized to the code length. At first, the influence of the intermediate frequency was investigated. In Fig. 4.5 the frequency dependence as predicted in Sec. 2.4.3 is clearly visible. Frequencies from 1.30 GHz to 1.50 GHz were investigated in steps of 0.01 GHz, to find the ideal frequency. The best measured case with $f_0 = 1.47\,\text{GHz}$ and a nearby frequency of $f_0 = 1.50\,\text{GHz}$ are shown in Fig. 4.5. The figure shows clearly that not only the noise floor increases by a factor of 4, but also that the absolute value of the peak decreases by roughly 30%, for the non-ideal frequency, when compared to the ideal one. This results in a main-to-side-lobe ratio that is roughly 14 dB lower. In a second measurement series, the differences between the correlation of two unipolar sequences and the correlation of a unipolar with a bipolar sequence were verified. Fig. 4.6 shows the disadvantages of an OOK-OOK correlation. It is clearly visible that the DC offset is significantly higher than for the OOK-BPSK correlation. In theory a maximal main-to-side-lobe ratio of 6 dB is possible for OOK-OOK correlation. These measurement results were obtained using non-ideal code shapes obtained from the modulator without any effort put into pulse forming.

4.1.2 A/D-Converter and Peak Detector

A/D-Converter

As already mentioned numerous times, the dynamic range of the radar sensors determines the accuracy and the precision of the imaging system. This is due to the high resolution required to detect small targets in the presence of greater ones. For the ADC of the final system, the quantization depths needs to be high, 12–14 bits is assumed a good size, that is available at a moderate price for the required sampling rate of 1–10 MS/s.

During this work, the correlator output was connected to a digital oscilloscope, namely a Tektronix TDS220. The oscilloscope data was thereafter read into a PC using a GPIB interface. It has a 100 MHz bandwidth and a sampling rate of 1 GS/s with an 8 bit digital output. Therefore, the sensitivity of the system is low.

For the simulation, the ADC was implemented as a logarithmic converter. The ADC subroutine of the simulation takes the minimum and the maximum discrete value, $q_{\min}$ and $q_{\max}$, the discretization depths in bits, and of course the signal to be discretized as input arguments. A vector with the digital values, from $q_{\min}$ to $q_{\max}$, spaced logarithmically, i.e. the exponents of the base 10 are spaced linearly, is created. As an example, a 2 bit, i.e. 4 digital values, quantization vector, with $q_{\min} = 1$ and $q_{\max} = 10$ is given as

$$q = \begin{pmatrix} 10^0 \\ 10^{1/3} \\ 10^{2/3} \\ 10^1 \end{pmatrix} = \begin{pmatrix} 1 \\ 2.14 \\ 4.64 \\ 10 \end{pmatrix}. \tag{4.4}$$

The analog input values are then replaced with the closest digital value, i.e. the absolute of the difference between the analog and the chosen digital value has to be minimal.

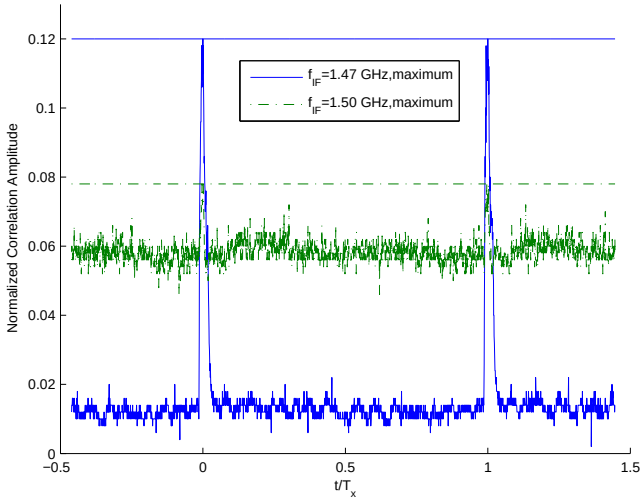

Fig. 4.5: Measured frequency dependence of the correlation result

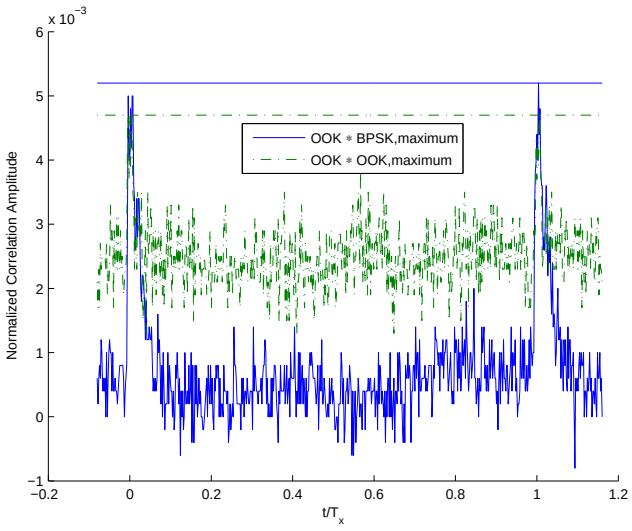

Fig. 4.6: Measured results of OOK-OOK and OOK-BPSK correlations

Peak Detector

Peak detection is performed within the microprocessor device by an algorithm described in Sec. 2.5. It was implemented as suggested by [35]. The subroutine for peak detection takes the absolute of the I/Q-correlation and the peak excursion as functional arguments. The proper peak excursion is a system parameter that has to be determined by accounting for environmental parameters, such as maximum range, and system parameters, such as maximum antenna gain, quantization depths and amplifier gain. In general, the peak excursion parameter will be determined empirically, i.e. a value needs to be found, that provides good recognition of real targets but avoids the detection of noise spikes as targets.

Furthermore, an experimental stage of a detected peak evaluation module was introduced. As the peak detector gets the absolute as well as the phase of the I/Q-correlation, the idea came up to exploit the phase information, for better peak detection. The idea was that peaks of real targets should have a constant phase of the I/Q-correlation resulting from the fixed phase argument in Eqs. 2.30 and 2.32. Noise peaks on the other hand will show arbitrary phases. Therefore, the idea was to check the phase constancy around the point that corresponds to the detected peak in the absolute. Assuming the peak detector found a peak at $\tau = nT_\mathrm{c}$, then the phase of the correlation from Eq. 4.5

$$\chi(\tau) = \arctan\left(\frac{\varphi_{s_\mathrm{rec}s_\mathrm{ref,Q}}(\tau)}{\varphi_{s_\mathrm{rec}s_\mathrm{ref,I}}(\tau)}\right) \tag{4.5}$$

has to fulfill the following condition

$$|\chi(nT_\mathrm{c}) - \chi(nT_\mathrm{c} + \tau_\chi)| < \delta_\chi \tag{4.6}$$

with δ_χ the phase deviation, a value that has to be determined empirically like the peak excursion δ, and $-\tau_\mathrm{P} < \tau_\chi < \tau_\mathrm{P}$ the peak width. τ_P depends of course on the pulse form, as the shape of the ACF depends on it. Furthermore, it can be adjusted manually to system parameters, i.e. decreased, to help small targets fulfill the condition in Eq. 4.6. Speaking figuratively, Eq. 4.6 means a area in the phase plot that is flat, i.e. the phase is constant. Fig. 4.7 shows the absolute of a correlation, whereas in Fig. 4.8, the corresponding phase is plotted. Clearly visible are flat areas corresponding to the peaks. Unfortunately, using discrete values for calculating the phase via the arctan-function, results in a flattened plot, compared to the analog case. Fig. 4.8 shows the comparison of the discrete and the analog correlation phase.

4.2 Free Space and Target Simulation

The simulation of the free space in between the radar system and the target is necessary to take certain noise effects as well as the free space attenuation into account. Special interest was on the topic of target simulation. Unlike free space simulation, it is not used to simulate the entire system, as RCS are assumed to be known. If it was possible to calculate the RCS of common roadside objects efficiently, imaging would be a lot easier.

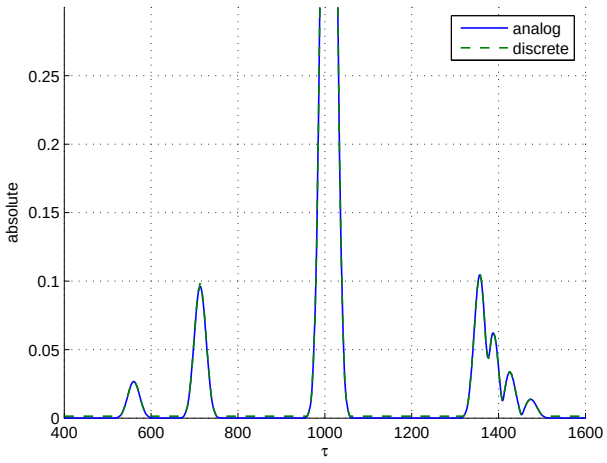

Fig. 4.7: Analog and discrete absolute of an IQ correlation, with several peaks

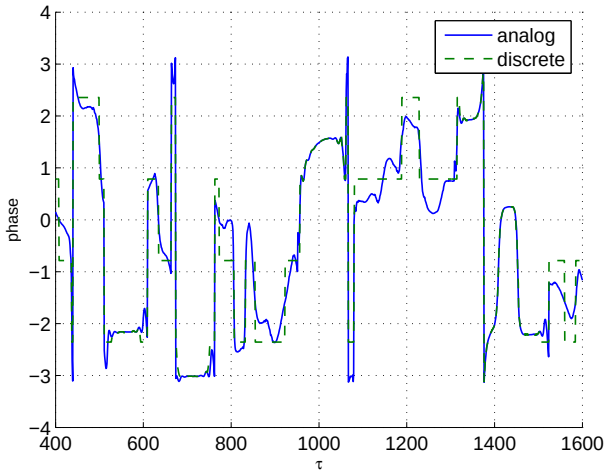

Fig. 4.8: Analog and discrete phase of an IQ correlation, containing several flat areas corresponding to peaks in Fig. 4.7

Detected targets could be compared with the calculated RCS and in case of congruence, the system assumes the respective object at the target location instead of depicting just a dot. Therefore easy formulas need to be found and their suitability needs to be tested.

4.2.1 Radar Target Simulation

The algorithm that is the core of the imaging system is based on the assumption that at least two radar sensors see the same object with a similar RCS for slightly different aspect angle. It is assuming basically that the antenna characteristic changes faster with aspect angle than the RCS. This assumption is of course not valid for all objects. Ideally, only objects with cylindrical symmetry along a vertical axis make up the scenario to be imaged. Obviously, cylinders match this criterion. Therefore the aim was to identify as many roadside objects as cylinders or composition of multiple cylinders as possible. This is possible for a variety of objects, such as trees, poles of traffic signs and, most important, people.

Cylinders or objects resembling cylinders in RCS would have another important advantage in radar imaging. Literature [40, 41, 45, 46] mentions several formulas to calculate the RCS of cylindrical elements. If this formulas would prove correct for the objects under investigation, the imaging system would get a chance to derive the real size of a detected target by inserting the calculated RCS into the respective formula. Deriving the dimensions of objects is essential for 3D imaging. Therefore, the following section treats the accordance of these formulas with the RCS obtained by a full wave simulation of cylinders of different materials. Some results were taken from [47].

Definition - Radar Cross Section

Effective Area - Effective Width The Radar Cross Section has the dimension of an area and describes the effective scattering area of an object. This effective area σ depends on the angle of incidence (φ_i, ϑ_i) as well as the observation angles (φ_s, ϑ_s). Obviously the RCS describes in general a bistatic setup. For the monostatic case only the backscattering is of interest, i.e. the Radar Cross Section for $\varphi_s = \varphi_i$ and $\vartheta_s = \vartheta_i$ (see Fig. 4.15 for definition of angles). The bistatic RCS is defined as follows:

$$\sigma(\varphi_i,\vartheta_i,\varphi_s,\vartheta_s) = 4\pi \cdot \lim_{r\mapsto\infty} r^2 \cdot \frac{\left|E_s\left(r,\varphi_s,\vartheta_s\right)\right|^2}{\left|E_i\left(r,\varphi_i,\vartheta_i\right)\right|^2} \tag{4.7}$$

For objects that extend infinitely to one dimension, the fields do not depend on this dimension any more. This means on the one hand that there is an infinite amount of power, but on the other hand it allows to solve the problem in only two dimensions. This yields not an effective area as known for 3D objects, but an effective width:

$$\sigma_c(\varphi_i,\vartheta_i,\varphi_s,\vartheta_s) = 2\pi \cdot \lim_{r\mapsto\infty} r \cdot \frac{\left|E_s\left(r,\varphi_s,\vartheta_s\right)\right|^2}{\left|E_i\left(r,\varphi_i,\vartheta_i\right)\right|^2} \tag{4.8}$$

Forward Scattering As the RCS describes the ratio of the scattered to the incident E-field, a high RCS can therefore not only describe a reflection area but also a shadow area. This means that a high RCS in the forward scattering case is expected for objects that shield the E-field. This scattered field in forward direction interferes destructively with the incident field so that it results in a low total E-field.

Approximation of the RCS

Infinitely Long Cylinder Exact closed form solutions do exist only for very few objects. Among these are infinitely long cylinders, which can either be perfectly conducting, homogeneous or perfectly conducting with homogeneous coating. As mentioned earlier, the distribution of the E-field is the same in every cross section that is perpendicular to the cylinder axis. The solution of this problem therefore gives an effective width σ_c which can be taken from [40], pp. 271ff. The material constants ϵ_r and μ_r for homogeneous cylinders may be complex, i.e. the objects can have finite conductivity. The given series solution is valid for both TM-, i.e. E-vector is parallel to the plane of incidence, and TE-polarized waves, i.e. the E-vector is perpendicular to the plane of incidence. The formula gives for each polarization two solutions: one for the scattered wave that has the same polarization as the incident wave and one for the depolarized component, which exists for non perfectly conducting cylinders with $\vartheta_i \neq 90°$. The scattered wave for infinitely long cylinders propagates in only one elevation direction $\vartheta'_s = \pi - \vartheta_i$.

Cylinders of Finite Length The Radar Cross Section of cylinders of finite length with a height h of several wavelengths (roughly $h > 3\lambda_0$) can be approximated. For the approximation Huygen's principle and the following assumptions are used:

1. Near the cylinder radially, i.e. $\frac{a^2}{\lambda_0} \leq r \leq \frac{h/2^2}{\lambda_0}$, the E-field is the same as for an infinite cylinder, i.e. it is proportional to $\frac{1}{\sqrt{r}}$ and therefore outweighs the field proportional to $\frac{1}{r}$.

2. The width of the scattered field in z-direction is limited by the height of the cylinder.

The plane of integration is parallel to the cylinder axis and has its reference coordinate system with origin on the scattered wave vector k_0^s. Given the above assumptions, the integration plane reduces to an area limited in height to $\pm h/2$ and in width to $\pm\sqrt{\frac{(h/2)^2-a^4}{\lambda_0^2}}$. The integration yields the magnetic Hertz vector which is used to derive the scattered E-field at the observation point. The integral can be solved in a closed form with the stationary phase method and results in a factor

$$L = \frac{4k_0h^2}{\pi}\cos^2(\vartheta_s)\,\mathrm{si}^2\Big(k_0h\big(\sin(\Psi_i)+\sin(\Psi_s)\big)\Big) \tag{4.9}$$

with $\Psi_i = 90^\circ - \vartheta_i$ and $\Psi_s = 90^\circ - \vartheta_s$.

Ansoft HFSS Simulation

To simulate the scattered field on a finite elements frequency domain engine like HFSS, the complete volume within a so called *Radiation Box* has to be discretized. This box must have a minimum distance to the closest scattering object of one fourth of the wavelength. For non perfectly conducting cylinders one has to consider whether to simulate the field within the scattering object or whether it is sufficient to use surface currents, because of negligible skin effect, which saves a reasonable amount of time. Another method to save simulation time is to introduce a symmetry plane in the plane of incidence. Depending on the type of incident wave perfect-E or perfect-H planes have to be used. Incident waves were used as sources for all simulations, i.e. plane waves with either TM- or TE-polarizations. Tab. 4.1 shows the geometry and the cylinder material for each project. All cylinders had jackets consisting of 20 rectangles, as this conserved simulation time and delivered results that deviated less than 0.1% from simulations with real cylinders.

Name	a_s/mm	h_s /mm	a_r /mm	h_r /mm	Material	ϵ_r	μ_r	σ /(S/m)
line1	2.5	80	6	90	copper	1	0.999991	$5.8 \cdot 10^7$
line1-75	2.5	60	6	67.5	copper	1	0.999991	$5.8 \cdot 10^7$
line7	2	40	6.5	49	water_sea	81	0.999991	4

Tab. 4.1: HFSS projects for RCS validation

Comparison

In the following section, cylinders of different materials and geometries were illuminated and observed from different angles. The graphs show the results of the simulation, the result of the approximation formula and in some cases the relative error, defined as

$$\delta_{\text{rel}} = \frac{|\sigma_{\text{approx}} - \sigma_{\text{HFSS}}|}{\sigma_{\text{approx}}} \tag{4.10}$$

All simulations and calculations were performed at a frequency of 24 GHz which corresponds to $\lambda_0 = 12.5\,\text{mm}$. Graphs that show σ over ϕ, with $\phi = \varphi_s - \varphi_i$, are drawn for the main scattering elevation angle $\vartheta_s = \pi - \vartheta_i$ only. In general we can state that the agreement for small $|\phi|$ is better than for large values. For radar application, only RCS for small ϕ are interesting as transmitter and receiver are spatially close together especially in automotive applications.

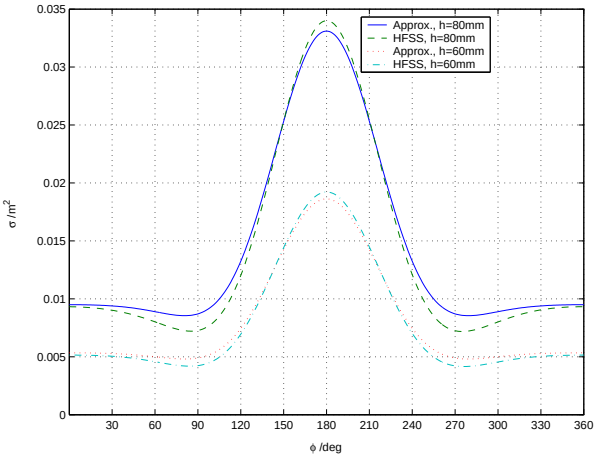

Fig. 4.9: Project *line1-75* and *line1*, TM

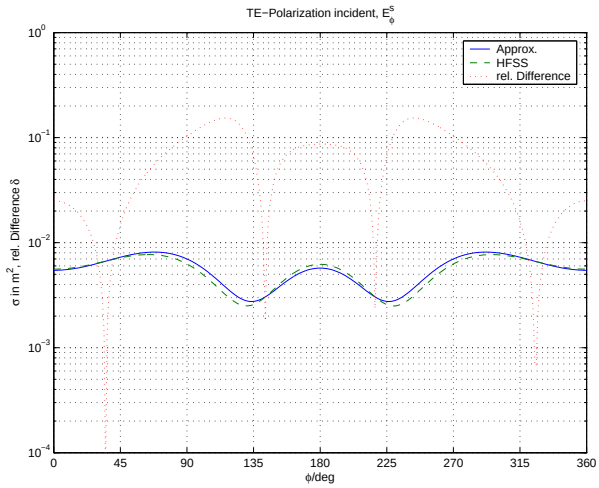

Fig. 4.10: Project *line1*, TE

Copper Cylinder, $\vartheta_i = 90°$ Fig. 4.9 shows that the quadratic dependence can be shown in the simulation as well as in the approximation. The ratio of the cylinder heights is 0.75. The polarization of the incident wave was TM.

Fig. 4.10 shows the results of TE illuminated cylinders. As already mentioned, the agreement is better for small angles.

Fig. 4.11 is the same copper cylinder again illuminated with a TM wave. The graph shows the deviation for constant $\phi = 0$ over ϑ_s. It shows clearly that the results agree only for the main scattering direction $\vartheta_s = \pi - \vartheta_i$. The approximated RCS decreases faster than the simulated one. One reason is the short cylinder height of only 3 wavelengths used here. The cylinder ends are not taken into account by the approximation formula. As a result of this assumption, better agreement over ϑ_s is expected for larger h.

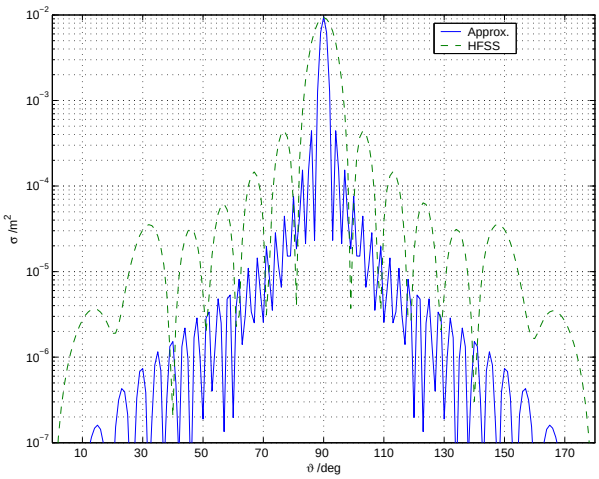

Fig. 4.11: Project *line1*, TM

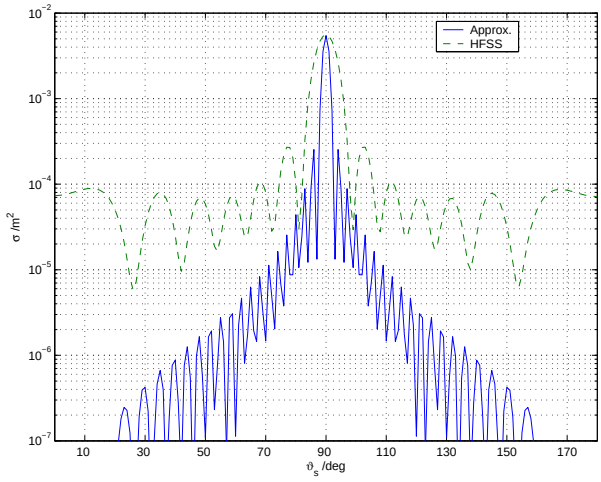

Fig. 4.12: Project *line1*, TE

Sea Water Cylinder, $\vartheta_i = 79°$ Sea Water was chosen as a dielectric material for two reasons. First it is assumed to have ϵ_r and μ_r similar to those of human tissue. The second reason was to validate if the approximation formula can be used for high ϵ_r materials, too. Fig. 4.13 shows in polar plots the RCS in m^2 over ϕ for $\vartheta_i = 79°$. Again it is clearly visible, especially for the TM illuminated case, that the agreement for small $|\phi|$ is good.

Fig. 4.14 shows the relative error for TM- and TE-polarized waves over ϕ for different incident elevation angles. The important difference between the two plots is that for TM-polarized wave, i.e. the E-field vector lies in the plane of incidence, the results get a lot better for $\vartheta_s \to 90°$. For TE-polarization the error remains roughly the same for the investigated range of angles.

Conclusion and Future Work

This section shows that it is basically possible to use approximation formulas instead of full wave simulations. Measurements could help to verify if the approximation for the RCS over ϑ_s for longer cylinders gets better. The next step in calculating RCS sequences would then be to coherently add the echoes of different cylinders in close proximity to each other.

4.2.2 Modeling the Channel

The channel is modeled within the full simulation in MatLab. Other than in a real world environment, where multiple noise effects occur, the simulation is reduced to the most important ones. All simulated noise effects are implemented in a separate module.

Additive White Gaussian Noise

Clearly, white Gaussian noise is the most common noise effect. It can be easily implemented within the simulation. The noise parameter SNR', describes the noise power in the model,

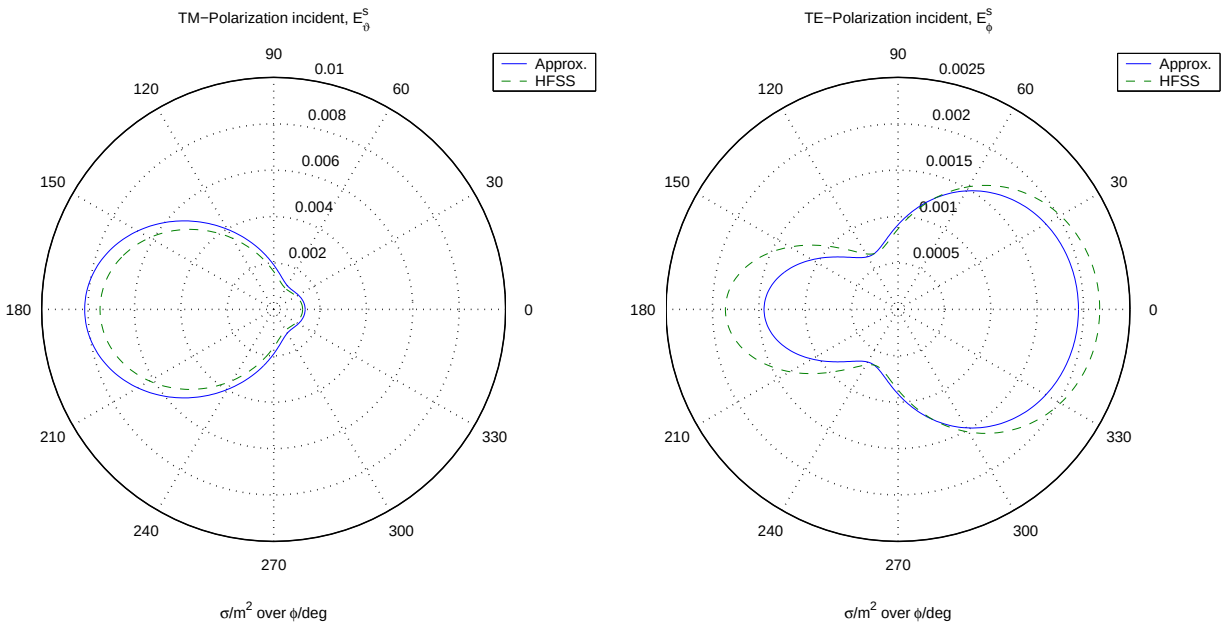

Fig. 4.13: Comparison RCS Simulation-Approximation in m^2 over φ_s, $\vartheta_s = 79°$, non-depolarized components, material *water_sea* ($\epsilon_r = 81$, $\mu_r = 0.999991$, $\sigma = 4\,S/m$), $\varphi_i = 0°$, $\vartheta_i = 101°$, project *line7* (a=2 mm, h=40 mm)

more precisely the ratio of the mean transmitted power to the mean noise power after the IF mixer. This uncommon ratio was chosen, as the ratio at the receiver depends on target properties, such as distance and RCS. If the standard definition was used, a reference target would have to be defined. This is obsolete when comparing the received noise to the transmitted power. This ratio furthermore can be transformed easily into the standard ratio, received signal power to received noise power, in case the target properties are known in addition to the system parameters. From the given

$$SNR' = \frac{\mathcal{E}\left\{P_{\text{signal,TX}}\right\}}{\mathcal{E}\left\{P_{\text{Noise,RX}}\right\}} \tag{4.11}$$

the mean noise power can be calculated. The simulated noise is then generated by MatLab and added to the received IF signal. The main effects of additive white Gaussian noise AWGN is detection of noise spikes as targets and non-detection of weak targets due to a noise floor in the ACF. Both effects can be simulated by adding the MatLab generated noise to the calculated received signal. The SNR at the receiver can be derived from Eq. 4.11 by replacing $\mathcal{E}\left\{P_{\text{signal,TX}}\right\}$ by $\mathcal{E}\left\{P_{\text{signal,RX}}\right\}$, which can be expressed by the radar equation Eq. 3.8.

DC Offset

As already mentioned in Sec. 2.4.1, DC offsets are an important problem for PN radars. The section also describes a method, namely the IF correlation, that can avoid DC offsets.

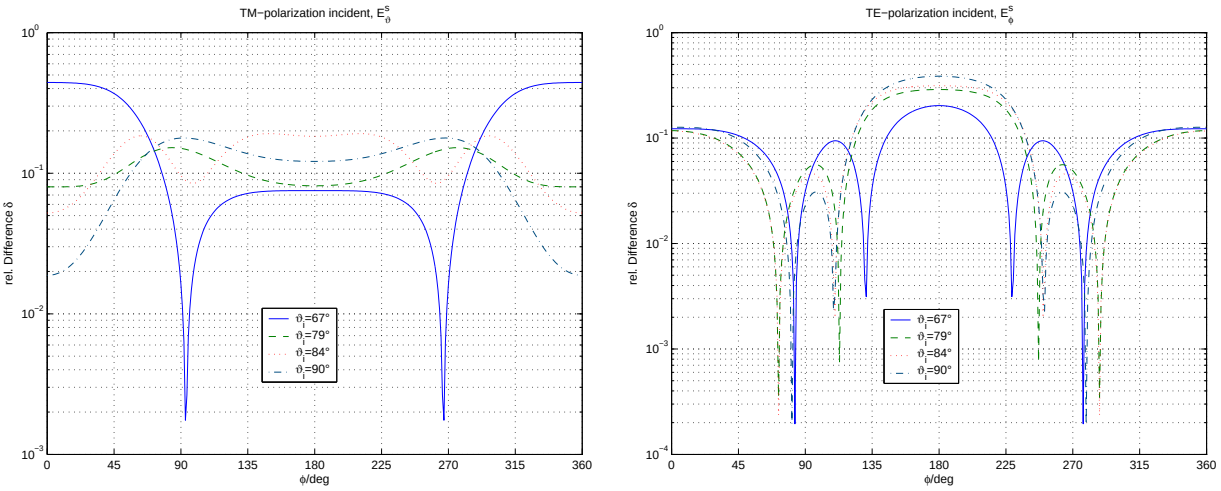

Fig. 4.14: Comparison RCS Simulation-Approximation, dependence of relative error on incidence elevation angle over φ_s, project *line7* (a=2 mm, h=40 mm)

In order to test the power of the IF correlator, DC offsets were implemented. A constant offset F is added to the amplitude of the received IF signal.

Variation of the Intermediate Frequency

In Sec. 2.4.3, the influence of the IF on the correlation result was discussed. This section proposes the usage of an intermediate frequency that is a multiple of the inverse chip duration. A variable IF in the simulation allows verification of the noise effects caused by a differing IF. The reason for such a divergence results from non-ideal elements, i.e. there is no infinite precision. Furthermore, the simulation was implemented, so that the IF of the received signal may differ from the IF of the reference signal. This situation eventually appears when the Doppler effect is taken into account. Assuming a chip duration of 1 ns, the bandwidth of the spreading sequence will be on the order of 1 GHz. This is narrow when compared to the carrier frequency of 24 GHz. Therefore, it is legitimate to assume the Doppler shift as constant for the entire spectrum under investigation.

Other noise effects

The above mentioned effects were identified as the most important ones and therefore included into the simulation. Other disturbances of the radar system such as multipath propagation and the related Rayleigh fading were unaccounted for. Multipath propagation appears for targets that scatter the received wave to more than one direction, i.e. all targets. Furthermore, highly reflective boundary conditions, i.e. a guardrail, another metal plane, or a wet surface needs to be present and provide a second or third propagation path in addition to the line of sight. The effect of these reflections are so called ghost targets. They result from the assumption that received signals traveled on the line of sight from

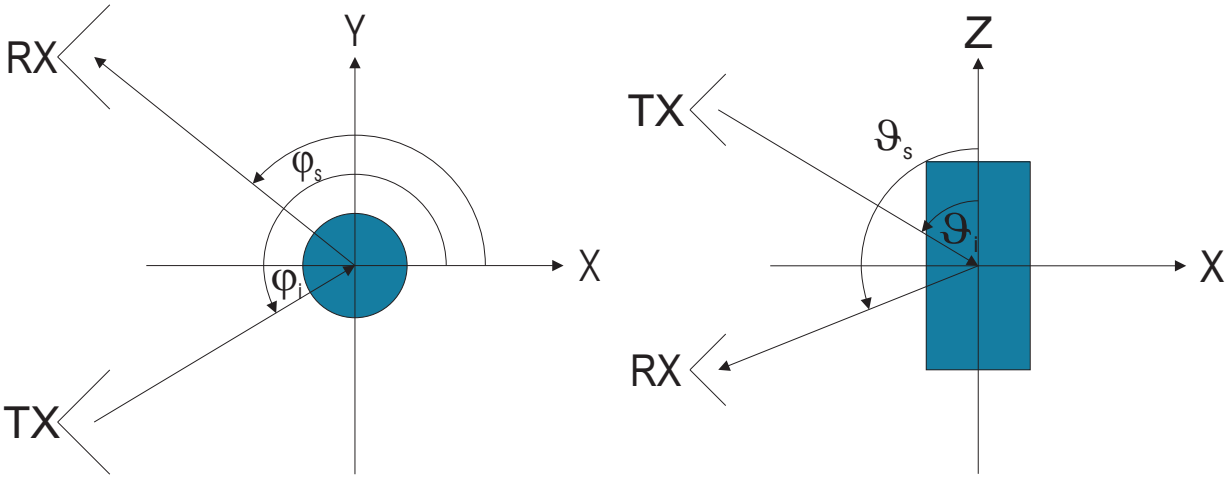

Fig. 4.15: x-y and x-z projections of the geometry

the source to the target and back to the receiver. Given the example in Fig. 4.17, the imaging system might display a total of two targets. First, there is the reflection of the target car that travel back to the radar the direct way, i.e. on a line of sight. The second target that is not existent, will be displayed at the position marked by the gray car. Usually the amplitude of the signal that experiences multiple reflections is reduced by one or more orders of magnitude. The distance of the ghost target is the distance the multiple reflected wave traveled. Ghost targets are a problem that appear with all radar and radar imaging types, as the problem is not caused by system parameters but by environmental parameters. Therefore the only solution for this problem is intelligent target tracking or other means of data processing.

Ghost targets for the system under investigation can also be caused by the combination of information from different sensors as sketched in Sec. 3.5. These are system specific, but the methods to avoid ghost targets can be transferred to the problem mentioned above.

4.3 Full Simulation

Finally, this section will show the power of the discussed algorithm, embedded into the simulation of the radar front end as well as the free space propagation. Using simulation data instead of measured data has two reasons. On the one hand, it allows the comparison of noise corrupted data with ideal data. Second, measured data, was available from one sensor, but not of the entire system.

4.3.1 Flow Chart of the Full Simulation

The flow chart in Fig. 4.18, exhibits all subroutines of the full simulation. It furthermore outlines the data flow. The data on the left hand side of the chart contains environmental parameters, namely “target location and RCS” and “noise parameters”, as well as system

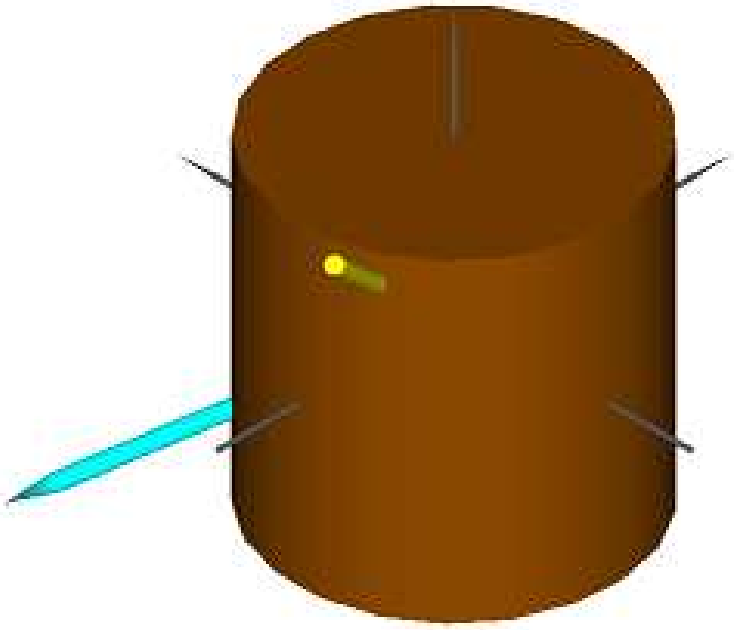

Fig. 4.16: Northwest view of a cylinder model with incident (yellow) and one reflected ray (cyan)

parameters. System parameters are given by the system itself and are generally constant for a specific imaging system. Environmental parameters characterize, as given by the name, the current surrounding area. The right hand side of the graph contains the subroutines and in their sequential order. It exhibits furthermore the data that is handed over from one module to the next. As all subroutines depend on data from the previous module, parallelization is not possible. For the following sections, which contain several examples to illustrate the abilities of the algorithm under investigation, all parameters are given so that the respective results can easily be reproduced.

4.3.2 Results

The following sections will demonstrate the abilities of the entire system. Separated into three chapters, the boundary conditions will converge with each step to near reality. The first step is a noiseless scenario with an inter-target distance larger than the inter-sensor distances. This avoids the creation of possible combinations and the decision for one or more of them. After introducing arbitrary inter-target distances in step two, the last paragraph shows results that were simulated using a noisy environment.

For all simulations, a set of system parameters was used that is discussed in short here. The sensors were set at positions $\mathbf{s}_1 = (-0.75 \quad 0 \quad 0)^{\mathrm{T}}$, $\mathbf{s}_2 = (0 \quad 0 \quad 0)^{\mathrm{T}}$, and $\mathbf{s}_3 = (0.75 \quad 0 \quad 0)^{\mathrm{T}}$. The sensor spacing is deduced from the width of a standard car. As mentioned in the beginning of this document, the intention is, to place the entire system in the front bumper of a car.

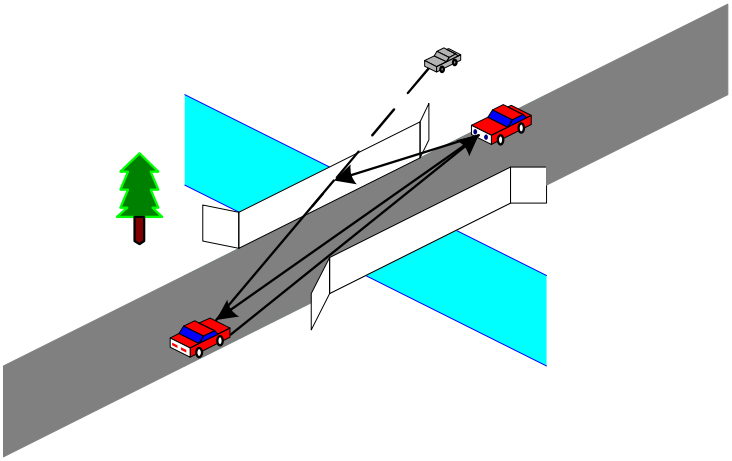

Fig. 4.17: Multipath scenario showing the direct reflection as well as the indirect return via the guardrail and the location of the ghost target

The carrier frequency for all examples was assumed to be 24 GHz, due to the relatively wide ISM band located there. The intermediate frequency was set to 2 GHz. The choice is on the one hand made according to the chip duration, i.e. the IF needs to be greater than half the signal bandwidth, and on the other hand set as low as possible, as devices are cheaper and easier to handle.

The antenna characteristics were chosen according to the considerations in Sec. 2.3.2. Fig. 4.19 shows the transmit antenna pattern, covering the entire field of view with an almost constant gain, whereas the receive antennas in Fig. 4.20 are required to vary, so that a high diversity for the different responses is obtained. The outer receive antennas have an inclination of seven degrees toward the center.

The chip duration was chosen to be $T_c = 1\,\text{ns}$. This choice is somewhat arbitrary, as it can only be chosen properly, when range precision and bandwidth limitations are obeyed. A duration of one nanosecond is accomplishable, when looking at the hardware design side. The only factor that might limit the system to a lower range precision might be the communication control authorities, as the ISM band at 24 GHz is at the moment only 250 kHz wide, i.e. it is to narrow for a $T_c = 1\,\text{ns}$. Chances are good that a wider band is assigned to automotive radar soon.

For the demonstration Gaussian shaped pulses were used. The choice was made, as they exhibit the best time-bandwidth-product. Furthermore, the pulse form in use here, exhibits sharper ACF peaks as rectangular pulses.

Peak excursion and quantization vector are to be chosen with good knowledge of the environmental parameters. Furthermore, antenna characteristics need to be taken into account, to determine a peak excursion value that provides good detection of real targets and prevents the detection of noise spikes as targets. For the quantization vector, it makes sense to use a value about an order of magnitude lower than the peak excursion as the minimum. For the maximum digital value, a value that is roughly the dynamic range of the

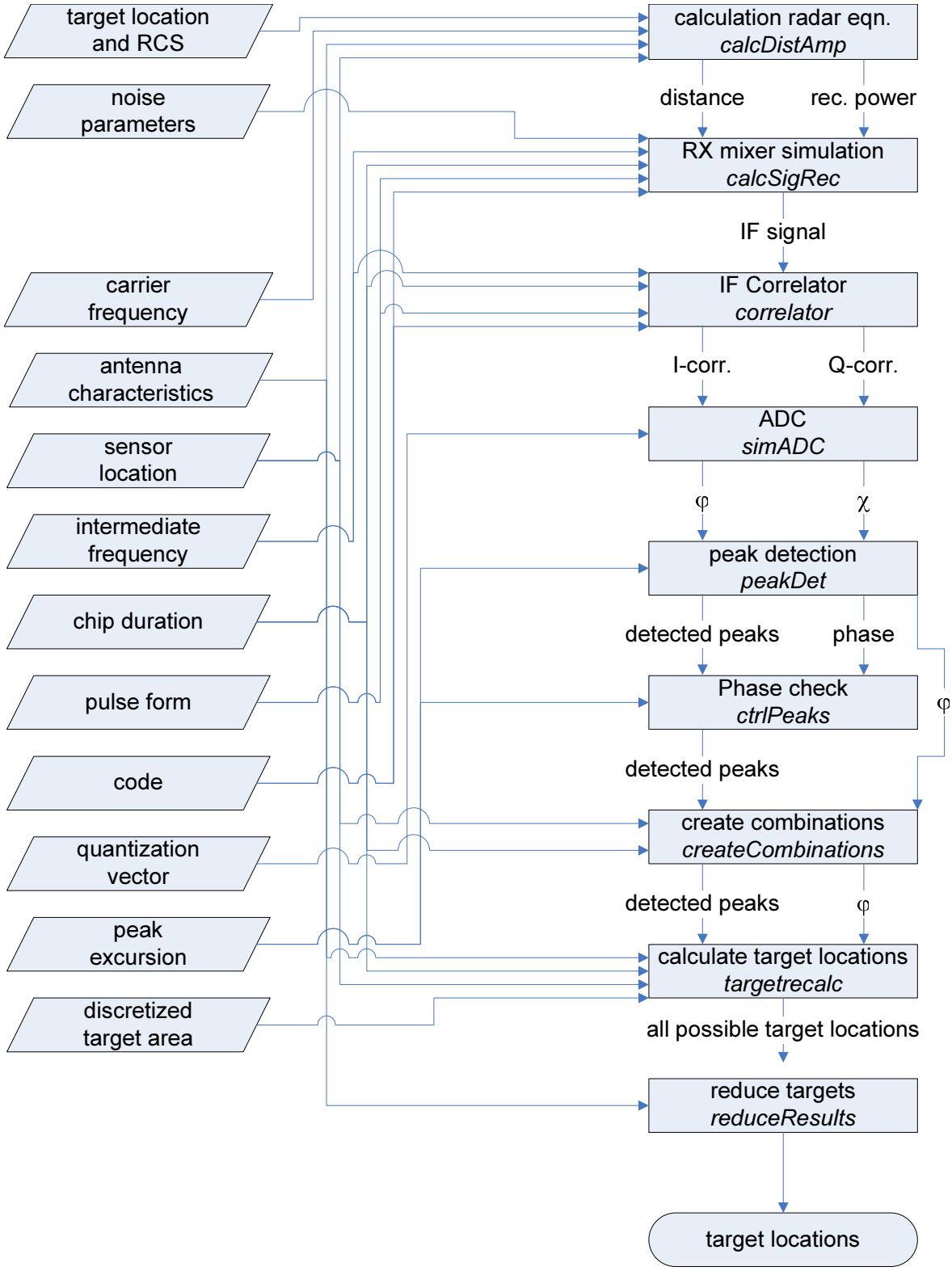

Fig. 4.18: Flow chart of the full simulation implemented in MatLab

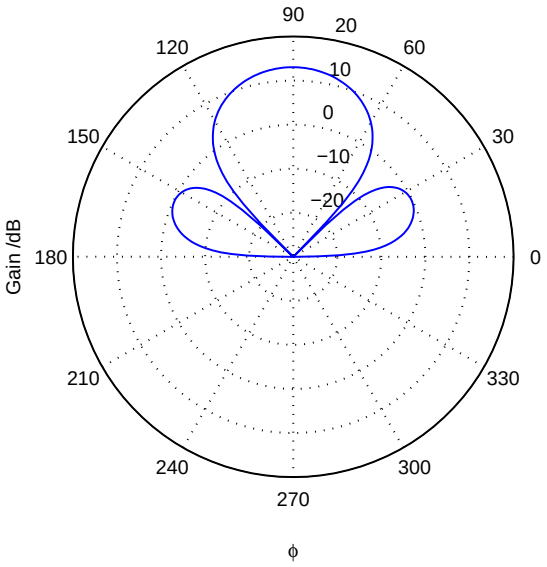

Fig. 4.19: Characteristic used to simulate transmission antenna

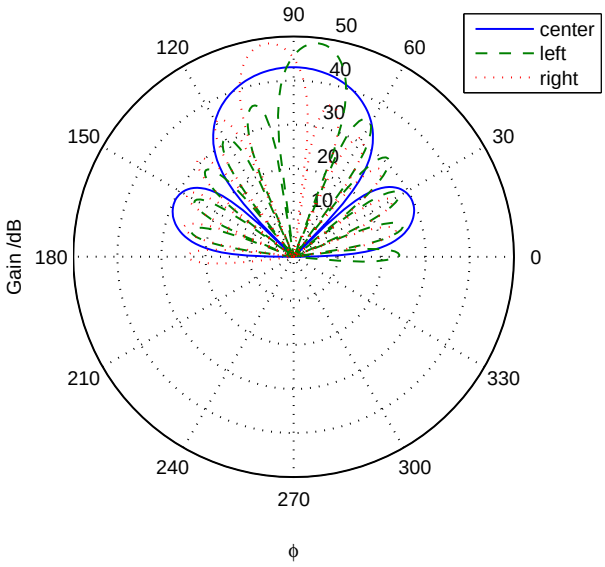

Fig. 4.20: Characteristics used to simulate the three receive antennas

analog system times the minimum digital value is chosen. The values in between minimum and maximum depend on the chosen distribution, for the example here, a logarithmic distribution was chosen.

The choice for the code is made dependent on the available time and the noise in presence. For low noise environments, a short code can be used, whereas longer codes shall be used under noisy circumstances. A code length of $L = 1024\,\text{bit}$ is regarded as a good trade off between required correlation time and resulting SNR.

The discretized target area was set to an area $20 \times 20\,\text{m}^2$, centrally located in front of the radar system. The maximum ranges within this field may bring the analog system to its limits as far as the dynamic range is concerned.

Noiseless Environment

The first two examples will be set up in a noiseless environment. They were chosen to demonstrate the main problem that arises from a finite precision and targets in close proximity.

Unambiguous Combinations The first scenario under investigation is chosen, so that the inter-target distance is greater than the inter-sensor distance, which results in unambiguous sensor response combinations. The targets are located at $\mathbf{t}_1 = (-1 \quad 3 \quad 0)^{\mathrm{T}}$, $\mathbf{t}_2 = (3 \quad 6 \quad 0)^{\mathrm{T}}$, $\mathbf{t}_3 = (1 \quad 10 \quad 0)^{\mathrm{T}}$, and $\mathbf{t}_4 = (-3 \quad 12 \quad 0)^{\mathrm{T}}$, with normalized RCS $a_1 = 30$, $a_2 = 1$, $a_3 = 0.1$, and $a_4 = 5$. With the above mentioned system parameters, the simulated sensors yield the values shown in Tab. 4.3, with d the return distance TX - target - RX. According to the choice of the targets, the creation of the list of possibly

Sensor 1		Sensor 2		Sensor 3	
d / m	A	d / m	A	d / m	A
6.1980	4.9131	6.3420	8.3600	6.6600	3.7682
13.7940	0.0854	13.4340	0.0482	13.1400	0.0388
20.2200	0.1361	20.1180	0.1110	20.0700	0.0879
24.5820	0.0971	24.7560	0.3377	24.9600	0.2458

Tab. 4.2: Table of sensor responses for a three sensor scenario, with four targets visible for all sensors

corresponding targets is trivial. As mentioned in Sec. 3.5, in addition to the full sets, those assuming one quasi-blind sensor are added. The complete list is shown in Tab. 4.3. It results from peak detection of the ACFs that are depicted in Fig. 4.21. Applying the

K	S_1	S_2	S_3	K	S_1	S_2	S_3	K	S_1	S_2	S_3	K	S_1	S_2	S_3
1	1	1	1	5	2	2	2	9	3	3	3	13	4	4	4
2	–	1	1	6	–	2	2	10	–	3	3	14	–	4	4
3	1	–	1	7	2	–	2	11	3	–	3	15	4	–	4
4	1	1	–	8	2	2	–	12	3	3	–	16	4	4	–

Tab. 4.3: All possible combinations that are checked by the algorithm for their minimum J value

algorithm on these combinations yields the final target picture as in Fig. 4.22. It shows a sketched road that helps to visualize roadside dimensions. On the bottom right side of the road, the radar equipped vehicle is assumed. It is marked by the transmit antenna, a triangle in the figure, and three receive antennas, three upside-down triangles. "+" (blue) signs indicate the true target locations, whereas circles (red) indicate the calculated positions. The fact that more calculated targets exist than real ones, results from the consideration of quasi-blind sensors. It is clearly visible in Fig. 4.22 that the system works perfectly for a noiseless environment, even though more targets than sensors are present. With given RCS variations of almost 25 dB, the result proves the applicability of the algorithm and the simulation. Slight deviations of the calculated targets result from combinations assuming quasi-blind sensors. As those are marked in the result list, they can easily be removed. The positions calculated for the full combinations, as well as the deviations from the real targets, are given in Tab. 4.4.

location	calculated	deviation
$(-1 \quad 3 \quad 0)^{\mathrm{T}}$	$(-1.0 \quad 3.0 \quad 0)^{\mathrm{T}}$	0
$(3 \quad 6 \quad 0)^{\mathrm{T}}$	$(3.0 \quad 6.0 \quad 0)^{\mathrm{T}}$	0
$(1 \quad 10 \quad 0)^{\mathrm{T}}$	$(0.8 \quad 10.0 \quad 0)^{\mathrm{T}}$	0.2
$(-3 \quad 12 \quad 0)^{\mathrm{T}}$	$(-3.1 \quad 12.0 \quad 0)^{\mathrm{T}}$	0.1

Tab. 4.4: Calculated results compared to real locations for the unambiguous scenario

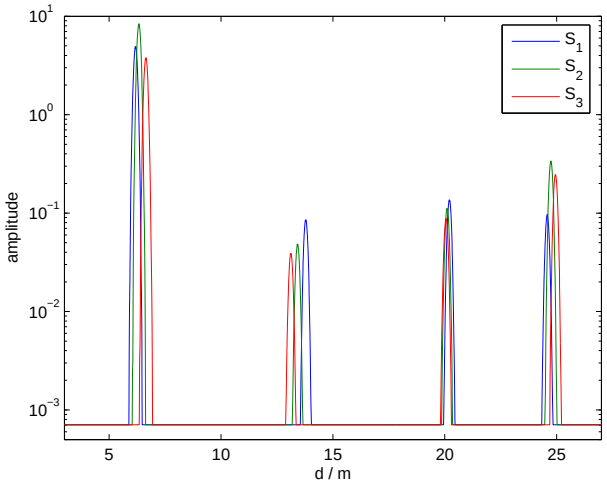

Fig. 4.21: ACFs of all three sensors for the unambiguous scenario

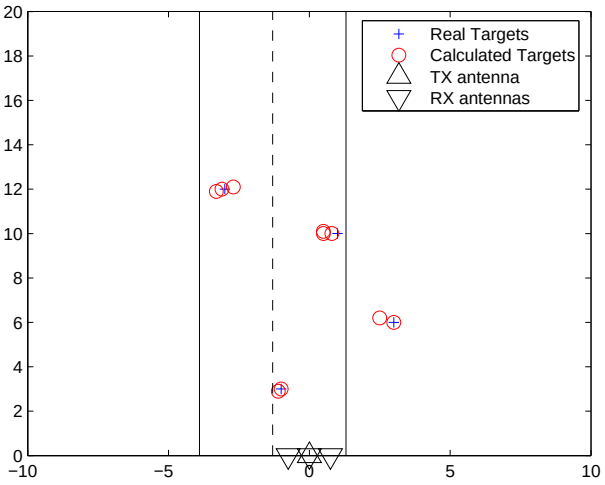

Fig. 4.22: Final calculated target location for the unambiguous scenario

Ambiguous Combinations The above example described above is repeated, again in a noiseless environment, but with targets that are spaced so that several combinations of sensor responses are possible. The targets are now located at $\mathbf{t}_1 = (-1.6 \quad 5 \quad 0)^{\mathrm{T}}$, $\mathbf{t}_2 = (-0.4 \quad 4 \quad 0)^{\mathrm{T}}$, $\mathbf{t}_3 = (0.2 \quad 4 \quad 0)^{\mathrm{T}}$, and $\mathbf{t}_4 = (1.8 \quad 5 \quad 0)^{\mathrm{T}}$, again with normalized RCS $a_1 = 20$, $a_2 = 1$, $a_3 = 20$, and $a_4 = 3$. Again the peaks detected form the ACFs in Fig. 4.23 are listed in Tab. 4.5. Clearly, targets T_2 and T_3 are not resolved into two targets by sensors S_1 and S_3. Furthermore, targets T_1 and T_4 cannot be separated by sensor S_1. As the targets are spaced more closely here, multiple combinations are created. The

Sensor 1		Sensor 2		Sensor 3	
d / m	A	d / m	A	d / m	A
7.9380	0.6356	8.0100	9.4056	8.0460	13.7163
8.1420	8.5353	10.4940	2.4339	10.4340	0.4105
10.3320	0.7178	0	0	10.8000	0.8759
10.9440	0.4105	0	0	0	0

Tab. 4.5: Table of sensor responses for a three sensor scenario, with two targets visible for all sensors, one visible for three sensors, and another one visible for only one sensor

entire list of possible combinations is given in Tab. 4.6. Fig. 4.24 holds again the sketched roadside scenario. It can be observed that target T_4 is slightly dislocated by the algorithm. Furthermore, a ghost target appears between T_3 and T_4. It is caused by combination $K = 9$. Observing the J values of the calculated locations yields $J_9 = 2.29$, whereas other full combination J values are less than 0.5. So by refining the J criterion, ghost targets like in this example might be avoidable. A deviation list as in the last paragraph was created using the four results with the lowest J values. It is shown in Tab. 4.7.

K	S_1	S_2	S_3	K	S_1	S_2	S_3	K	S_1	S_2	S_3
1	–	1	1	6	–	2	2	14	1	–	1
2	1	1	1	7	–	2	3	15	2	–	1
3	1	1	–	8	3	2	–	16	3	–	2
4	2	1	–	9	3	2	2	17	3	–	3
5	2	1	1	10	3	2	3	18	4	–	2
				11	4	2	–	19	4	–	3
				12	4	2	2				
				13	4	2	3				

Tab. 4.6: All possible combinations that are checked by the algorithm for their minimum J value, ambiguous scenario

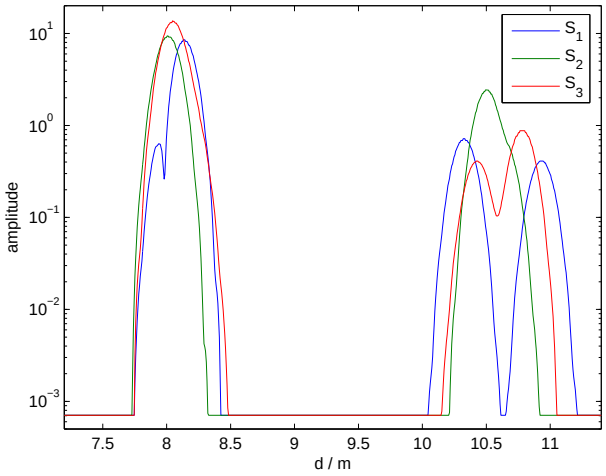

Fig. 4.23: ACFs of all three sensors for the ambiguous scenario

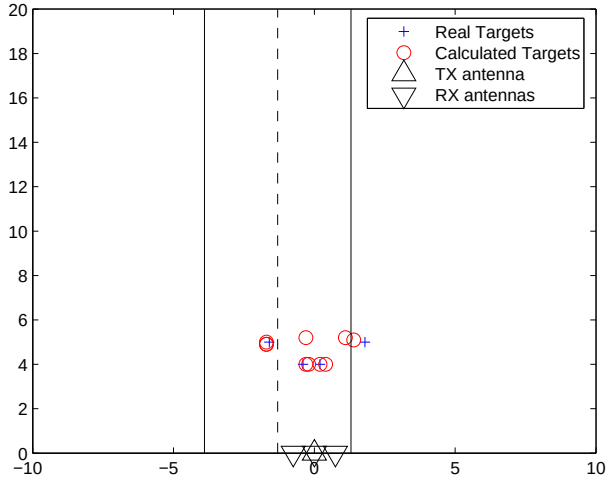

Fig. 4.24: Final calculated target location for the ambiguous scenario

Noisy Environment

To complete the results section, noisy environments are introduced. The following examples are simulated with a normalized DC-offset of 0.1, corresponding roughly to 0.1 V offset. The additive white Gaussian noise is characterized by the ratio average received noise power to average EIRP (SNR'). This was chosen because the SNR at the receiver varies with RCS and distance of the closest target. Targets used for this example outline a simple roadside scenario, which is drawn in Fig. 4.25. The light car at the bottom left is the vehicle equipped with the imaging system under investigation. Targets are located at the positions

location	calculated	deviation
$(-1.6 \quad 5 \quad 0)^{\mathrm{T}}$	$(-1.7 \quad 5.0 \quad 0)^{\mathrm{T}}$	0.1
$(-0.4 \quad 4 \quad 0)^{\mathrm{T}}$	$(-0.3 \quad 4.0 \quad 0)^{\mathrm{T}}$	0.1
$(0.2 \quad 4 \quad 0)^{\mathrm{T}}$	$(0.2 \quad 4.0 \quad 0)^{\mathrm{T}}$	0
$(1.8 \quad 5 \quad 0)^{\mathrm{T}}$	$(1.4 \quad 5.1 \quad 0)^{\mathrm{T}}$	0.4

Tab. 4.7: Comparison of the calculated and real target locations, ambiguous scenario

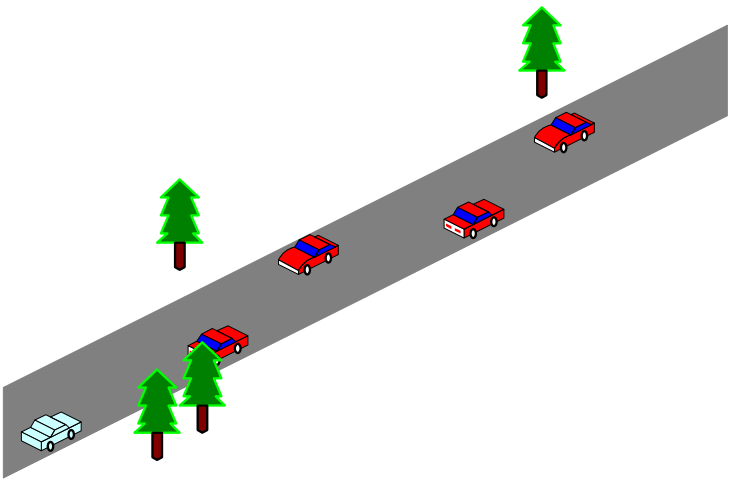

Fig. 4.25: Figure of the assumed roadside scenario

listed in matrix $\mathbf{T}$ with normalized RCS given by $\mathbf{a}$.

$$\mathbf{T} = \begin{pmatrix} -1.0 & 6.0 & 0 \\ -0.5 & 6.0 & 0 \\ 0 & 6.0 & 0 \\ 0.5 & 6.0 & 0 \\ 1.0 & 6.0 & 0 \\ -1.5 & 8.0 & 0 \\ -2.25 & 8.0 & 0 \\ -3.0 & 8.0 & 0 \\ -3.75 & 8.0 & 0 \\ 1.5 & 4.0 & 0 \\ 1.5 & 3.0 & 0 \\ -4.25 & 7.0 & 0 \\ 0.5 & 16.0 & 0 \\ -0.5 & 16.0 & 0 \\ -2.25 & 18.0 & 0 \\ -3.25 & 18.0 & 0 \\ -4.25 & 19.0 & 0 \end{pmatrix}^{\mathrm{T}} \qquad \mathbf{a} = \begin{pmatrix} 0.9 \\ 0.9 \\ 0.9 \\ 0.9 \\ 0.9 \\ 1.0 \\ 1.0 \\ 1.0 \\ 1.0 \\ 0.5 \\ 0.3 \\ 0.4 \\ 2.0 \\ 2.0 \\ 2.0 \\ 2.0 \\ 0.3 \end{pmatrix}$$

The simulation shows good results for both SNR', 80 dB in Fig. 4.26 and 65 dB in Fig. 4.27. Clearly, in both simulations, ghost targets are observed. As mentioned, this is an inevitable result of allowing quasi-blind sensors. Its influence may be reduced by further refinement of the J criteria. The comparison of the two noise levels yields furthermore the disappearance of weak targets, with increasing noise. It is important to mention further key features here. First, even the high noise scenario, does not depict any calculated targets closer than the first real target on the road. This is essential to avoid dangerous emergency breaks during autonomous cruises, or warnings to the driver in assisted cruises. Second, the amount of ghost targets is manageable. Tracing, as possible in a moving environment, was not applied here, but will certainly help to decrease the number of ghost targets enormously.

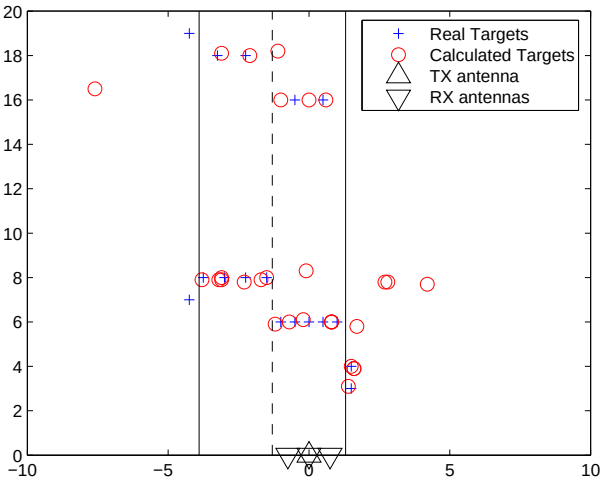

Fig. 4.26: Calculated target locations for a noise level of 80 dB below the EIRP

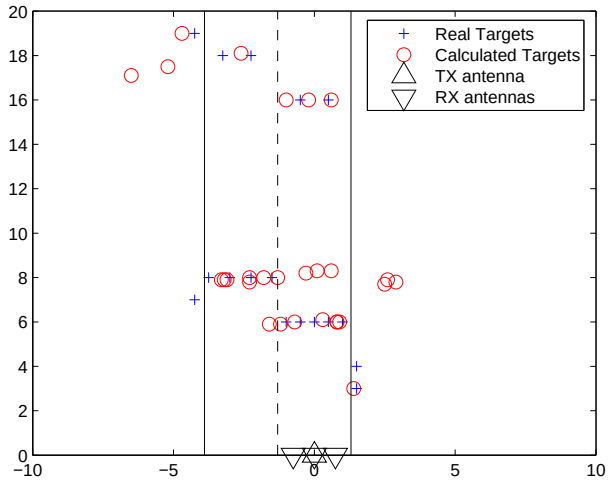

Fig. 4.27: Calculated target locations for a noise level of 65 dB below the EIRP

5. CONCLUSION AND FUTURE WORK

5.1 Conclusion

The presented work demonstrates the applicability of non-coherent sensors for radar imaging. In detail, three pseudo noise radar sensors, i.e. sensors using spreading techniques and a correlator to determine the range information, were combined.

The radar front end concept was taken over from another project with slight modifications. The correlation of the PN receivers now takes place at the intermediate frequency. This yields a higher dynamic range and faster correlation. The spacing in between the sensors was chosen so that the entire system would fit into the front bumper of a standard car, i.e. a maximum width of 1.5 m was obeyed. The acquired data from each sensor is then fed into a processing unit. The task of the processing unit is to combine data from several independent sensors, i.e. it is not necessary to synchronize the sensors in frequency or phase. The processing unit must be able to yield a certain range and angular precision not only for a single target environment, but for a large number of obstacles, i.e. more targets than sensors, so that trilateration alone cannot be utilized.

The processing unit performs at first a standard triangulation. With multi target environments, the usual problem arises. It is ambiguous which response from sensor A corresponds to a certain response of sensor B. Given two targets that have a spacing in between them less than the distance between two sensors, it is impossible for a standard trilateration to determine which responses to combine. To perform trilateration, two corresponding range values are necessary for a two dimensional scenario. With three sensors it is possible to either image a three dimensional scenario or to introduce redundancy that allows the correction of noise effects. The number of range values of different sensors that may correspond to each other depends on system parameters, such as precision, and sensor location. Triangulation alone cannot solve the problem. Therefore, triangulation is performed for all possible combinations. This yields a large number of ghost targets. The second step of the presented algorithm is then intended to increase the location precision and to reduce the number of ghost targets. These goals can be reached by exploiting the amplitude information that is provided by the sensors. Assuming the RCS roughly constant for the small changes in aspect angle, resulting from slightly different sensor locations, different amplitudes for one target can be measured for different sensors, as the receivers have different antenna gain, i.e. gain diversity. The above made assumption now becomes a vital part. Each pair, consisting of range and amplitude value, of every combination is now inserted into the radar equation. The radar equation is calculated upside down, so that it yields the radar cross section (RCS) of the detected object. By now, for each re-

sponse at each sensor, an RCS value is obtained. The obtained RCS for each combination are compared and a deviation number is introduced. Depending on the deviation number, those combinations are marked as true targets that have the smallest in the calculated RCS.

The above described algorithm was simulated together with the modified radar front ends. The results prove the applicability of radar imaging using noncoherent sensors. The obtained images, as presented in the previous section, show good agreement with the given scenario. Within the critical area, i.e. in between the radar equipped car and the nearest obstacle, no ghost targets appear. Furthermore the angular precision is sufficient in this area to determine, whether targets are located on the road or next to it. Fulfilling these two boundary conditions makes the algorithm applicable for the automotive environment. Though the presented work is restricted to two dimensions, an extension to three dimensions is possible, if required. For automotive environments, a three dimensional version, requiring higher computing power, is in general not necessary, as all roadside objects are limited to movements on the ground. Picking up the question from the introduction, whether non coherent radar imaging is suitable for the automotive environment, a clear "yes" is the answer.

5.2 Future Work

Though a functional imaging system is presented, some points are worth to invest some more research. As with any imaging system, ghost targets play a vital role and their avoidance will be treated first.

Target tracking is a feature that has not been included so far. It is an efficient method to identify objects and to reduce ghost targets. Assuming a car that has multiple reflection centers, target tracking might combine several detected scattering centers into one object. Furthermore, a tracking algorithm is able to detect ghost targets. As those targets result from various noise effects, such as multipath propagation, they are likely to change their location and speed discontinuously. Therefore, all objects that do not show continuous, moderate, and rational change of their location properties can be marked as ghost targets and suppressed on the display.

Another field for further improvement would be the speed of the imaging algorithm. It will on the one hand benefit from increased processor speed, but research toward a faster algorithm is definitely worth some effort. Given a faster algorithm, the entire image might be fast enough for pre-crash sensing instead of using sensor raw data only. With pre-crash capable radar images, a lot more possibilities arise for passenger and pedestrian safety. Furthermore, some accidents can even be avoided due to automated breaking.

The peak detector used in the presented work provides sufficient performance. A better suppression of noise peaks would help to reduce ghost targets. One method to avoid the detection of noise peaks would be the further development of the proposed phase detection algorithm. A higher peak detector performance would furthermore increase the dynamic range of the entire system and therefore the maximum imaging range.

Another possibility for system improvement is the analog to digital converter. Even though it is farfetched, a very fast ADC that provides high resolution at the same time, would be able to sample the received signal directly. The obtained digital data can be correlated via a Fourier transform, which is much faster than the analog correlation. Thereafter, considerations, whether a two dimensional correlation is possible, can be made. A 2D correlation would not only allow range measurements directly, but also velocity measurement, via the frequency shift due to the Doppler effect.

BIBLIOGRAPHY

[1] Willie D. Jones. Keeping Cars from Crashing. *IEEE Spectrum*, pages 40–45, Sep. 2001.

[2] Willie D. Jones. Building Safer Cars. *IEEE Spectrum*, pages 82–85, Jan. 2002.

[3] R. H. Rasshofer and K. Gresser. Automotive Radar and Lidar Systems for Next Generation Driver Assistance Functions. In *Advances in Radio Science*, volume 3, pages 205–209, 2005.

[4] J. Otto and W. Pannert. Strukturuntersuchung mit einem FMCW-Radar. In *Deutsche Gesellschaft für Zerstörungsfreie Prüfung, Fachtagung Bauwerksdiagnose - Praktische Anwendungen Zerstörungsfreier Prüfung*, pages 267–271, 1999.

[5] M. Larsen. Point Process Models for Weather Radar Images. In *Geoscience and Remote Sensing Symposium, IGARSS '94*, pages 25–28, 1994.

[6] Stefan Lindenmeier and Johann-Friedrich Luy. Mehrzielfähiges Verfahren und mehrzielfähige Sensorvorrichtung für die Abstands- und Winkelortung von Zielobjekten im Nahbereich. Offenlegungsschrift DE 102 58 367 A1 2004.07.08, Dec. 2002. DaimlerChrysler AG.

[7] C. N. Rheinfelder, S. Lindenmeier, J.-F. Luy, C. Willner, and A. Schuppen. A sensor system based on SiGe MMICs for 24 GHz automotive applications. In *2001 IEEE MTT-S Int. Microwave Symp. Dig.*, volume 3, pages 2239–2242, 2001.

[8] Kyung-Tae Kim, Dong-Kyu Seo, and Hyo-Tae Kim. Efficient Radar Target Recognition Using MUSIC Algorithm and Invariant Features. *IEEE Transactions on Antennas and Propagations*, 50(3), Mar. 2002.

[9] Richard Roy and Thomas Kailath. ESPRIT – Estimation of Signal Parameters Via Rotational Invariance Techniques. *IEEE Transactions on Acoustics, Speech, and Signal Processing*, 37(7), Jul. 1989.

[10] Uwe Siart. *Modellgestützte Signalverarbeitung für inkohärente Radarsensoren in mehreren Frequenzbändern*. Logos Verlag, Berlin, 2005.

[11] Dariu M. Gavrila, Martin Kunert, and Ulrich Lages. A multi-sensor approach for the protection of vulnerable traffic participants - the PROTECTOR project. In *Proc. of the 18th IEEE Instrumentation and Measurement Technology Conference*, 2001.

[12] Y. T. Zhou. Multi-Sensor Image Fusion. In *IEEE International Conference on Image Processing, ICIP-94*, 1994.

[13] M. Schiementz, F. Fölster, and H. Rohling. Angle Estimation Techniques for different 24 GHz Radar Networks. In *Proc. of the International Radar Symposium IRS 2003*, 2003.

[14] Adrian Garrod. A Synchronised Multistatic Automotive Radar Network. In *Proceedings of the VehCom 2003, First International Conference on*, 2003.

[15] Lingmin Meng, Wolfgang Grimm, and Jeffrey Donne. Radar Detection Improvement by Integration of Multi-Object Tracking. In *Proceedings of the Fifth International Conference on Information Fusion*, 2002.

[16] Frank Kruse, Florian Fölster, Malte Ahrholdt, Marc-Michael Meinecke, and Hermann Rohling. Object Classification with Automotive Radar. In *Proc. of the International Radar Symposium IRS 2003*, 2003.

[17] I. Leizerson, S. G. Lipson, and V. Sarafis. Superresolution in far-field imaging. *Optics Letters, Optical Society of America*, 19(3), Mar. 2002.

[18] Magnus O. Olbrich. *A Short-Range Pseudo-Noise Radar.* PhD thesis, Technische Universität München, to be published.

[19] V. Filimon and J. Buechler. A Pre-Crash Radar Sensor System Based on Pseudo-Noise Coding. In *2000 IEEE MTT-S Int. Microwave Symp. Dig.*, volume 3, pages 1415–1418, 2000.

[20] Merrill L. Skolnik. *Radar Handbook.* McGraw-Hill, Boston, MA, 2nd edition, 1990.

[21] I. Gresham, A. Jenkins, R. Egri, and et al. Ultra-Wideband Radar Sensors for Short-Range Vehicular Applications. In *IEEE Transactions on Microwave Theory and Techniques*, volume 52, pages 2105–2122, Sep. 2004.

[22] Hans Dieter Lüke. *Korrelationssignale.* Springer-Verlag, Berlin, 1992.

[23] Florian Gerbl. A Numerical Model of a 24-GHz PN-Radar. Master's thesis, Technische Universität München, Feb. 2003.

[24] Robert A. Scholtz and Lloyd R. Welch. Groupcharacters: Sequences with Good Correlation Properties. In *IEEE Transactions on Information Theory*, volume IT-24, pages 537–545, Sep. 1978.

[25] J. Freese, H.-L. Blöcher, J. Wenger, and R. Jakoby. Microstrip Patch Arrays for a Millimeter-Wave Near Range Radar Sensor. In *German Radar Syposium, Proceedings of the*, pages 149–153, 2000.

[26] Hideo Iizuka, Kunio Sakakibara, Toshiaki Watanabe, Kazuo Sato, and Kunitoshi Nishikawa. Millimeter-Wave Microstrip Array Antenna with High Efficiency for Automotive Radar Systems. Technical report, R&D Review of Toyota CRDL, 2002.

[27] Frank Kolak and Channabasappa Eswarappa. A Low Profile 77 GHz Three Beam Antenna for Automotive Radar. In *2001 IEEE MTT-S Int. Microwave Symp. Dig.*, volume 2, pages 1107–1110, 2001.

[28] Christian Morhart. Wanderwellenantennen mit hohem Gewinn für 24 GHz. Master's thesis, Technische Universität München, Sep. 2004.

[29] F. B. Helmbrecht, D. Olbrich, M. O. and. Zitzmann, and E. M. Biebl. A PN-Radar Correlator with IF-Input Ports. In *Proc. 35 th European Microwave Conf.*, to be published.

[30] Athanasios Papoulis. *Probability, Random Variables, and Stochastic Processes*. McGraw-Hill, New York, 1991.

[31] John G. Proakis. *Digital Communications*. McGraw-Hill, New York, 4th edition, 2001.

[32] Hrvoje Babic and Mladen Vucic. System Functions with Minimum Time-Bandwidth Product Based on the Higher Order Moments. In *Proceedings of the 2nd International Symposium on Image and Signal Processing and Analysis*, pages 479–484, Jun. 2001.

[33] Paul A. Tipler. *Physik*. Spektrum Akademischer Verlag, Heidelberg, 1995.

[34] Merrill L. Skolnik. *Introduction to Radar Systems*. McGraw-Hill International, Singapore, 2001.

[35] M. L. Jacobson. Auto-Threshold Peak Detection in Physical Signals. In *Engineering in Medicine and Biology Society, Proc. of the 23rd Annual International Conference of the IEEE*, volume 3, pages 2194–2195, 2001.

[36] Eugene Hecht. *Optics*. Addison Wesley, San Francisco, 2002.

[37] Peter Russer. Hochfrequenztechnik 2. Skriptum zur Vorlesung an der Technischen Universität München, 2001.

[38] André Quinquis, Emanuel Radoi, and Felix-Costinel Totir. Some Radar Imagery Results Using Superresolution Techniques. *IEEE Transactions on Antennas and Propagations*, 52(5), May 2004.

[39] F. B. Helmbrecht and E. M. Biebl. Radar Imaging Using Non-Coherent Sensors. In *2005 IEEE MTT-S Int. Microwave Symp. Dig.*, to be published.

[40] George T. Ruck. *Radar Cross Section Handbook*, volume 1. Plenum Press, New York, 1970.

[41] George T. Ruck. *Radar Cross Section Handbook*, volume 2. Plenum Press, New York, 1970.

[42] M. Ogawa, K. Kidono, and Y. Asano. Electrically Scanned Millimeter Wave Automotive Radar With Wide Detection Region. *SAE Technical Paper Series, ISSN 0148-7191*, 2003.

[43] Carsten Metz, Jens Grubert, Johann Heyen, Arne F. Jacob, Stephan Janot, Ernst Lissel, Gerald Oberschmidt, and Leif C. Stange. Fully Integrated Automotive Radar Sensor With Versatile Resolution. *IEEE Transactions on Antennas and Propagations*, 49(12), Dec. 2001.

[44] Winfried Mayer, Markus Wetzel, and Wolfgang Menzel. A Novel Direct-Imaging Radar Sensor with Frequency Scanned Antenna. In *2003 IEEE MTT-S Int. Microwave Symp. Dig.*, volume 3, pages 1941–1944, 2003.

[45] Eugene F. Knott. *Radar Cross Section*. Artech House, Dedham, MA, 1985.

[46] J. W. Crispin and K. M. Siegel, editors. *Methods of Radar Cross-Section Analysis*. Academic Press, New York, 1968.

[47] F. B. Helmbrecht and E. M. Biebl. Radar Cross Section of Dielectric and Metallic Homogeneous Cylinders. In *Kleinheubacher Tagung*, Oct. 2003.